One of the potentially serious side effects of drugs is cardiotoxicity which is the negative effect of drugs on the normal heart function. Cardiotoxicity has been a frequent cause for withdrawal of drugs from market and costly late-stage clinical drug failure, highlighting an unmet need for improved in vitro cardiotoxicity screening assays.

Heart muscle cells, cardiomyocytes, in a beating heart experience cyclic stretching and contraction. It has been shown in the literature that cardiomyocytes can sense mechanical stretching and adapt their electrical and mechanical activity to it. Therefore, more reliable and predictive screening results can potentially be obtained by incorporating the mechanical stretching and contraction in the in vitro models.

The focus of this thesis is on developing a manufacturable technology to realize a novel heart-on-a-chip platform which enables mimicking the cyclic mechanical stretching and contraction for the cultured cardiomyocytes as it happens in the heart while performing electrophysiological measurements for cardiotoxicity detection.

The platform is based on pneumatically actuated Stretchable Micro-Electrode Array (SMEA) chips. A novel and robust mechanical design for the SMEAs is presented which enables fabrication of the electrical interconnects without the need for space-demanding meandering designs, or the use of unconventional stretchable conductive materials. In order to enable large scale production of the SMEAs a manufacturable fabrication method was developed for embedding the electrodes and electrical interconnects in the stretchable membranes.

The electrochemical and electromechanical characterization of the chips are presented, together with proof of concept field potential measurements from human stem cell derived cardiomyocytes under cyclic mechanical loading.

Stretchable Micro-Electrode Arrays for Electrophysiology

Saeed Khoshfetrat Pakazad

Stretchable
Micro-Electrode Arrays
for Electrophysiology
Design, Fabrication and Characterization

Saeed Khoshfetrat Pakazad

TUDelft — Delft University of Technology

nanonextnl — innovating with micro and nanotechnology

PHILIPS

Stretchable Micro-Electrode Arrays for Electrophysiology

Design, Fabrication and Characterization

Proefschrift

ter verkrijging van de graad van doctor
aan de Technische Universiteit Delft,
op gezag van de Rector Magnificus prof. ir. K. C. A. M. Luyben,
voorzitter van het College voor Promoties,
in het openbaar te verdedigen op maandag 15 juni 2015 om 12:30 uur

door

Saeed KHOSHFETRAT PAKAZAD

Master of Science
in Electrical and Biomedical Engineering
geboren te Tehran, Iran

This dissertation has been approved by the promotor:

Prof. dr. ir. R. Dekker

Composition of the doctoral committee:

Rector Magnificus   chairman
Prof. dr. ir. R. Dekker   promotor

Independent members:

Prof. dr. ir. A. van den Berg   University of Twente
Dr. P. C. J. J. Passier   Leiden University Medical Center
Prof. dr. P. M. Sarro   Delft University of Technology
Prof. dr. ing. M. Staat   FH Aachen University of Applied Sciences
Dr. A. Bahinski   Wyss Institute at Harvard University
Dr. H. Huiberts   Philips Research Eindhoven
Prof. Dr. G. C. A. M. Janssen   Delft University of Technology, substitute
                                  member

An electronic version of this dissertation is available at:
http://repository.tudelft.nl

I dedicate this endeavor *to my family, Maryam, Reza, Soheil and Sina, for their unconditional love and support, and to my friends for always supporting me and tolerating my reservedness during the demanding times preparing this dissertation.*

Contents

Chapter 1 - Introduction

1.1 Motivation

In the pharmaceutical industry new drug compounds are tested in several stages during development before they are released to the market. Figure 1.1 shows the different stages of the pharmaceutical R&D pipeline which starts with the discovery of the compounds and continues with the screening of the compounds in pre-clinical and clinical phases. In the preclinical phase the drug compounds are tested on in vitro cell-based models, computational models (*in silico* models), and animals. The drug candidates that pass the preclinical phase are then tested on a group of human volunteers in the clinical phase. Finally, the drug candidates that pass the clinical phase, after obtaining approval form the regulatory authorities are allowed to enter the market.
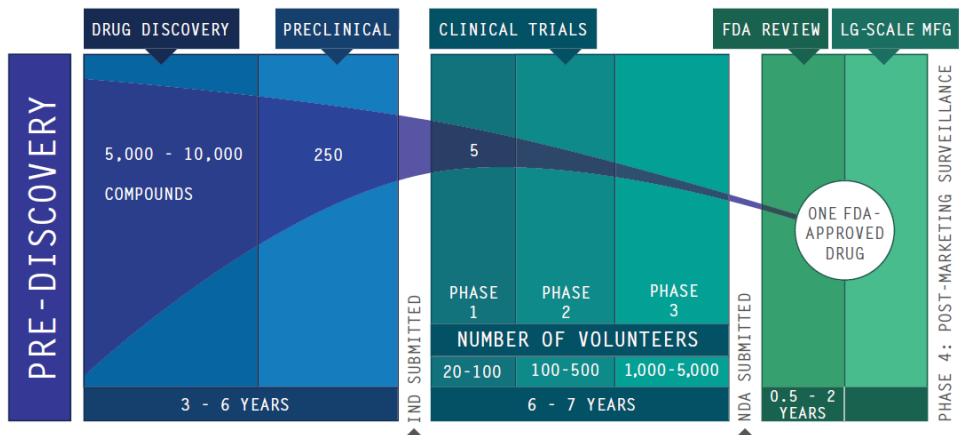
Figure 1.1 Pharmaceutical R&D pipeline. Adapted from [1].

For every 5,000 to 10,000 new compounds that enter the pipeline, only one receives approval with an average of $1.2 billion R&D investment over a period of 10-15 years for each new medicine [2]. Therefore, late stage failure of drugs is extremely costly. Moreover, despite careful screening of drug candidates before entering the market, drugs are regularly being withdrawn from market because of unexpected side-effects, incurring huge financial losses to the pharmaceutical

industry [3]. Models capable of predicting the failure of a compound on humans as early as possible in the pipeline can save significant development costs and improve drug safety.

Inaccurate detection of certain side effects of drugs on humans during drug development can be attributed firstly to the fact that the models used in the preclinical phase of drug screening are non-human models, e.g. animals or over-simplified in vitro cell models, which do not recapitulate the human physiology adequately. Additionally, different genetic profiles show different sensitivity to certain side effects of drugs, and the limited number of human volunteers in the clinical phase hardly represents the whole genetic variability of the market.

With the recent advances in stem cell technology it has become feasible to implement in vitro models based on human cells for drug screening purposes. Specifically, by using the induced pluripotent stem cell (iPSC) technology it is possible to reprogram adult cells, e.g. skin cells, from any individual to become pluripotent stem cells, proliferate the stem cells and subsequently direct (differentiate) the stem cells into becoming another cell type of that individual, such as neurons, heart, pancreatic, and liver cells [4]. The iPSC cells can be produced in reasonable quantities in a reproducible manner and are commercially available, enabling high throughput screening in human in vitro models.

The mentioned advances in stem cell technology have given momentum to the relatively new and evolving "organs-on-chips" field of research which aims at developing in vitro models of different organs by incorporating the stem cell derived cells in proper micro-environments which mimic the in vivo conditions, with the help of microfluidics and microfabrication technologies [5]–[7]. Such models based on human cells can potentially yield more predictive and accurate results than conventional non-human in vitro models [5]. Moreover, many drug-induced toxicities occur in diseased or genetically predisposed patients rather than in normal healthy volunteers used in clinical trials [8]. By utilizing the iPSC technology it is possible to test the drugs on in vitro organ-on-chip models based on diseased cells, or cells derived from specific genetic profiles, in an early stage of drug development, thereby preventing late stage failures of compounds and early stage termination of promising drug candidates.

A number of successful examples of organ-on-chip models have already been demonstrated for several organs including the lung, kidney, blood vessels, liver and

heart [5]–[7], [9], [10]. Specifically for the case of heart the muscular thin films (MTFs) [9] and the CellDrum technology [11] have been demonstrated as models to study the effect of drugs on contractile force and beating rhythm of the heart muscle cells (cardiomyocytes). The MTFs consist of an aligned layer of cardiomyocytes on sub-millimeter sized thin film cantilevers of soft elastomers. Deflection of these cantilevers during muscle contraction allows for calculation of the contraction force of the cardiomyocytes. In the CellDrum platform the cardiomyocytes are grown either within flexible, circular collagen gels or as monolayer on top of 1µm thick silicone membranes. The deflection of the membrane represents the contraction force. Also, by applying air pressure to the membrane, mechanical loading of the cells is possible. These models are mainly mechanical and do not enable in situ electrophysiological measurements from the cardiomyocytes.

The focus of this thesis is on developing a manufacturable technology to realize a novel electrophysiological heart-on-a-chip model capable of mimicking the cyclic mechanical stretching and contraction of the heart muscle tissue as it happens in vivo while simultaneously performing electrophysiological measurements. By incorporating iPSC heart muscle cells, such a model can be used as a potentially more accurate cardiac safety pharmacology assay, specifically for cardiotoxicity detection. The model can also be used for developing human cardiac disease models by simulating pathophysiological electro-mechanical conditions. In addition, the electrophysiological measurements obtained from the model under variable levels of reproduced cardiac load can be used to develop and verify *in silico* computational electrophysiological models for the heart function and cardiotoxicity mechanisms [12]–[14].

1.1.1 Cardiotoxicity

Cardiotoxicity is one of the most serious side effects of drugs. It involves altering the normal functioning of the cardiomyocytes and may cause life threatening cardiac arrhythmias leading to cardiac arrest. Cardiotoxicity has been the leading cause of drug withdrawals from the market in the past decades [3], which highlights an unmet need in the pharmaceutical R&D for more accurate and predictive models to detect cardiotoxicity.

An important indication for drug-induced proarrhythmic cardiotoxicity is the prolongation of the QT interval observed in body surface ECG (electrocardiogram)

[15]–[17]. The QT interval represents the duration of the ventricular depolarization and subsequent repolarization, measured from the beginning of the QRS complex to the end of the T wave. The QT interval roughly represents the duration of the ventricular cardiomyocytes' electrical action potential. The prolongation of the QT interval originates from the prolongation in the ventricular cardiomyocytes action potential duration (Figure 1.2).

An action potential signal - which triggers the contraction of cardiomyocytes by causing intracellular release of calcium ions - consists of a rapid increase of the transmembrane potential (inside versus outside) of the cardiomyocyte from a negative value to a positive value (depolarization) and subsequent gradual recovery of the transmembrane potential (repolarization) to the original values as show in Figure 1.2 (top). Briefly, the action potential is initiated when a part of the cell membrane is stimulated by an electrical, chemical, mechanical or thermal stimulus - normally electrical for the case of the heart - which triggers an inward flux of Na^+ and Ca^{2+} ions through corresponding ion channels in the cell membrane resulting in a rapid increase of the transmembrane potential. This is followed by an outward flux of K^+ ions which gradually restore the original transmembrane potential [18]. Drug compounds that interfere with the normal functioning of the K^+ ion channels potentially can cause prolongation of the repolarization period which is associated with life threatening ventricular arrhythmias [16], [17], [19].
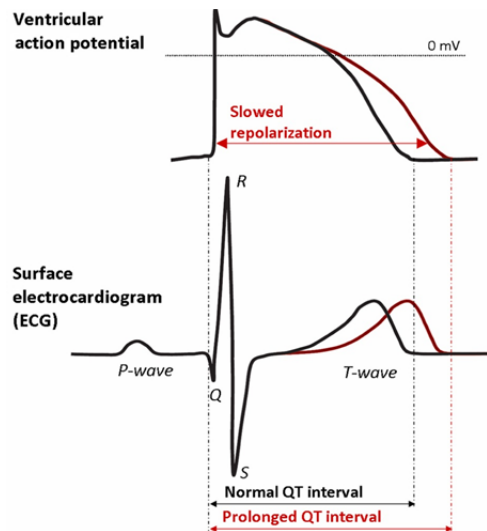
**Figure 1.2** The prolongation of ventricular action potential duration and resulting prolongation of the body surface ECG QT interval. Figure adapted from [20].

1.1.2   Action potential measurement

The in vitro electrophysiological models that can be used to detect cardiotoxicity are mostly based on measurement of the ion channel currents or action potential of cardiomyocytes subjected to drug compounds [14], [21], [22]. These measurements can be performed either by using the patch clamp procedure or through extracellular (micro-)electrodes in close contact with the cardiomyocytes.

The patch clamp method is capable of directly measuring the transmembrane potential by puncturing the cell membrane and measuring the potential difference between inside and outside of the cell, as well as measuring the current through individual ion channels. In this method a micropipette is brought into contact with the cell membrane by using micro-manipulators under a microscope, and by subsequently applying suction to the pipette the membrane is perforated or a single ion channel is isolated for measurement. Although very accurate measurements are possible with this method, manual patch clamping is a tedious and low throughput process. In order to increase the throughput, automatic patch clamp platforms are being developed [23].

The action potential of cardiomyocytes can also be indirectly measured through extracellular micro-electrodes. In this method the internal potential of the cell is coupled through the cell membrane impedance to an external electrode in contact with the cell, and the measured signal is called the field potential [24], [25]. Field potential measurements from cultured cardiomyocytes or tissue slices are performed with Micro-Electrode Arrays (MEAs) which have electrodes integrated in the cell culture substrates (Figure 1.3). Through th micro-electrode in contact with the cell membrane a high-pass filtered version of the action potential is measured , which resembles the time derivative of the actual transmembrane action potential, as explained in more detail in chapter 5 [25]–[27]. A prolongation of the measured field potential signal thus corresponds to a prolongation of the duration of the actual action potential (Figure 1.4).
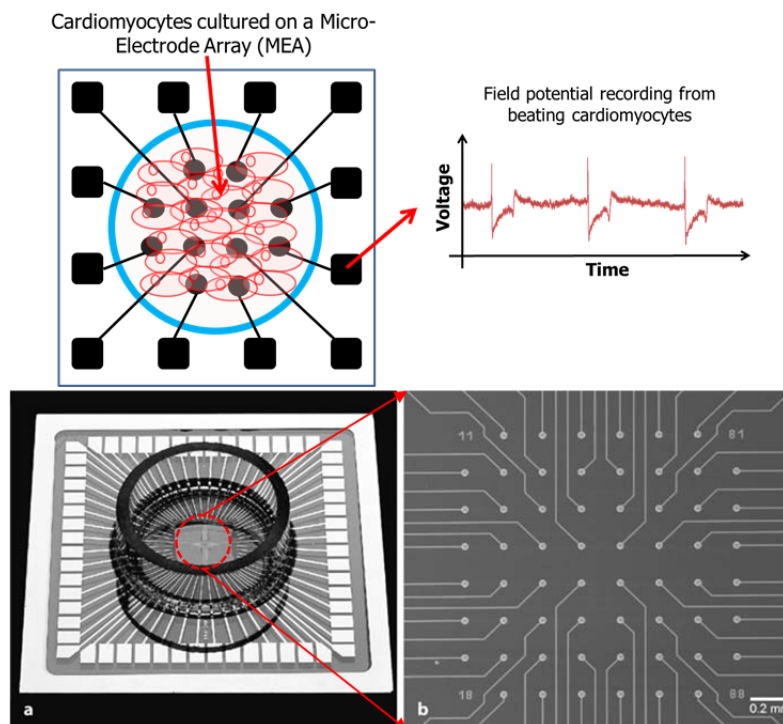
Figure 1.3 (top) Schematic representation of a Micro-electrode Array (MEA) device. The field potential is measured through the electrodes integrated in the cell culture substrate. (bottom) A picture of a commercial MEA with the micro-electrode area magnified. A glass ring around the electrode area holds the culture medium for the cells. Adapted from [24].
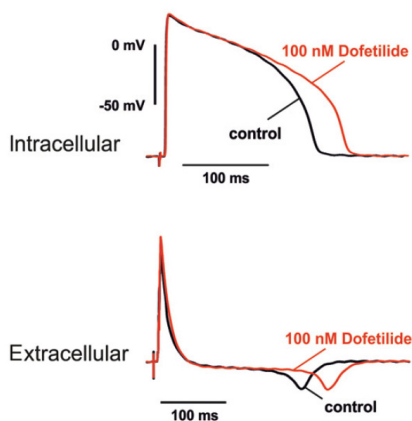
Figure 1.4 An example of the prolongation effect of a compound on the duration of intracellular action potential (top) and the extracellular field potential (bottom). Adapted from [27].

MEAs enable non-invasive long term monitoring of the cultured cardiomyocytes' action potential and provide medium to high throughput solutions for cardiotoxicity screening applications. However, MEAs are normally fabricated on rigid substrates, which do not properly model the in vivo micro-environment of the cells and preclude mechanical stretching and contraction of cultured cardiomyocytes as it happens in a beating heart. As described in the next section the mechanical cues of the culture environment are important to realistically reproduce the in vivo physiology of the cardiomyocytes.

1.1.3   Limitations of current in vitro electrophysiological models

1.1.3.1   Mechanical stimulation

Cardiomyocytes in vivo stretch during diastole when the heart fills with blood and subsequently contract during systole to pump out the blood. Cardiomyocytes can sense mechanical stretching and adapt their response to it, through several inter-related mechano-biological phenomena [28]–[31]. Examples are the stretch-induced increase in contraction force (Frank-Starling response) [32], or changes in the electrophysiological response of the cells (mechano-electric coupling) reflected in the alteration of action potential shape, duration, and rhythm [28]. These responses are mediated through different mechanotransduction phenomena [33]–[35], for instance stretch activated ion channels (SACs) or stretch sensitive biomolecules in the cell membrane, cytoskeleton or intra-cellular organelles [36]–[39], as well as inter-cellular mechano-electrics interactions [40], [41]. As a result of the mechanically induced physiological changes, increased mechanical stretch can make the heart tissue more susceptible to drug-induced arrhythmias, especially in diseased tissue such as hypertrophied ventricular tissue [42], [43].

While various effects of mechanical stretch on the electrophysiology of cardiomyocytes have been reported in literature, including this mechanical aspect in in vitro electrophysiological models has been technically challenging. The current approaches used for performing electrophysiological measurements while applying mechanical stretch involve manual clamping of cardiomyocytes or isolated heart tissue samples between micromanipulator-mounted mechanical arms, patch clamp pipettes or carbon fibers [42], [44], [45], or performing measurements on ex vivo perfused whole heart preparations (Langendorff heart) [14], [46]. These approaches are extremely low throughput, and not suitable for safety pharmacology in which a large number of compounds have to be screened.

1.1.3.2   Maturation and alignment

A limitation of the current electrophysiological models based on stem cell derived cardiomyocytes is the level of maturation of the cardiomyocytes. The stem cell derived cardiomyocytes tend to be less mature than adult human cardiomyocytes, resulting in differences in the physiology of the cells [8], [47], [48]. For instance a number of the ion channels involved in cardiotoxicity might not be present or fully developed in immature cardiomyocytes [8]. Apart from chemical and biological factors that govern the differentiation of stem cells, it has been demonstrated that electrical and/or mechanical stimulation resembling the in vivo developmental conditions improves the maturation of stem cell derived cardiomyocytes [47]–[51]. Therefore, a platform capable of providing proper in vitro mechano-electric stimulation can be utilized to further mature the stem cell derived cardiomyocytes prior to cardiotoxicity screening.

Moreover, in normal heart muscle tissue the cardiomyocytes are elongated and aligned to each other to enable directional contractility of the tissue. The anisotropic arrangement of cardiomyocytes also results in anisotropic physiological characteristics, for instance anisotropic electrical conduction velocity and anisotropic distribution of intercellular connections (gap junctions) and arrangement of sarcomeres, etc [52]. Normally, in in vitro cardiomyocyte cultures the cells form isotropic cell layers which do not acquire the mentioned in vivo anisotropic characteristics. In order to obtain a more physiologically relevant model, the anisotropic alignment of cardiomyocytes should therefore be reproduced [6], [50], [53], [54]. Additionally, the direction of mechanical stretch with respect to the cell alignment direction also affects the physiological response of the cells to the applied stretch [55]–[57], highlighting the need for control over cell alignment direction in the in vitro models which enable mechanical loading of the cultured cells.

1.2   Stretchable Micro-Electrode Array (SMEA) platform

As mentioned previously, micro-electrode arrays (MEAs) enable long term non-invasive monitoring of electrical activity of the cardiomyocytes by recording the extracellular field potential. Embedding the electrode array in the surface of a stretchable membrane enables the application of physiologically relevant mechanical stretch to the cardiomyocytes cultured on the membrane. Such a device can replicate the in vivo stretching and contraction of the cells during electrical

measurements, and also enables in situ maturation of the cultured stem cell derived cardiomyocytes. Additionally, by incorporating micro-features on the surface of the membrane it is possible to induce alignment of the cardiomyocytes in a certain direction, as discussed later. This results in a better replication of the in vivo tissue structure and allows for the stretch to be applied in a certain orientation with respect to that of the cardiomyocytes.

1.2.1 Electrical interconnects to the electrodes

In a stretchable micro-electrode array device the electrical interconnects to the electrodes embedded in the elastomeric membrane should withstand the strains in the stretching membrane. Since the conductive materials (metals and metal alloys) commonly used in micro-fabrication are not inherently stretchable, alternative materials or special mechanical designs have been proposed for the electrical interconnects in stretchable devices [58], [59].

One category of methods used to fabricate stretchable electrical interconnects is based on using stretchable conductive materials or composites; for instance, liquid metal alloys [60], elastomers doped or implanted with conductive particles [61]–[63], and metal deposition on elastomers [64]. These methods are generally not suitable for high volume micro-fabrication due to difficulties in processing, deposition and patterning of these materials with common micro-fabrication techniques, and the problems associated with thin film processing on elastomers.

The other strategy to realize stretchable interconnects is based on designing the electrical interconnects in wavy or horseshoe shapes which accommodate the strains during stretching by bending in-plane or out-of-plane [65]–[68]. In these methods the interconnects normally occupy a large portion of the surface area of the device and change the surface topography and mechanical properties.

The stretchable micro-electrode arrays (SMEAs) are used as cell culture substrates. Therefore, the surface properties of the devices, such as topography and mechanical stiffness, should be minimally altered by the electrical interconnects. Moreover, in order to address drug screening applications a manufacturable micro-fabrication technology should be used to enable high volume fabrication of the (disposable) chips. To address these constraints, a novel mechanical design for the electrical interconnects is proposed in this thesis, which enables stretchability of the devices without using meandering structures or the use of unconventional

stretchable materials. In this method, as described in chapter 2, the optimal routes for the interconnects which result in sufficiently low stress levels in the interconnects are determined by analysing the principal strains in pneumatically inflating membranes.

1.2.2 Cell alignment

Cells in tissue are surrounded by a hierarchically organized matrix of proteins, called the extracellular matrix (ECM), which serves a variety of biological purposes including connecting the cells and giving form and mechanical stability to the tissue [69]. These proteins are mainly produced (deposited) by a special category of cells called the fibroblast. Cells adhere to the ECM through certain transmembrane proteins, integrins, which dynamically anchor the cell's cytoskeleton to the ECM through a protein complex called the focal adhesion, as graphically illustrated in Figure 1.5.

To promote the adhesion of cells, the in vitro cell culture substrates are normally coated by one or a combination of fibrous ECM proteins, e.g. collagens, elastins, fibronectins and laminins, etc [70]. Additionally, by patterning the ECM proteins on the surface of the culture substrate, the cells can be patterned in certain shapes or aligned in a certain direction defined by the coating pattern [71], [72]. A common way of patterning the ECM components is micro-contact printing in which a stamp containing the desired (micro-)pattern is used to transfer the ECM proteins to the culture substrate [73]–[76]. It has been demonstrated that cardiomyocytes can be aligned using ECM protein fibronectin patterned in the form of stripes on silicone and other types of substrates [9], [54], [77].
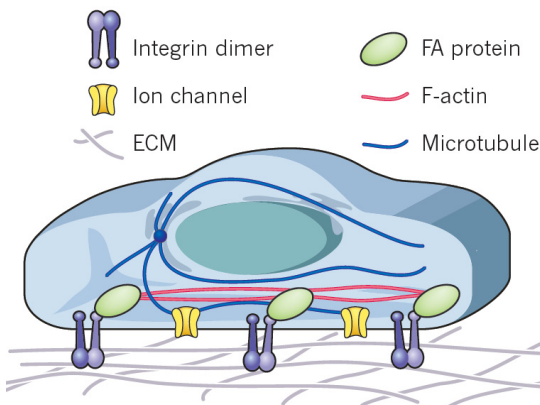

Figure 1.5 Cell adhesion to ECM through integrins and focal adhesion proteins. Adapted from [33].

Another method used to induce alignment of the cells is using topographical micro micro/nano features, e.g, grooves, on the surface of the cell culture substrate [50], [53], [78]–[80]. The mechanisms through which the micro/nano features affect the adhesion pattern of cells and induce alignment are still being investigated. Most likely they can be attributed to the modulation of the orientation and conformation of ECM protein coatings and to the resulting anisotropic distribution of adhesion sites. It has been demonstrated that the cells can be aligned and exposed to longitudinal or transversal strain by using microgrooves in PDMS substrates [56], [57], [80], [81].

Using micro/nano features to induce cell alignment is a more favorable method in terms of throughput, since such features can be prefabricated in the cell culture substrates without the need for manual stamping of ECM proteins. To include the capability of cell alignment in the platform micro-features of arbitrary shape can be integrated on the surface of the stretchable MEA membrane using the proposed microfabrication technology as described in chapter 3.

1.2.3   System overview

The stretchable micro-electrode array chip consists of an elastic freestanding polydimethylsiloxane (PDMS) membrane containing the electrodes, interconencts and micro-features intended to promote cell alignment and adhesion, supported by a silicon frame containing the electrical contact pads. The electrical interconnects extend from the contact-pads on the silicon substrate to the electrodes on the PDMS membrane. Figure 1.6 shows the schematic configuration of the SMEA membranes for two different designs, namely dogbone and circular, together with the optical and SEM micrographs of the surface of the membranes. The design of the membrane shape and interconnect arrangement enables stretching of the membrane by pneumatic inflation without damage to the interconnect tracks (see chapter 2 on mechanical design).
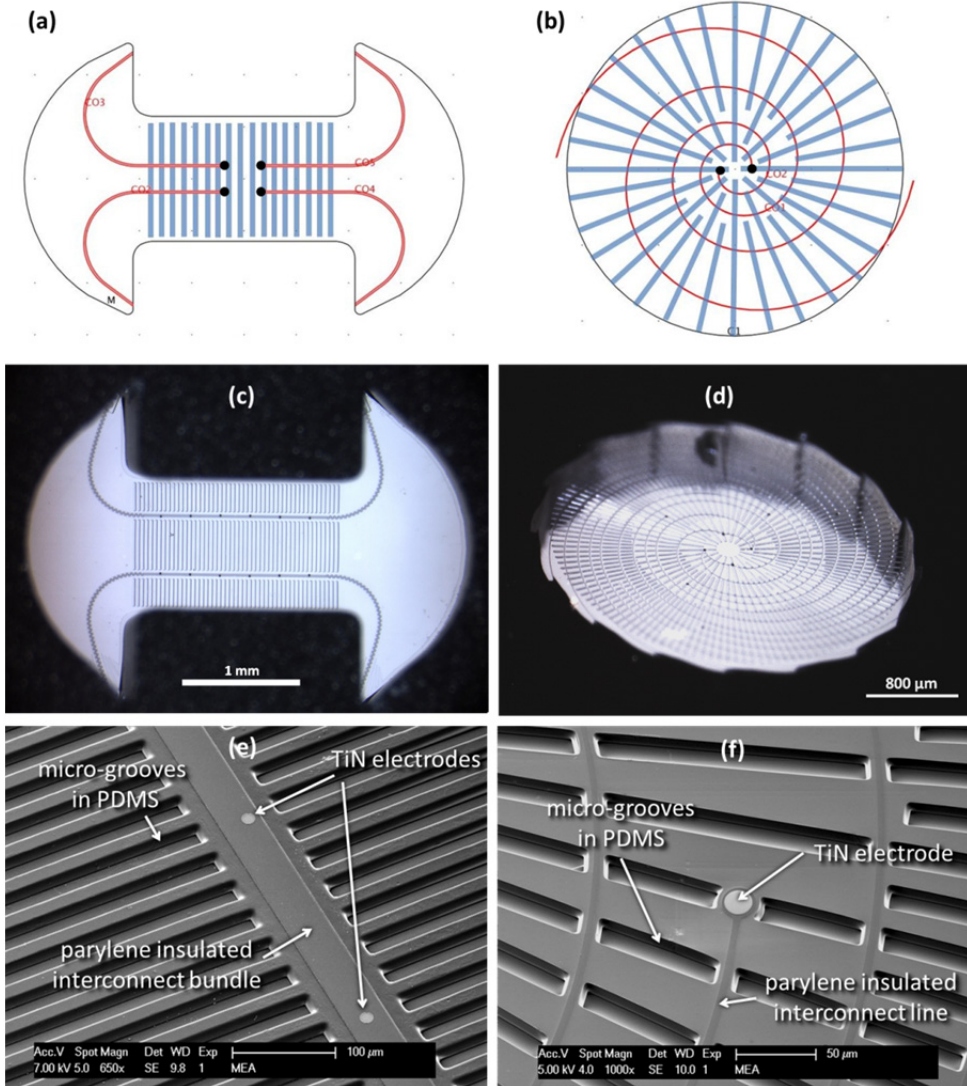
Figure 1.6 (a,b) Schematic representation of SMEA membranes for two different designs, dogbone and circular respectively. The interconnects are shown in red, the electrodes in black and the micro-grooves in blue. Only a subset of the electrodes and interconnects are shown for schematic illustration. (c,d) Optical micrographs of the SMEA membranes. (e,f) SEM micrographs of the SMEA membrane surfaces for the dogbone and circular designs.

The selected material for the electrodes is titanium nitride which is a common electrode metalization for stimulating and recording electrodes, due to intrinsic chemical and mechanical stability [82]. TiN is also a suitable material for micro-fabrication processing due to ease of deposition and patterning. As shown in Figure

1.7 (b) the electrical interconnects are made from TiN on the membrane area and from aluminium on the silicon substrate. The interconnects on the membrane area are fully isolated with parylene which also serves as the mechanical structural material. The isolation is opened at the location of the electrodes to allow direct contact with the cells, as shown in cross-section in Figure 1.7 (c).
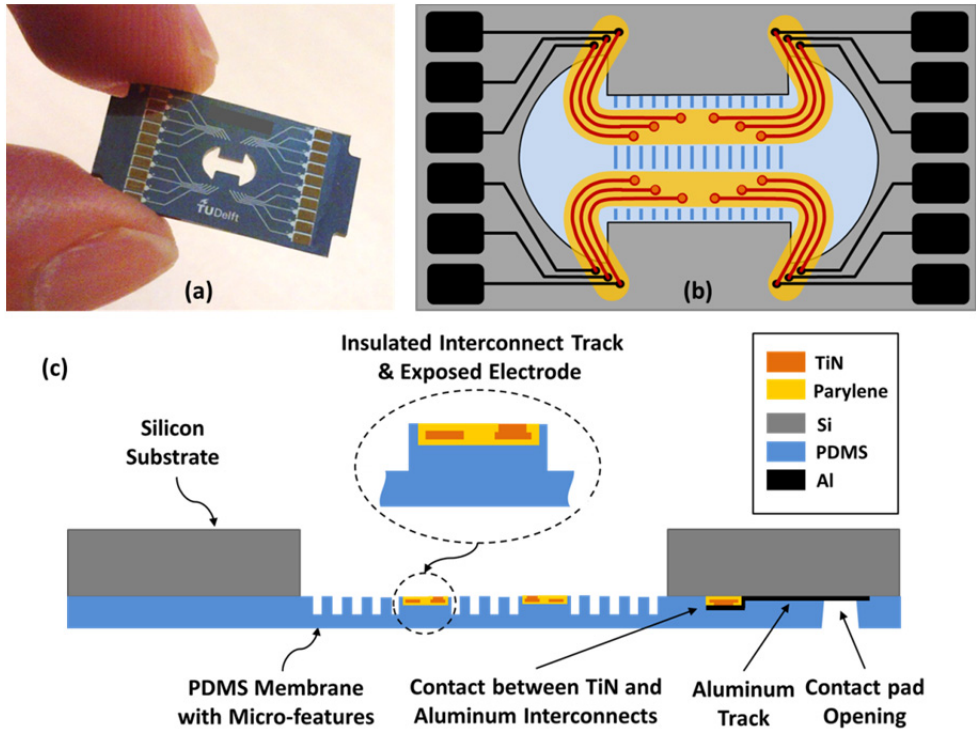
Figure 1.7 (a) Photograph of an SMEA chip with dogbone design. (b) Schematic illustration of the chip's layout. (c) Schematic cross-section view of the chip.

In brief, the microfabrication of the SMEA chips starts by fabricating the electrodes, interconnects, and sacrificial photo-resist micro-molds for the desired micro-features on a silicon wafer. Subsequently, PDMS is applied on top, and finally the silicon substrate is removed from underneath the membrane area by flipping the wafer and deep reactive ion etching (DRIE) of silicon (Figure 1.8 (a)). As a result, the functional side of the membrane resides at the bottom of the deep-etched cavity in the silicon substrate (Figure 1.8 (b)).
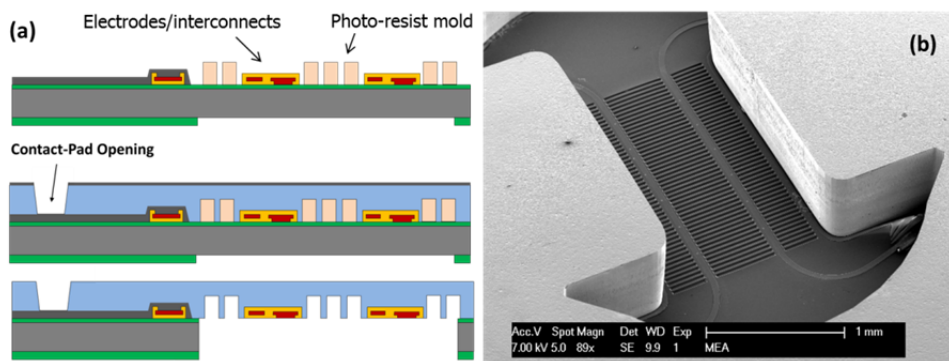
Figure 1.8 (a) summarized microfabrication sequence of SMEA chips. (b) SEM micrograph of the chip from the backside after DRIE etching of silicon.

The SMEA membranes are pneumatically actuated by applying a controlled air pressure to the backside of the membranes, thereby applying physiologically relevant strains to the cultured cells adhering to the membranes (Figure 1.9). The amount of strain in the membrane is calculated from the measured inflation height at the center of the membrane according to a geometrical model as explained in chapter 4 on device characterization.
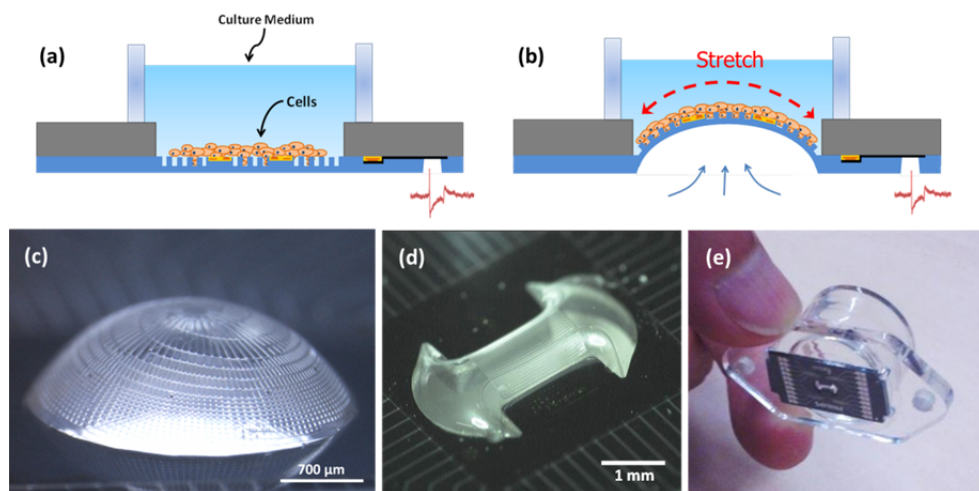
Figure 1.9 (a, b) Pneumatic actuation of the SMEA membrane to apply stretch to the cells. The pictures show the membrane in relaxed and stretched states, respectively. (c, d) Micro-photographs of inflated SMEA membranes with circular and dogbone designs, respectively. (e) Photograph of a chip mounted at the bottom of a culture chamber.

To electrically contact the chips and apply the pneumatic pressure to the backside of the chips an electro-pneumatic adaptor was designed. The adaptor design

enables in situ inverted-microscopy during experiments by providing minimal distance between the membrane and the microscope objective, as illustrated in Figure 1.10 (a). In order to reduce the distance between the objective of the inverted microscope and the membrane to a few millimeters, a pneumatic access channel is milled in the backside of the PCB and sealed with a thin coverslip glass. The chips are pressed and fixed against thin form factor spring-loaded contact pins which come in contact with the contact-pads on the chips, and an elastic O-ring for pneumatic sealing (Figure 1.10 (b-e)). For proper electrical contact, the chips are aligned to the chip-alignment pins by incorporating alignment-notches at the corners of each chip. The from factor of the adaptor is designed to fit seamlessly into commercially available MEA amplifier systems to enable in situ application of pneumatic actuation while performing electrical measurement and stimulation (Figure 1.10 (g)).

1.3   Outline of the thesis

The remaining chapters of this thesis present the design, micro-fabrication and characterization of the stretchable micro-electrode arrays. Chapter 2 discusses the mechanical design methodology used for the electrical interconnects based on principal strains in inflated membranes. The detailed micro-fabrication process and associated challenges are presented in chapter 3. The SMEA chips are electro-chemically and electro-mechanically characterized in chapter 4 to determine the impedance of the electrodes, as well as mechanically induced resistance changes and fatigue life time. The presented cellular experiments in chapter 5 demonstrate the proof of concept with field potential measurements under mechanical stimulation from stem cell derived cardiomyocytes. The thesis ends with conclusions and recommendations for future work.
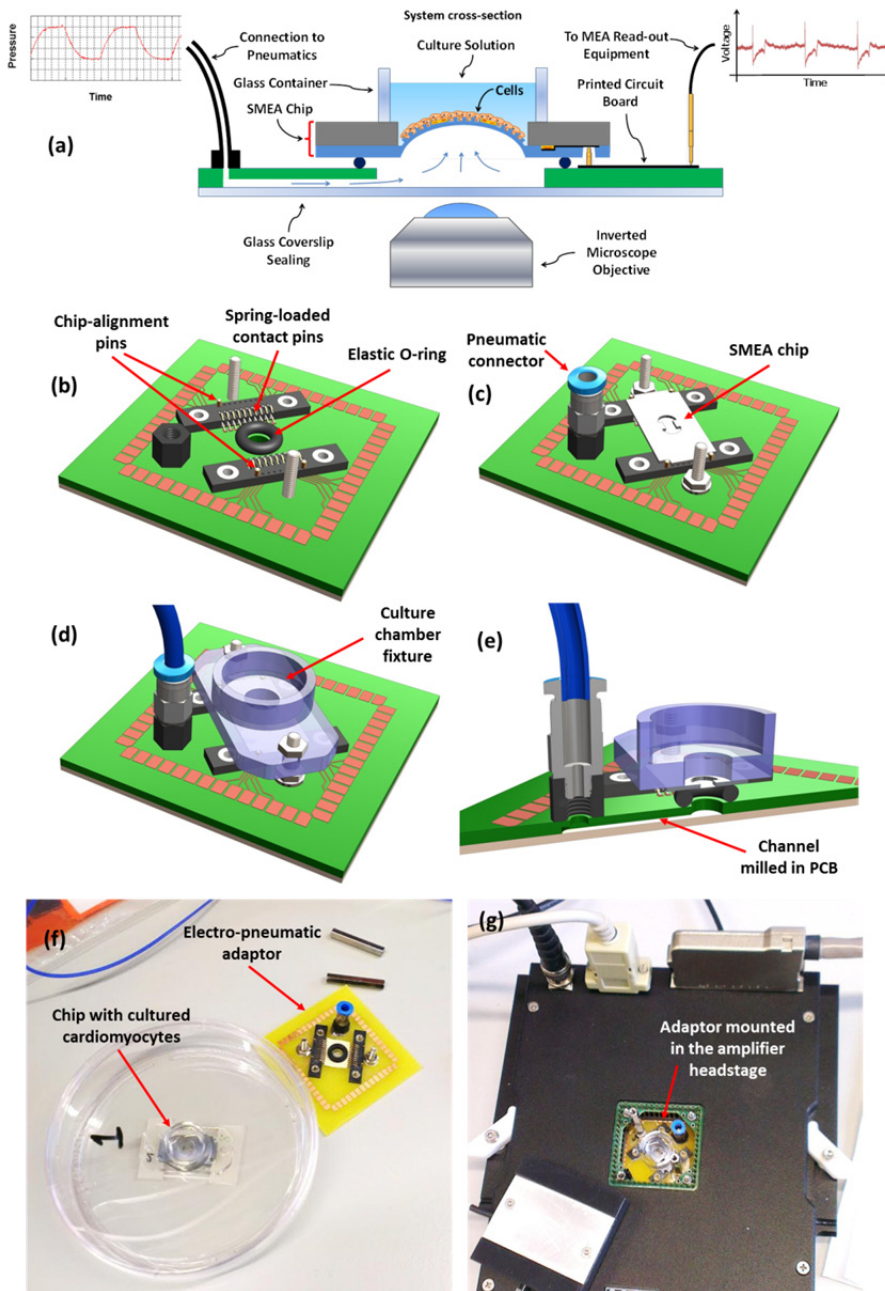
Figure 1.10 (a) Schematic cross-section of the electro-pneumatic adaptor system. (b-e) Illustration of the actual adaptor design elements. (f, g) Adaptor usage: the chips with cultured cells are fixed in the adaptor first. Subsequently, the adaptor is placed in the amplifier headstage for measurements.

Chapter 2 - Mechanical design of the SMEA

The electrical interconnects to the electrodes in the stretchable micro-electrode array chip are designed in such a way that they can withstand the strains in the pneumatically actuated membrane. The conventional method to realize electrical interconnects for stretchable devices is to design them in wavy or horseshoe shapes which accommodate stretching by bending in plane or out of plane. However, as discussed in the introduction chapter, meandering interconnects require a large surface area and alter the mechanical properties of the surface. Therefore, meandering designs for the interconnects are not favorable for the SMEA membranes that are to be used as cell culture substrates.

The approach used to design the electrical interconnects for the SMEA chips to achieve minimal surface area allocation for the interconnect tracks was to determine the proper routes for the interconnects - which result in sufficiently low stress in the tracks - according to the principal strains in inflated membranes obtained from finite element model (FEM) mechanical simulations. The first and second principal strains in the simulated membranes indicate the direction and magnitude of the maximum and minimum in plane perpendicular strains, which are used to determine the proper routes [83]–[85].

After calculation of the direction and magnitude of the first (maximum) and second (minimum) in plane strains, the route of the interconnects were designed in such a way that the interconnect tracks are perpendicular to the first principle strain direction and therefore parallel to the second principal strain direction. In this way, the interconnects experience the maximum strain in the membrane transversally and therefore are robust with respect to it, and should only be mechanically dimensioned properly to withstand the second principal strain that acts on the interconnects longitudinally. This mechanical design approach is illustrated for two different SMEA designs, i.e. the circular and the dogbone designs, in the following sections.

2.1   Circular design

In the circular design the SMEA membrane has a circular shape and the interconnects are designed in the form of spirals. Figure 2.1 shows the geometry of the membrane and the two spiral-shaped interconnects used in the simulations.
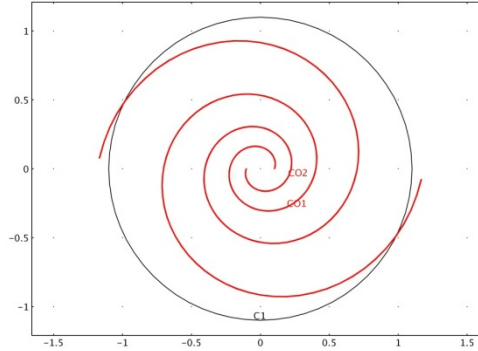
Figure 2.1 The geometry used for the FEM simulation, showing a circular membrane and two spiral-shaped interconnect tracks (the axes scales are in millimeters).

In an inflated circular membrane, the first and second principal strains are in radial and tangential directions, respectively. Figure 2.2 shows the magnitude and direction of the principal strains in a 25 μm thick circular PDMS membrane inflated with 10 kPa pressure.
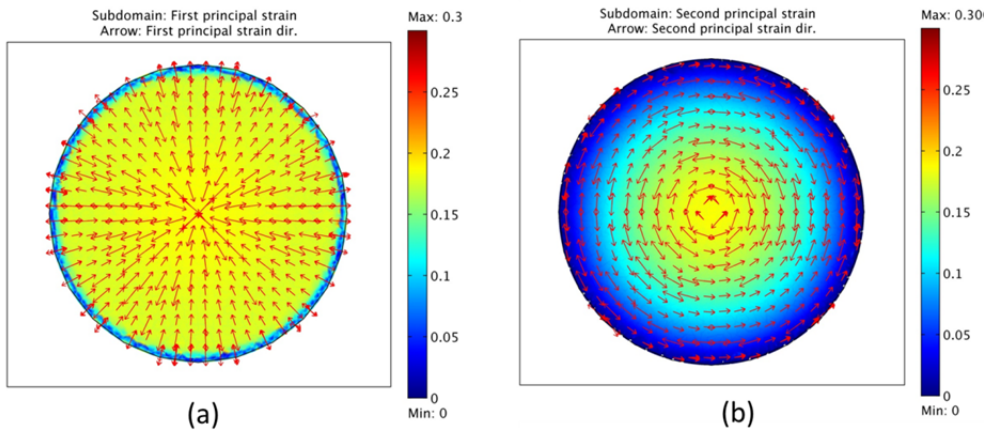
Figure 2.2 The magnitude and direction of (a) first and (b) second principal strains in a circular 25 μm thick PDMS membrane inflated with 10 kPa pressure (PDMS Young's modulus : 1.2 MPa).

By following the aforementioned design approach, to traverse the interconnect lines from the periphery of the membrane to the center perpendicular to the

direction of the first principal strain, the interconnect routes attain a spiral shape. In this manner the interconnect tracks do not restrain the radial stretch in the membrane upon inflation, and therefore are robust with respect to the first principal strain. The spiral interconnects however confine the tangential strain in the membrane which results in stress development in the interconnect tracks. Figures 2.3 (a & b) show the effect of the spiral interconnects on the principal strains in the membrane, and the confinement of the tangential strain by the interconnects compared to that of the plain membrane shown in Figure 2.2 (b). Figure 2.3 (c) shows the developed stress in the interconnect tracks simulated as parylene beams with 4 μm thickness and 5 μm width embedded in the membrane's surface.
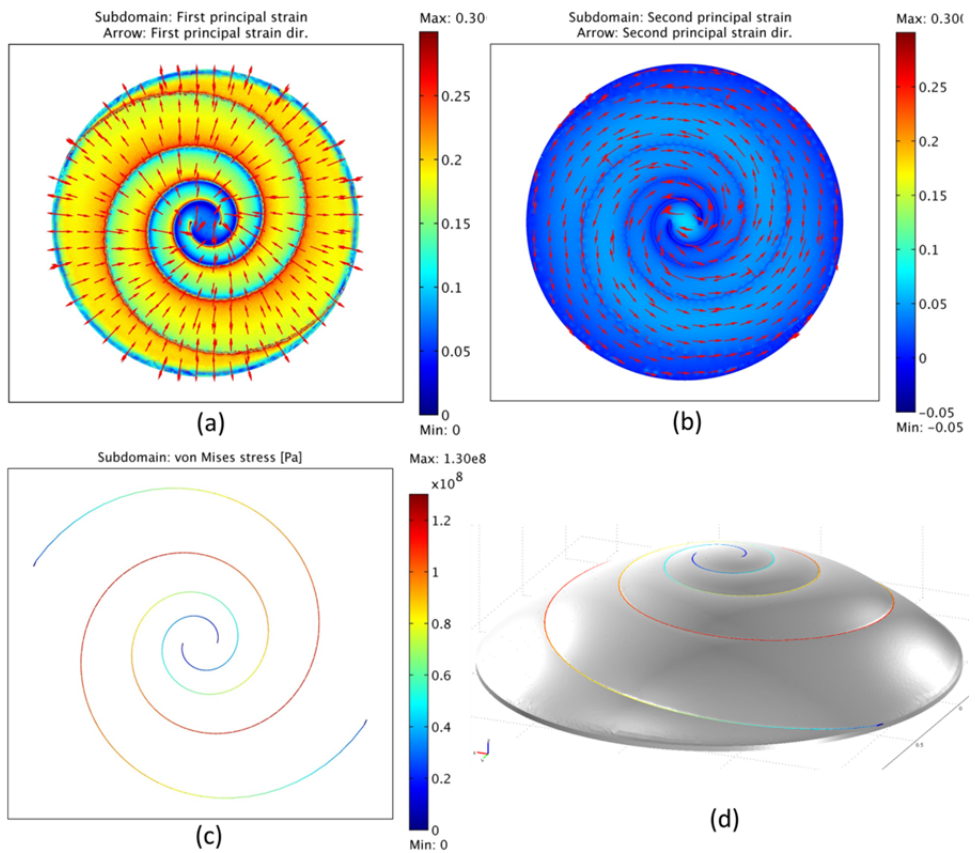
Figure 2.3 (a & b) The magnitude and direction of the first and second principal strains in the circular membrane affected by the spiral interconnects (pressure: 10 kPa). (c) The developed stress in the interconnects tracks due to confining the tangential strain in the membrane. The interconnect tracks were simulated as parylene beams with 4 μm thickness and 5 μm width (parylene Young's modulus : 3.2 GPa).(d) Three dimensional view of the simulated geometry.

The magnitude of the developed stress in the interconnects depends on several factors including the cross sectional area of the tracks, the thickness of the membrane and the amount of inflation indicated by the principal strains in the membrane. For a required amount of inflation in the membrane, the magnitude of the stress in the interconnect tracks should remain below the yield stress of the structural material of the interconnect tracks. The stress in the interconnects can be reduced by either increasing the cross sectional area of the tracks or decreasing the thickness of the membrane, as demonstrated by the simulation results shown in Figure 2.4 compared to that of Figure 2.3 (c) for the same level of inflation height.
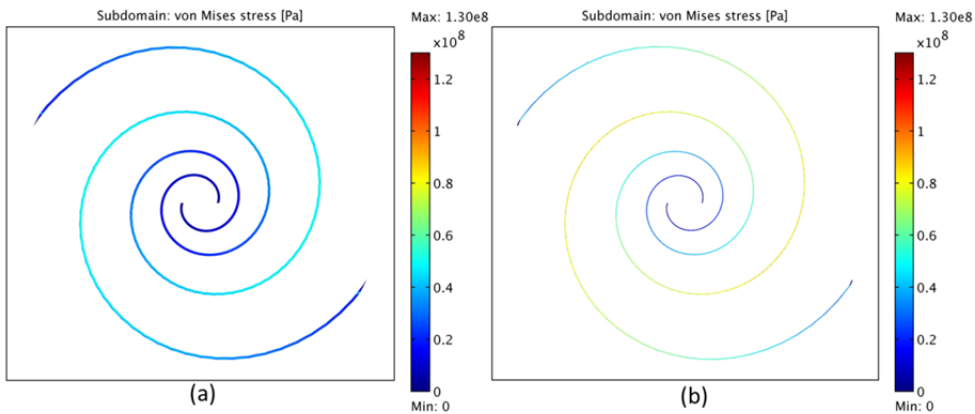
Figure 2.4 Reducing the stress in the interconnects by (a) increasing the width of the tracks from 5 µm to 15 µm (membrane thickness: 25 µm, pressure: 10 kPa), or (b) decreasing the thickness of the membrane to 15 µm. (track width: 5 µm, pressure: 6 kPa). The inflation height and principal strains in the membranes were the same in the simulations. For the thinner membrane less pressure (6 kPa) is required to reach the same inflation height, resulting in lower stress in the interconnect tracks.

In the circular design the tangential (2nd principal) strain in the membrane always results in stress development in the interconnect tracks. Increasing the width of the tracks to reduce the stress results in more surface area occupied by the interconnects, which in the actual chip design containing larger number of interconnect tracks can become prohibitive. Moreover, increasing the thickness of the tracks increases the bending stress (as described later) and can also pose microfabrication processing complications. By altering the shape of the membrane to introduce concave corners in the geometry, it is possible to obtain regions where the 2nd principal strain is virtually zero. Passing the interconnects through such regions results in minimal stress development in the interconnects due to the 2nd principal strain. This concept is illustrated in the next section that discusses the so called "dogbone" design.

2.2   Dogbone design

Figure 2.5 shows the shape of the membrane and the location of the interconnect tracks for the dogbone design. The geometry of the membrane has four concave corners which introduce zero-crossings in the magnitude of the 2nd principal strain as will be explained in the following. The designed tapering at the corners of the dogbone shape provides gradual out of plane bending of the interconnect tracks traversing form the rigid frame to the membrane area, when the membrane is inflated.
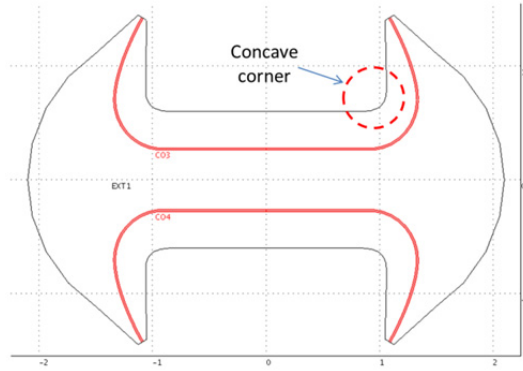
Figure 2.5 The geometry of the dogebone design. The dogbone shaped membrane has four concave corners. The interconnect tracks are denoted in red. One quarter of the geometry is used for the simulations due to axes symmetry (the axes scales are in millimeters).

Figure 2.6 shows the magnitude and direction of the principal strains in one quarter of a plane dogbone-shaped PDMS membrane with thickness of 25 μm inflated with 10 kPa pressure. Following the aforementioned design rule the interconnect routes should be designed perpendicular to the 1st principal strain direction. The black dashed lines in Figure 2.6 (a) denote several possible routes for the interconnect tracks. Since, the 2nd principal strain applies force on the interconnect tracks longitudinally causing stress in the tracks, among the many possible routes for the interconnects the one that passes through the minimal 2nd principal strain magnitude, develops the least amount of stress.

As illustrated in Figure 2.6 (b) the magnitude of the 2nd principal strain is negative in the vicinity of the concave corner and gradually turns positive moving towards the center of the circular region. Consequently, there exists a zero-crossing path where the 2nd principal strain magnitude changes from negative to positive, denoted by the white dashes line in Figure 2.6 (b). Since the relative location of the zero-crossing path remains the same in the intermediate stages of inflation according to

the simulations, this zero-crossing path effectively just tilts out of plane when the membrane is inflated and does not experience stretching.
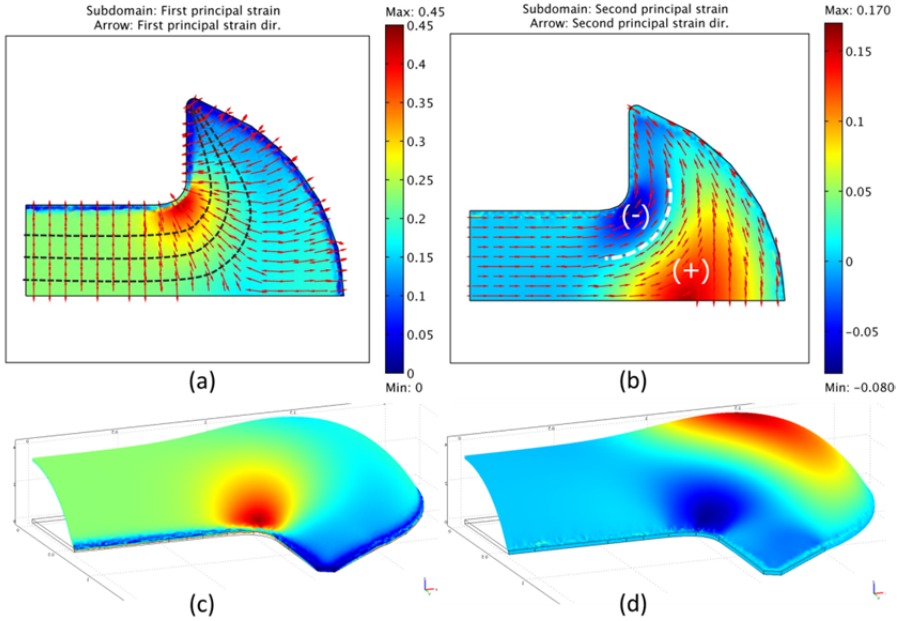
Figure 2.6 Principal strains in one quarter of the inflated dogbone-shaped membrane. (a) Magnitude and direction of the 1st principal strain. Several possible routes for the interconnect tracks perpendicular to the direction of the 1st principal strain are denoted by the black dashed lines. (b) Magnitude and direction of the 2nd principal strain. The zero-crossing path in the magnitude of the 2nd principal strain is denoted by the white dashes line. The relative location of the zero-crossing path remains the same in the intermediate stages of inflation. (c&d) Three dimensional views of the simulated membrane inflation for illustration.

For the route passing through the zero-crossing, the magnitude of the 2nd principal strain is virtually zero, resulting in minimal stress in the interconnects compared to other routes as demonstrated in Figure 2.7. The first row of Figure 2.7 shows the magnitude of the 2nd principal strain in two inflated plane membranes. The second row shows the influence of the addition of the interconnect tracks on the 2nd principal strain distribution in the membranes compared to that of the plane membranes for two different interconnect routes. For image (c) the interconnect track passes through the 2nd principal strain zero-crossing while for image (d) this is not the case. The change in the strain distribution in image (d) compared to that of the plane membrane in image (b) indicates that the interconnect track confines the strain in the membrane resulting in stress development in the track as shown in image (f).
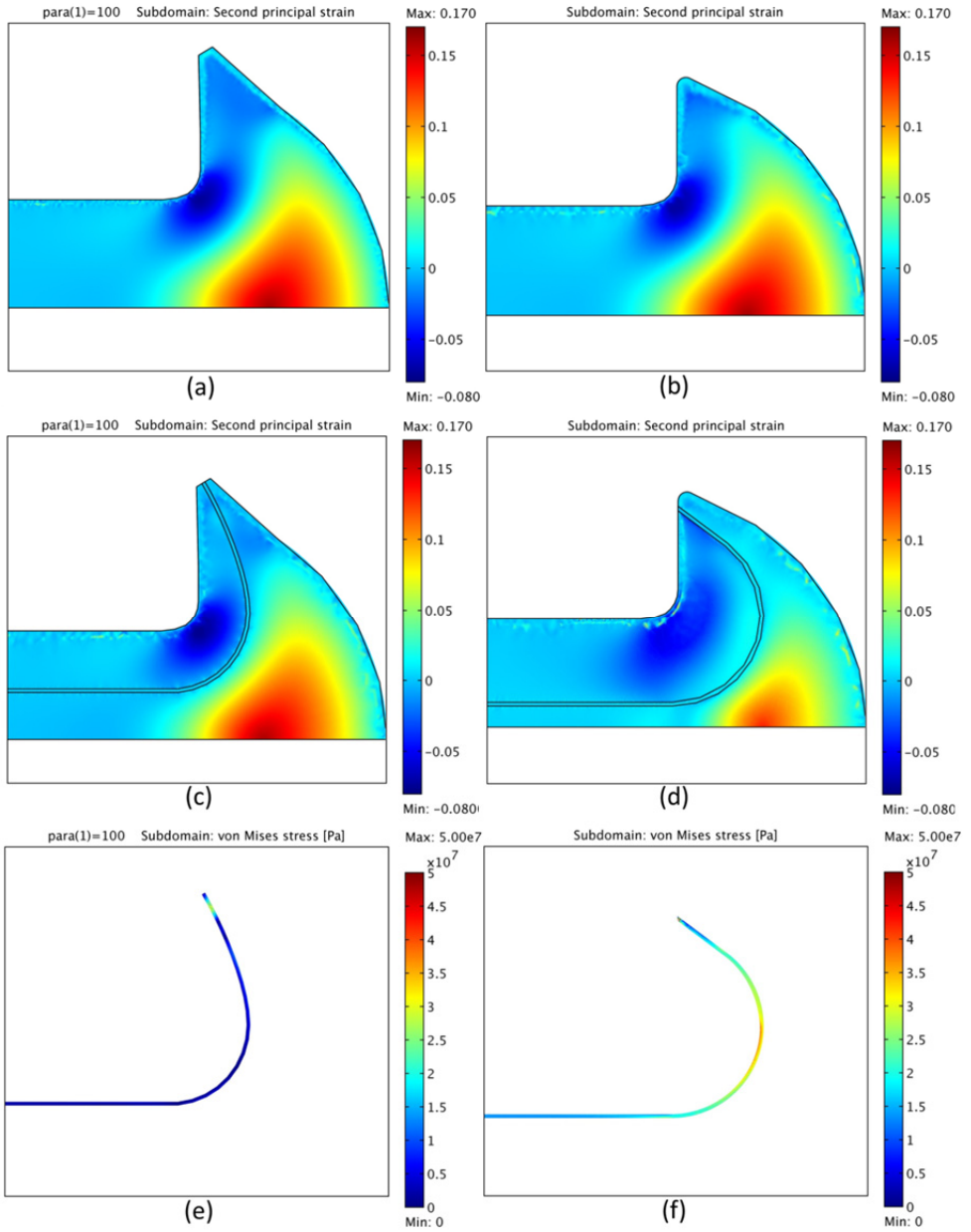
Figure 2.7 (a & b) The 2nd principal strain magnitude distribution in plane membranes. (c & d) The influence of the interconnect tracks on the 2nd principal strain distribution in the membranes shown in images a and b, respectively. In image c the track is passing through the 2nd principal strain zero-crossing, but in image d it does not. (e & f) The developed stress in the interconnect tracks (20 μm in width, 4 μm in thickness) in images c and d, respectively.

However, comparing images (a) and (c) for the interconnect track that passes through the zero-crossing shows that the strain distributions in the plane membrane and the membrane with the interconnect track are almost identical, demonstrating that the track does not confine the strain in the membrane resulting in substantial reduction of the stress in the track as shown in image (e) compared to that of image (f).

In the dogbone design the strain in the rectangular middle part of the geometry - which is the functional area of the SMEA containing the electrodes - is almost unidirectional as indicated by the magnitudes of the 1st and 2nd principal strains in Figure 2.6. Therefore, as previously described in the introduction chapter, by either vertically or horizontally orienting the cells in this region using proper micro-features, longitudinal or transversal strains can be applied to the cultured cells, respectively. For the circular design however, the strain distribution is not homogeneous as shown in Figure 2.3 (a).

2.3　Bending of the interconnects

The out-of-plane bending of the interconnect tracks at the transition locations from the PDMS membrane to the rigid silicon frame, causes bending stress in the interconnects. The bending stress depends on the thickness of the track and the bending radius according to the following relation:

$$\sigma = E\frac{t}{r} \tag{2.1}$$

In which E is the Young's modulus of the track material, t the thickness form the mid-plane (half of the total thickness), and r the bending radius. Therefore, for a parylene beam with 4 μm thickness, the minimum bending radius to remain below the yield strength of parylene (~ 55 MPa [86]) is 170 μm. For the dogbone design the tapering at the corners of the dogbone provides gradual bending of the interconnects and increases the bending radius, as illustrated in Figure 2.8 (top). The bending stress can be further reduced by modulating the stiffness of the membrane at the bending locations by locally incorporating parylene flaps in the design as illustrated in Figure 2.8 (bottom). In this manner instead of an abrupt change in the stiffness from the membrane to the silicon frame, the stiffness gradually increases resulting in a more gradual bending of the track.
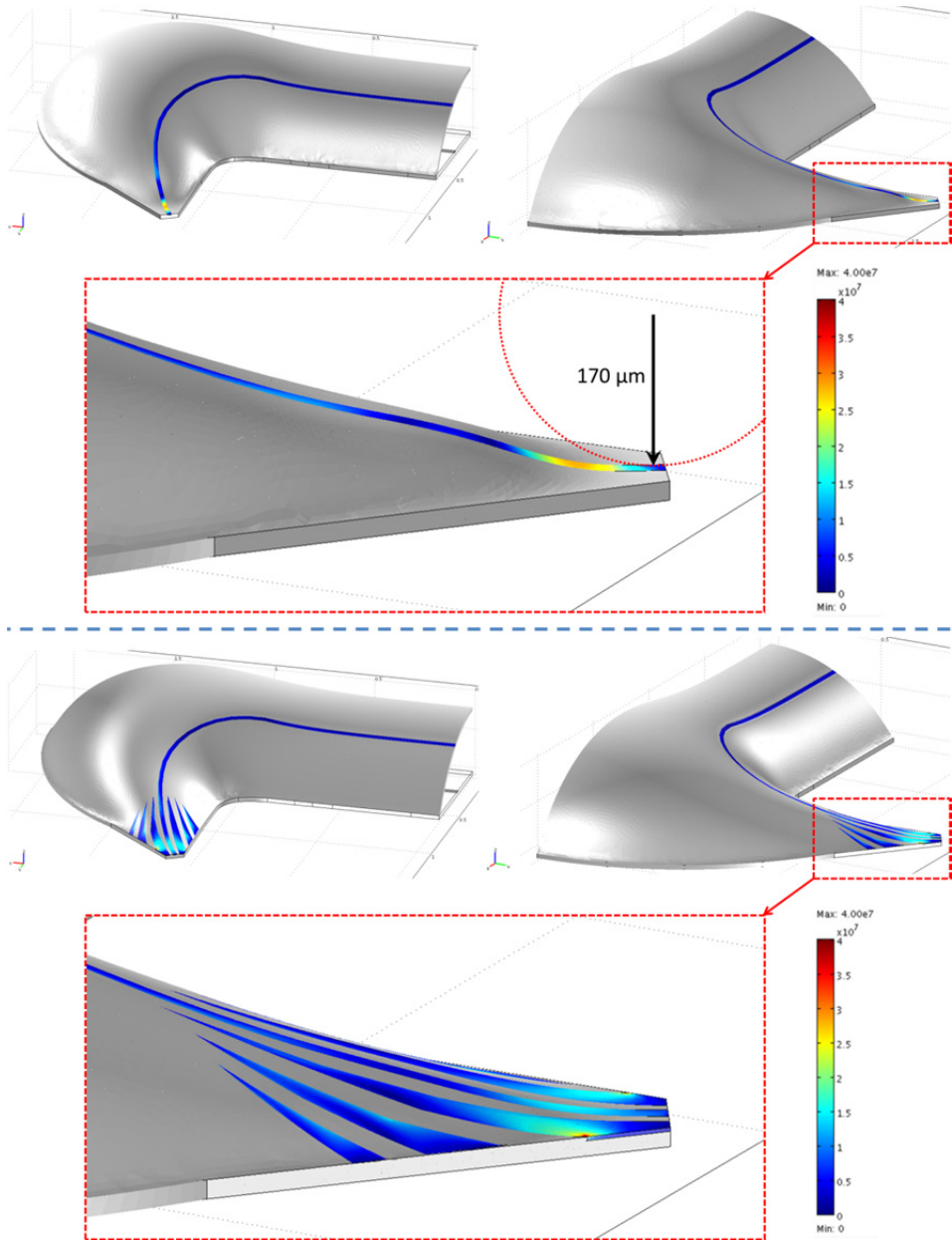
Figure 2.8 Three dimensional views of the interconnect track bending at the transition locations from the membrane to the rigid frame for (top) normal transition and (bottom) mild transition by using parylene flaps to gradually increase the stiffness, resulting in larger bending radius and decreased stress in the interconnect track.

To increase the bending radius at the transition locations from the membrane to the silicon frame for the circular design, it is possible to incorporate recessions in the silicon substrate as depicted in the circular chip layout shown in Figure 2.9.
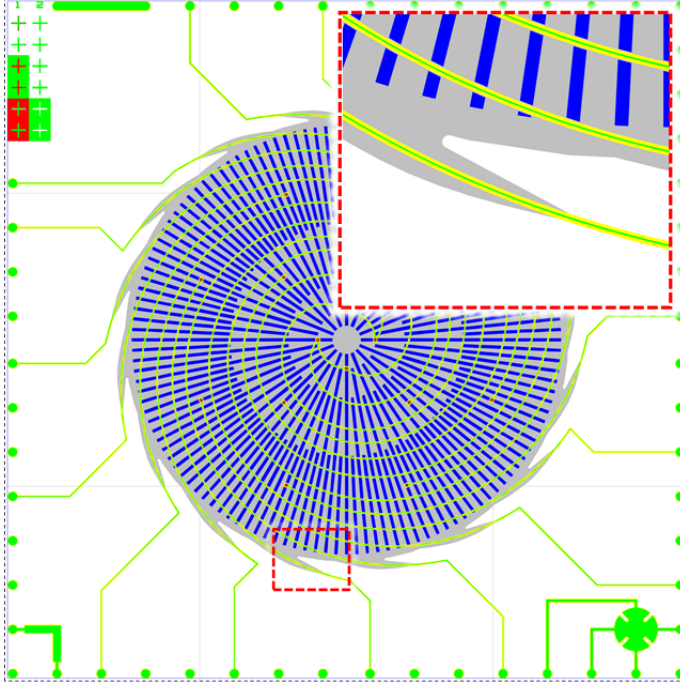
Figure 2.9 Actual layout of a circular design incorporating recessions in the silicon substrate to increase the bending radius. The inset shows the enlarged view of a recession denoted by the red box.

2.4   Discussion

Since the membrane deflection in the SMEA is much larger than the thickness of the membrane and the neutral plane undergoes significant stretching, a large strain model was used in the simulations. In order to verify the validity of the large strain COMSOL simulations, the deflection of a simple circular membrane was compared to a stablished numerical solution. The exact numerical equation for a thin, circular membrane deflection with respect to the applied pressure for the case of large strains is expressed by the following equation [87]:

$$\Delta p = 4 \frac{d_m t_m}{r_m} \left(\frac{2}{3} \frac{d_m^2}{r_m^2} \frac{E_m}{1.026 - 0.793 v_m - 0.233 v_m^2} \right) \qquad (2.2)$$

in which Δp, d_m, t_m, r_m, E_m and v_m, represent the applied pressure, displacement of the membrane's center, thickness, radius, Young's modulus and Poisson's ratio of the membrane respectively. The obtained value from Equation 2.2 for center displacement using the same parameter values used in the simulation of the plane circular membrane in section 2.1 is 514 µm which is within -4% accuracy from the value obtained from the simulation, 532 µm.

For the dogbone design the simulations showed a transition from negative values for the 2nd principal strain in the vicinity of the concave corner, to positive values in the circular region of the membrane. As discussed before, this transition region provides a favorable path for the interconnects. While the occurrence of this transition near concave corners can be studied theoretically, in order to have more numerical evidence, the dogbone membrane was also simulated using shell elements[1]. The simulations confirmed the existence of the transition region as demonstrated in Figure 2.10. In order to experimentally find the exact transition route on the fabricated chips, Digital Image Correlation (DIC) techniques can be used [88].
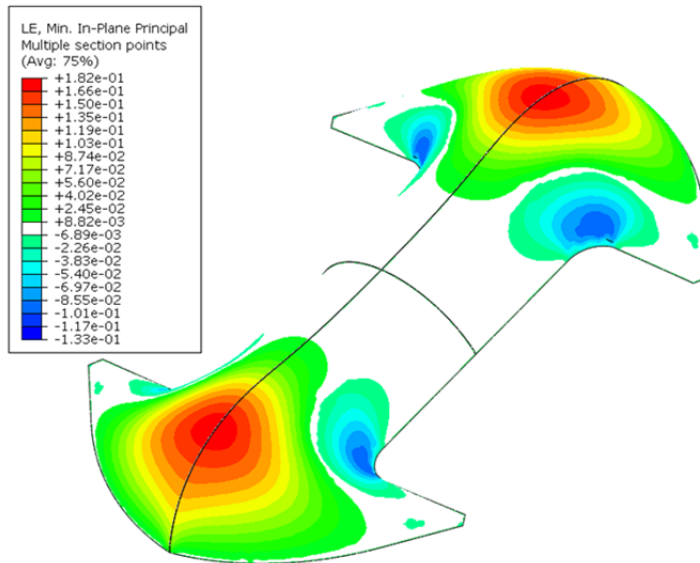
Figure 2.10 The second principal strain magnitude distribution in the dogbone shaped membrane simulated using shell elements. (pressure:10 kPa, membrane thickness: 16 µm, Young's modulus: 1.2 MPa, Poisson ratio: 0.5)[1]. The region with 2nd principal values between -0.7% and +0.8% is denoted in white.

---

[1] The simulation was carried out by the FEM modeling company Reden.

2.5   Summary

This chapter presented a novel approach to design the electrical interconnects for the stretchable MEA chips. In order to dedicate minimal surface area to the interconnects, the optimal routes for the interconnects which result in minimal stress in the tracks were determined based on the magnitude and direction of the 1st and 2nd principal strains in inflated membranes obtained from mechanical FEM simulations. The interconnect routes were designed to be perpendicular to the 1st principal strain direction and if possible pass through regions with minimal 2nd principal strain magnitude.

Two different designs for the SMEAs were presented. In the circular design the interconnects have a spiral shape almost perpendicular to the direction of the 1st principal strain and they need to be dimensioned mechanically to withstand the 2nd principal strain. In the dogbone design the concave corners in the geometry of the membrane result in regions with virtually zero 2nd principal strain magnitude providing optimal locations for the interconnect tracks.

While for the circular design the tangential strain in the membrane always results in stress in the interconnect tracks, in the dogbone design due to routing the interconnects through the 2nd principal strain zero-crossing higher levels of strain in the membrane are achievable with less stress development in the interconnect tracks, compared to the circular design. Moreover, the dogbone design provides unidirectional strain in the functional area of the membrane containing the electrodes which enables directional stretching of the cells. Therefore, for the electrophysiological measurements under stretch and the electromechanical characterization presented in the following chapters the dogbone design was preferred.

Chapter 3 - Microfabrication

In this chapter the microfabrication process for the Stretchable Micro-Electrode Arrays (SMEAs) is presented. In order to enable large scale production of the SMEAs a manufacturable fabrication method was developed. Commonly, fabricating stretchable devices involves processing on top of silicone elastomers. To avoid the problems normally associated with thin film processing on top of elastomers - originating from their relative softness and high thermal expansion coefficient - an "elastomer last" approach was employed for embedding the electrodes and electrical interconnects in the stretchable membrane.

Briefly, in this approach all the micro-structures including the electrodes, electrical interconnects and sacrificial photo resist molds for the surface micro-features are initially fabricated on a silicon wafer. A thin layer of elastomer is then applied on top of the fabricated structures, and subsequently the structures are transferred to the elastomeric membrane by removal of the underlying silicon substrate using Deep Reactive Ion Etching (DRIE) from the backside and dissolving the sacrificial photo resist molds. Figure 3.1 shows SEM micrographs of fully processed SMEA membranes for the dogbone and circular designs.

3.1   Overview

Figures 3.2 (a & b) show the actual and schematic layouts of the chips with the dogbone-shaped membrane. The deep etched cavity in the center of the chips is covered with the PDMS membrane containing the electrode array and the interconnects. The electrodes and the corresponding electrical interconnects on the membrane are fabricated from titanium nitride (TiN) and electrically insulated with parylene except at the electrode locations. Outside the membrane area the contact pads and electrical interconnects are fabricated form aluminum.

Figures 3.2 (c & d) show optical micrographs of the SMEA membrane containing 12 electrodes (12 µm in diameter) arranged in two rows, transversal micro-grooves (20 µm in width and 12 µm in depth), and the interconnects (2 µm in width) visible through the optically transparent parylene insulation. The schematic layout of the

chips shown in figure 3.2b is used as a reference throughout the text of this chapter to illustrate the lithography masks used in each stage of microfabrication.
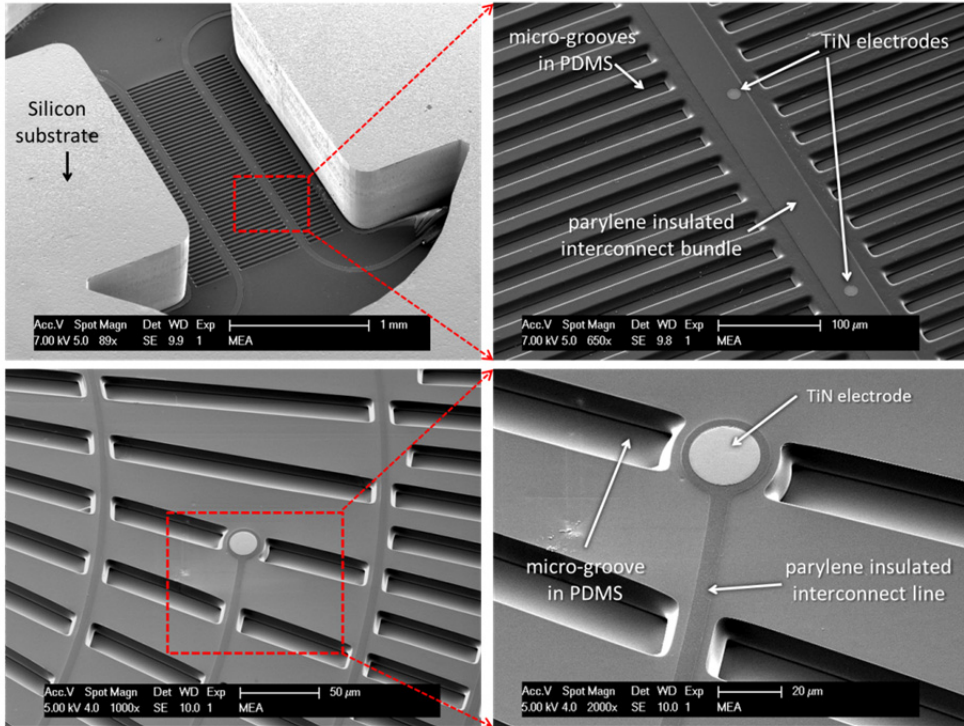
Figure 3.1 SEM micrographs of SMEA membranes. (top) A dogbone shaped membrane at the bottom of the DRIE etched cavity in the silicon substrate, containing the micro-electrode array and transversal micro-grooves. (bottom) A part of a circular membrane with spiral-shaped interconnects and radial micro-grooves. The electrodes and electrical interconnects on the membranes are fabricated from titanium nitride, and the interconnects are electrically insulated with parylene.
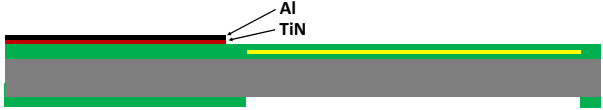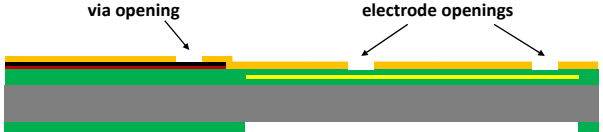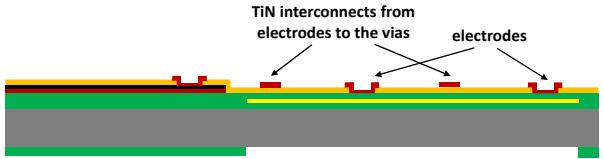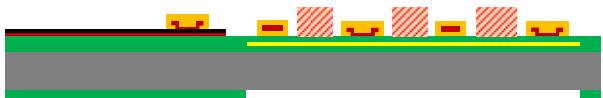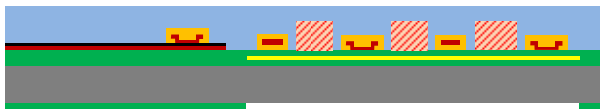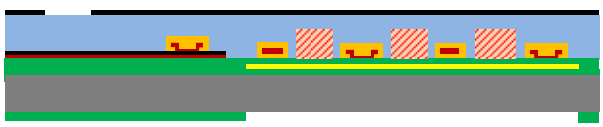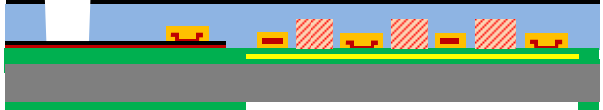
The microfabrication process steps are depicted schematically in table 3.1. The process flow is divided into several sequential stages and explained in the following sections, together with the involved processing challenges and the proposed solutions. The detailed microfabrication flow parameters are presented in appendix 1.
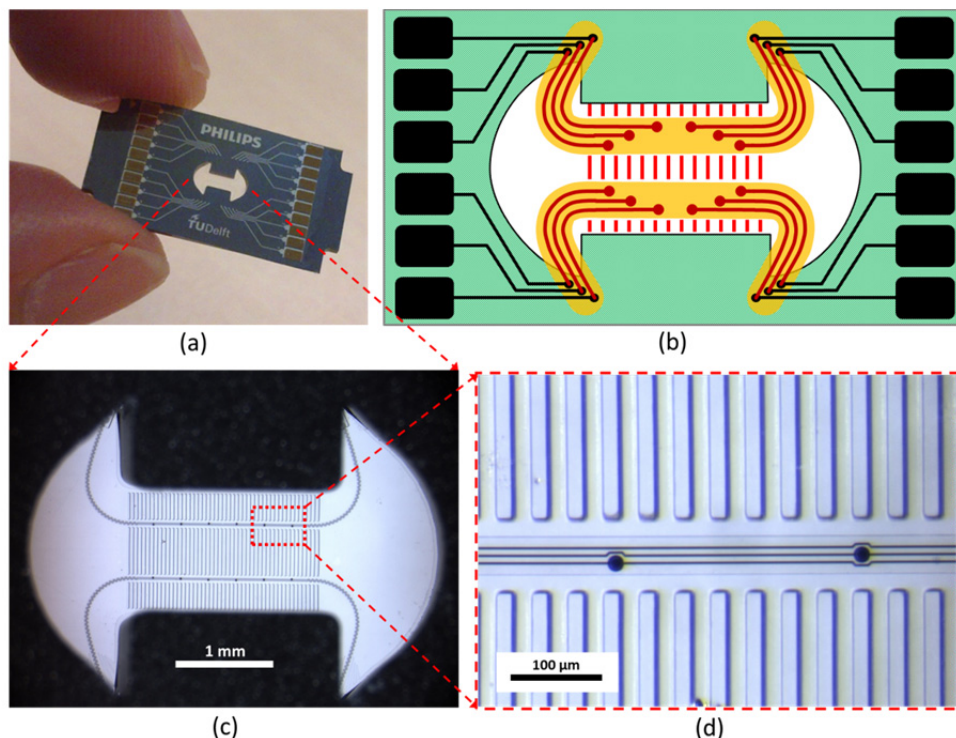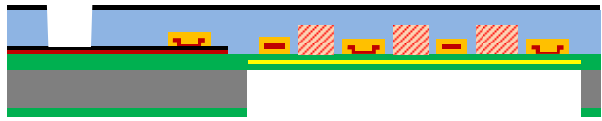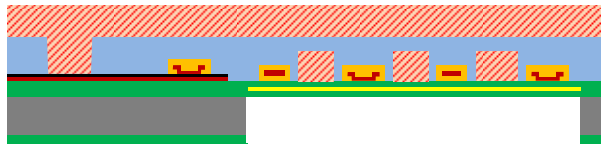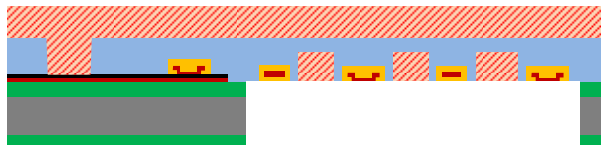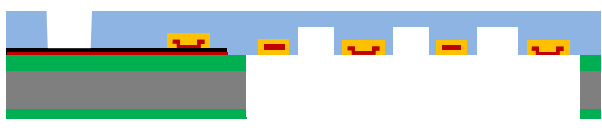
Figure 3.2 (a) A picture of the fully fabricated SMEA chip with a dogbone-shaped membrane. The deep etched cavity in the center of the chip is covered with the PDMS membrane containing the electrode array and interconnects (not visible in the picture due to small size of the structures) (b) The schematic layout of the SMEA chip for the dogbone device. The electrodes and interconnect on the membrane are fabricated from TiN and insulated with parylene. Outside the membrane area the interconnects and contact pads are fabricated from aluminum. The transversal grooves in the membrane are depicted with red vertical lines. (c, d) Optical micrographs of the SMEA membrane with transversal micro-grooves imaged from the backside of the chip. In the right image the interconnects to the electrodes are visible through the optically transparent parylene insulation.

Table 3.1 Fabrication sequence schematic cross section diagram. The structures are not drawn according to the actual layouts and scales.

#	Process step cross section	Description
1		Oxide deposited on the frontside as etch stop and on the backside as hard etch mask, patterned to define the membrane area (oxide shown in green and silicon in gray).

2		Buried titanium UV block layer fabricated (Ti shown in yellow).
3	**Al** **TiN**	TiN/Al interconnect bilayer is deposited and patterned (Al shown in balck and TiN in red).
4	**via opening** **electrode openings**	First layer of parylene insulation is deposited and opened for the electrodes and vias to the Al interconnects (parylene shown in yellow).
5	**TiN interconnects from electrodes to the vias** **electrodes**	TiN is deposited and patterned to define the interconnects and electrodes.
6		2nd layer of parylene is deposited and patterned to electrically insulate the interconnects and electrodes from the top side.
7		Photoresist is spin coated and patterned to form the sacrificial mold for the surface micro-features.
8		PDMS is spin coated and cured.
9		Al is deposited on PDMS and patterned as the hard etch mask for PDMS dry etching, and anti-stiction layer during later stage silicon deep etching from the backside.
10		PDMS is dry etched using the Al hard etch mask, stopping on the Al contact pads.

11		Silicon is deep etched from the back side through the wafer stopping on the frontside oxide.
12		A thick photoresist layer is spray coated on the PDMS as a mechanical support layer during wet etching of underlying Oxide/Ti/Oxide stack.
13		Oxide/Ti/Oxide layer is wet etched in buffered hydrofluoric acid.
14		The photo resist micro-molds and the mechanical support layer are dissolved in acetone to fully release the SMEA membrane.

3.2   Initial preparatory steps

This section explains the initial fabrication steps which are carried out in advance to prepare the wafers for certain steps in later stages of the processing.

3.2.1   Silicon DRIE etch stop and hard etch mask (step 1)

In order to prepare the wafers for the through wafer DRIE (Deep Reactive Ion Etching) of silicon in step 11 of microfabrication, a PECVD silicon oxide hard etch mask on the backside of the wafers, and etch stop layer on the front side are deposited. The hard etch mask on the back side is patterned by dry etching the oxide, to define the area underneath the membranes where the silicon is removed.

Generally, either thermal or PECVD oxides can be used as the etch stop layer for DRIE. Thermal oxide develops a high level of compressive residual stress due to increase in volume when silicon is oxidized. However, the etch stop oxide layer is required to have minimal residual compressive stress, to prevent buckling of the oxide layer after removal of the underlying silicon, as shown in figure 3.3.

Buckling of the oxide layer results in crack formation in the device layers and consequently damage to the interconnect tracks.
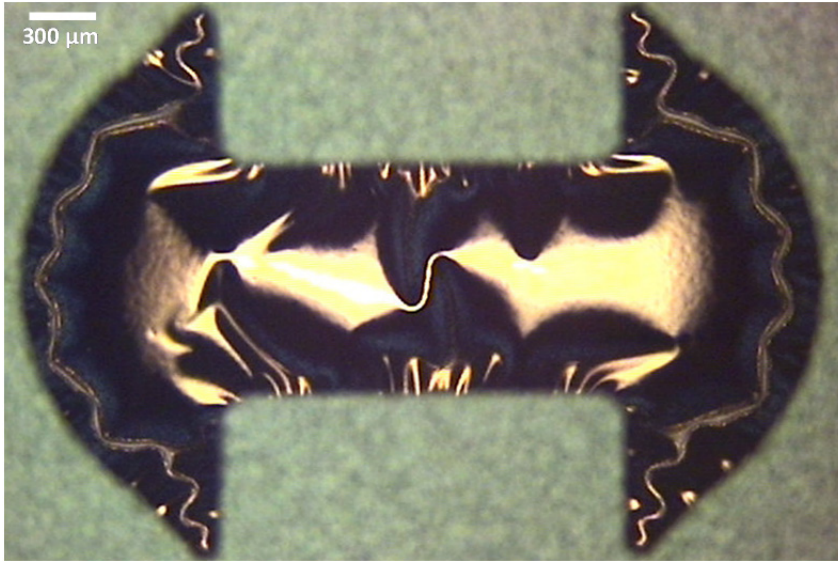
Figure 3.3 Optical microphotograph from the backside of the wafer after through wafer deep etching of silicon showing the buckling of the released membrane due to compressive stress in the 1µm thick thermal oxide etch stop layer.

Therefore, for the etch stop layer PECVD oxide was used. The oxide was deposited using process conditions tuned to result in minimal residual stress. The residual compressive stress in the PECVD oxide layers measured from the wafer bow was ~11 MPa which is more than an order of magnitude smaller than that of thermal oxide (250-300 MPa) [89].

A thickness of 1 µm is sufficient for the etch stop oxide layer. However, the residual stress in the PECVD oxide was still large enough to cause buckling in the 1µm thick oxide layer after removal of the underlying silicon. Since, the critical buckling stress is proportional to the layer thickness squared [90], the etch stop oxide layer thickness was increased to 2µm, resulting in completely flat membranes after silicon deep etching.

3.2.1.1   Wafer breaking slits and alignment notches

The backside oxide mask also contains structures for wafer breaking and alignment (figure 3.4). The fully fabricated SMEA chips contain thin free standing

membranes. Consequently, normal wafer dicing techniques cannot be used to separate the chips at the end of microfabrication. Therefore, to separate the chips, slits are fabricated in the wafers at the boundary of each chip, such that the fully processed wafers can be cleaved along these slits by applying mechanical force, in a similar manner to breaking a chocolate bar. Also, for accurate alignment of the chips in the electro-pneumatic holder, alignment notches are fabricated at the corners of the chips.

To fabricate the slits, narrow 5 µm wide lines are etched in the backside oxide mask. Subsequently, during DRIE etching of the wafers in step 11 of microfabrication, due to etch lag for small feature sizes, the narrow lines are only etched to a depth of approximately 300 µm while the larger open areas are etched completely through the wafer (670 µm). The width of the slits was determined such that the resulting slit depth would not compromise the mechanical integrity of the wafers for further processing.

3.2.2   UV blocking layer (step 2)

To fabricate the micro-features in the membrane's surface, photoresist is used as a sacrificial inverse mold. The resist mold is eventually dissolved in acetone after through wafer etching and removal of the underlying etch stop layer as briefly depicted in figure 3.5 (top). During through wafer etching of the silicon, the deep UV content of the plasma (wavelengths < 250 nm) passing through the oxide etch stop layer results in heavy cross-linking of a thin layer of the photo resist [91]. This cross-linked layer is undissolvable in acetone and forms remnants as shown in figure 3.5 (bottom). In order to prevent UV exposure of the photoresist structures, a buried 100 nm thick layer of titanium is incorporated in the etch stop layer to block the UV content of the plasma, as shown schematically in step 2 of the microfabrication. Titanium was chosen for this purpose, since it can be readily wet etched together with the etch stop silicon oxide in hydrofluoric acid in step 13 of the microfabrication.

Titanium is sputter deposited on the already deposited 1 µm thick PECVD oxide layer and patterned in chlorine plasma using a resist mask to overlap the projected membrane area. Subsequently, a second 1 µm thick layer of PECVD oxide is deposited on top of the Ti layer to provide a silicon oxide surface chemistry for further processing.
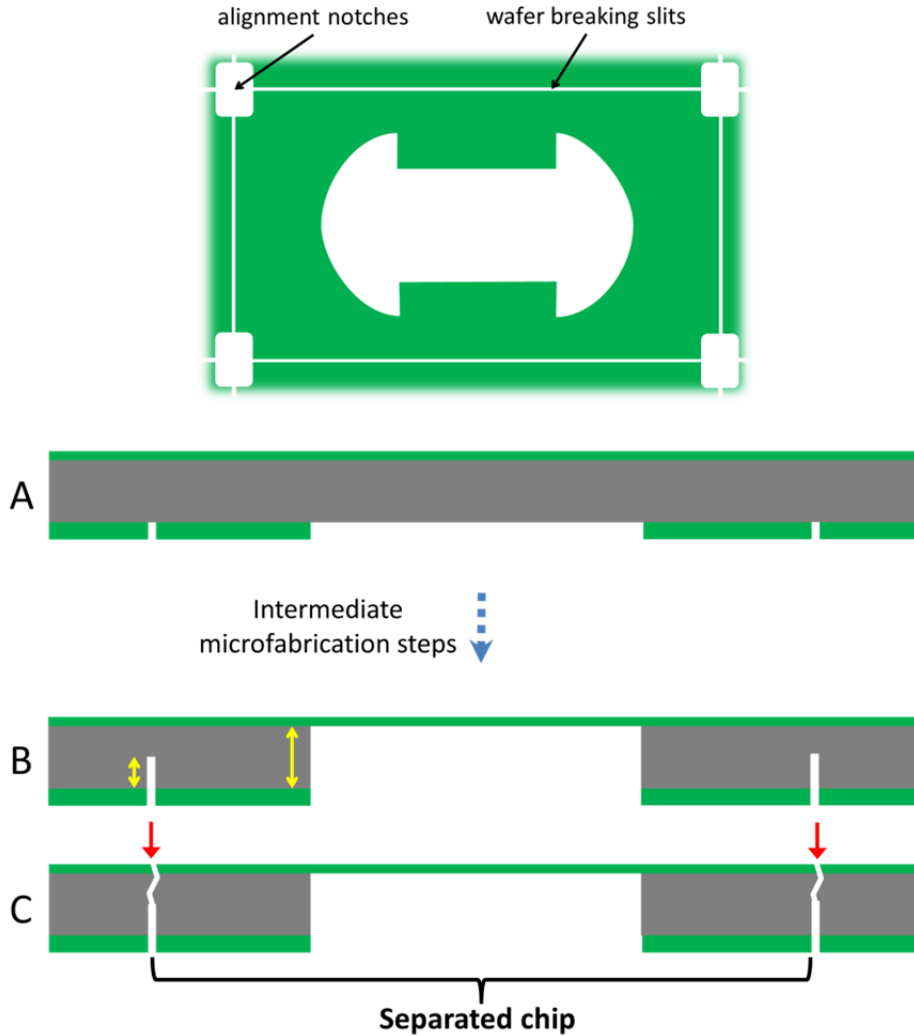
Figure 3.4 (top) Schematic layout of the backside oxide mask for each chip. The narrow lines at the boundary of the chips define the wafer breaking slits, and the openings at the corners define the alignment notched. (bottom) Schematic cross-section view of the wafer breaking slits fabrication (the microstructures on top of the wafer are not shown for simplicity). The backside oxide mask is first patterned. The slits are then formed during a later stage DRIE etching of silicon, as a results of the etch lag for small openings. The fabricated slits are then used to separate the individual dies by applying mechanical force, as shown in step C.
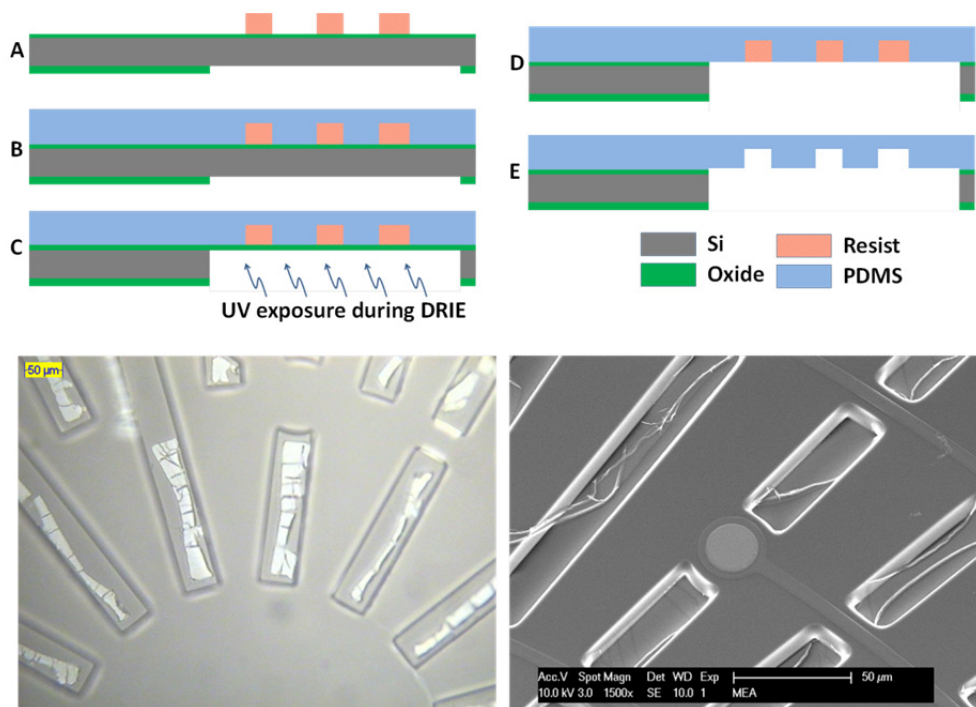
Figure 3.5 (top) Simplified schematic process flow for the fabrication of micro-features in a membrane by using photoresist as the sacrificial mold. The UV content of the plasma during DRIE etching (step C) passing through the oxide layer causes heavy cross-linking of the resist. (bottom) Optical and SEM micrographs of SMEA membranes showing remnants of UV cross-linked photo resist in the micro-grooves, not dissolved in acetone.

3.2.3 Interconnects from the membrane to the contact pads (step 3)

For the electrical interconnects outside the membrane area aluminum was used, which has an order of magnitude smaller resistivity (2.8μΩ.cm) than TiN (30 μΩ.cm). Moreover, Al was also used for the contact pads at the periphery of the chips, since it is a suitable material for wire bonding, enabling optional wire bonding of the chips to carrier PCBs.

The Al contact pads are prone to scratching when frequently interfaced using spring load contact pins in the electro-pneumatic holder during characterization tests and cellular experiments. Therefore, a hard and resilient layer of TiN was inserted in between the Al layer and the underlying oxide to provide a mechanically stable conductive layer for electrical interfacing with contact pins.

In step 3 of the microfabrication a TiN (100nm)/Al (300 nm) bilayer is sputter deposited in succession and subsequently patterned together by dry etching in chlorine plasma using a resist mask (figure 3.6). The Al layer is thick enough for wire bonding even after the wet etching of the antistiction Al layer in step 12 which also results in some etching of the bondpads.
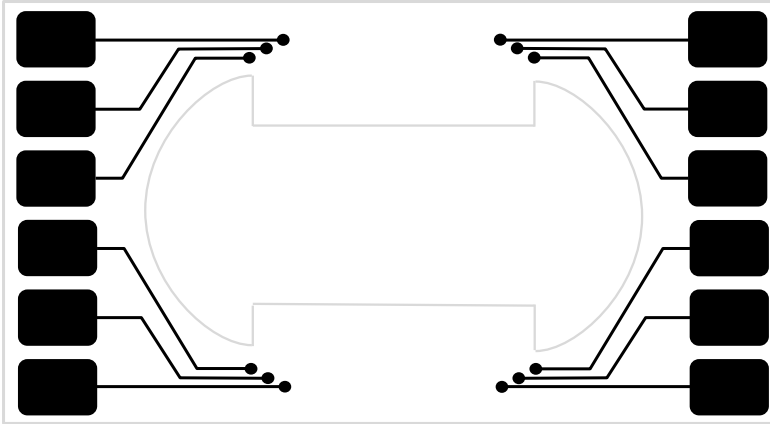
Figure 3.6 Schematic lithography mask for TiN/Al interconnects.

3.3   Fabricating the flexible interconnect stack and the electrodes

The flexible interconnects on the membrane are fabricated as a parylene/TiN/parylene stack. TiN is used as the conductive material for the electrodes and interconnects and parylene is used for electrical insulation and as mechanical structural material for the interconnects. The parylene layers are 2 µm thick each and the TiN layer is 100 nm thick. Less total thickness for the interconnect stack provides more flexibility for the interconnects. However, since the interconnects are bonded to the membrane and experience forces from the stretching membrane during actuation, a compromise was required between flexibility and mechanical integrity of the interconnects when determining the thickness of the parylene layers in the mechanical design stage.

TiN has been commonly used as the preferred electrode material for cellular measurements, due to its chemical and mechanical stability and favorable electrochemical properties [82]. Moreover, TiN is suitable for microfabrication in terms of deposition and patterning. TiN is sputter deposited and patterned by dry

etching in chlorine plasma. Parylene is a biocompatible polymer which is deposited from vapor phase at room temperature. The advantages of parylene for microfabrication are its conformal deposition and negligible residual stress in the deposited layers owing to the deposition at room temperature. Residual stress in the electrical insulation layer can cause undesired out of plane buckling of the interconnect stack after membrane release, resulting in loss of membrane flatness. Unwanted curvature in the membrane can cause inhomogeneous distribution of the cells after seeding during cellular experiments. By using parylene completely flat SMEA membranes were obtained.

3.3.1   First layer parylene deposition and patterning (step 4)

The fabrication of the interconnect stack starts by deposition of the first layer of parylene. To improve the adhesion of parylene to the underlying silicon oxide, an organosilane adhesion promoter, AP3000, is used. AP3000 is a ~1% dilution of vinyltriacetoxysilane in an organic solvent, which is spin coated on the wafers prior to parylene deposition. Parylene is deposited at room temperature in a vacuum chamber from the pyrolised parylene monomer gas. In the deposition chamber the wafers are supported by several pins on the backside, therefore, parylene is deposited on both sides of the wafers. The unwanted parylene deposited on the backside is removed in oxygen plasma in a dry etching machine, while the wafers are positioned top side down on the chuck. Subsequently, the parylene is patterned in step 4 of the microfabrication to make openings for the electrodes and vias to the Al interconnects as shown in figure 3.7.
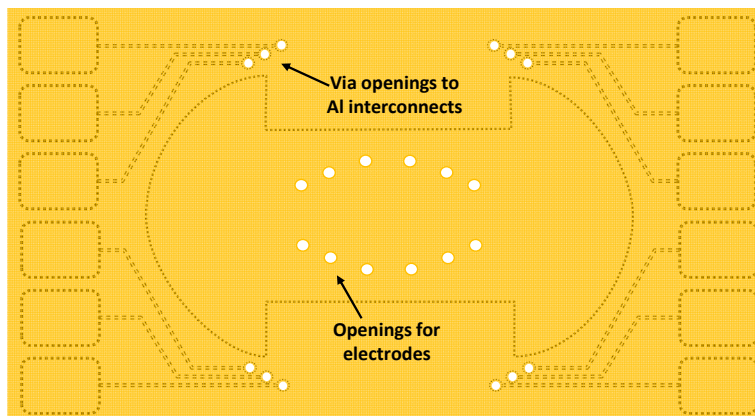
Figure 3.7 The schematic mask layout (shown in yellow) for the openings in the first layer of parylene for the electrodes and vias to the Al interconnects.

The parylene is patterned in oxygen plasma by using a photo resist mask. Since, both parylene and photo resist are etched in oxygen plasma, the mask is eroded during etching. Therefore, the etching recipe was optimized to achieve more anisotropic etching, resulting in less lateral erosion of the resist mask. Dry etching was performed in an Inductively Coupled Plasma (ICP) reactor in which the coil power and the plate power can be selected independently, to adjust the plasma density and the speed and directionality of the impinging ions on the surface, respectively. By using higher plate power more anisotropic etching was obtained.

For the resist mask a high resolution thick photo resist from MicroChemicals (AZ9260) was used. The thickness of the photoresist mask was chosen to be double the thickness of the parylene layer to compensate for the thickness loss during dry etching. Since the photo resist mask is relatively thick and also prone to erosion during dry etching, in order to obtain optimum fidelity in pattern transfer from the resist mask to the underlying parylene, the optimal stepper exposure parameters were determined. This was done by performing lithography with a Focus Exposure dose Matrix (FEM) followed by dry etching on a test wafer provided with the same thickness of parylene, and subsequent microscopy inspection.

3.3.2   TiN deposition and patterning (step 5)

TiN is sputter deposited on the patterned first-layer parylene. To improve the adhesion between TiN and parylene, an in situ argon plasma sputter etch is performed prior to the TiN deposition to introduce roughness to the parylene surface. Without the prior sputter etch, blisters form in the TiN layer during lithography due to compressive residual stress and consequent delamination [92].

After TiN deposition, cracks form in the TiN layer inside the parylene openings for the vias, however, for the electrode openings the TiN layer remains intact (figure 3.8). The parylene openings for the vias lie on aluminum and for the electrodes on oxide, as depicted in the process cross-section of step 4. The cracks inside the via openings are caused by the poor adhesion between parylene and Al, which allows the side walls of the parylene opening to move as a result of thermal expansion during TiN deposition and subsequent cooling. The retraction of the side walls of the parylene opening after TiN deposition introduces gaps between the TiN layer deposited on the side walls and the layer deposited at the bottom of the via on Al, as illustrated in figure 3.9 (left). For the electrode openings however, sufficient

adhesion between parylene and oxide - in the presence of the silane adhesion promoter - prevents the movement of the parylene layer and formation of cracks.
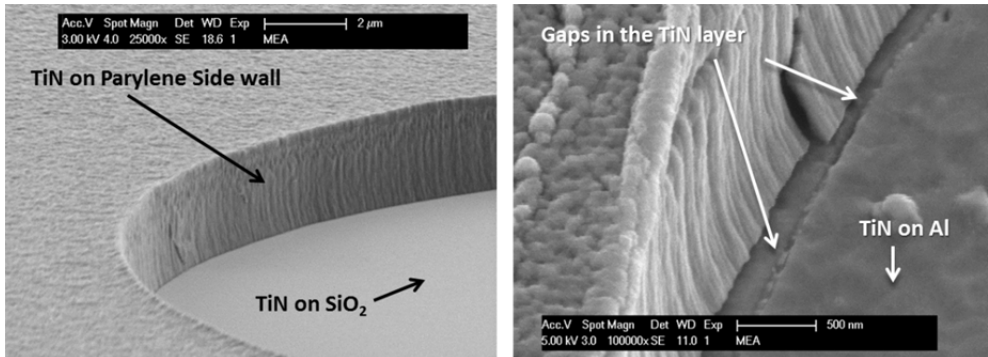
Figure 3.8 SEM micrograph showing the coverage of the 100nm thick TiN layer deposited on the parylene openings (left) on top of silicon oxide for an electrode, and (right) on top of aluminum for a via, respectively. As shown in the right image, due to poor adhesion of parylene to the underlying Al, the sidewall of the opening in the parylene layer can retract as a result of cooling after TiN deposition, causing gaps to form in the deposited TiN layer. However, for the electrode opening shown on the left image, good adhesion of parylene on oxide in the presence of the silane adhesion promoter prevents parylene movement due to thermal expansion and subsequent cooling, keeping the deposited TiN layer intact.

To ensure electrical conductivity in the vias a 100 nm thick layer of Al was deposited and patterned to form "Al plugs" covering the gaps as shown in figure 3.9.

Figure 3.9 (left) Schematic representation of the gaps formed in the TiN layer inside the vias, caused by parylene sidewall retraction as a result of cooling after TiN deposition. (right) Covering the gaps by depositing and patterning a layer of aluminum to from an "Al plug" inside the vias.

In order to prevent the formation of electrical discontinuities inside the vias, two possible solutions are proposed. One solution involves modifying the location of the parylene openings for the vias in the mask design, such that the parylene opening is located partially on the oxide adjacent to the Al interconnects, as

demonstrated in figure 3.10 (right). In this manner as mentioned before the proper adhesion of parylene to oxide prevents the formation of gaps in the TiN layer, and the electrical connection between TiN interconnects and Al interconnects is maintained. The second solution requires depositing an additional layer of oxide on top of the Al interconnects and subsequent opening of the layer at the via locations prior to parylene deposition, as shown in figure 3.10 (left).
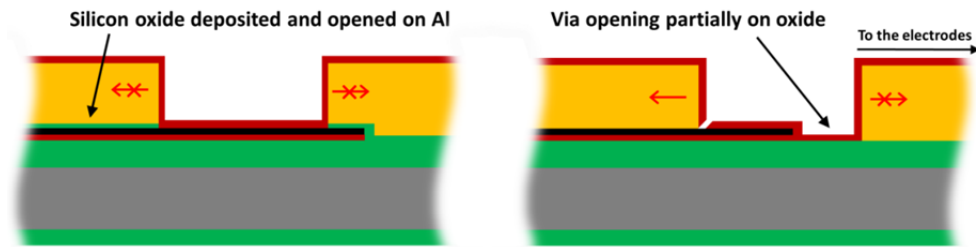
Figure 3.10 Schematic diagram depicting the two possible solutions to prevent electrical discontinuity in the TiN layer inside the vias. (left) A layer of silicon oxide is deposited on the front side wafers on top of the Al interconnects, and opened at the location of vias. The oxide layer provides proper adhesion to subsequently deposited parylene layer preventing the retraction of parylene side walls after TiN deposition. (right) In the mask design the location of the via openings in the parylene is slightly altered to partially position the opening on the oxide adjacent to the Al interconnects. In both solutions the proper adhesion of parylene to oxide in the presence of silane primer prevents the movement of parylene due to thermal expansion during TiN deposition, and subsequent retraction.

The deposited TiN layer is patterned in step 5 of the microfabrication, to define the electrodes and TiN interconnects on the membrane area, by dry etching TiN in a chlorine plasma using a resist mask. The TiN interconnects are the finest features fabricated in the SMEA chips, having widths of 1-2 μm or narrower if required. To pattern these small features, SPR660, a thin photo resist suitable for fine lithography, is used in this lithographic step. Since the resist is spin coated down to 0.8 μm in thickness, to prevent the formation of comets during spin coating, the sizes of the openings in the first 2 μm thick parylene layer should be kept as small as possible.

Generally, after dry etching, a thin superficial layer of the photo resist mask can become undissolvable in acetone, due to heavy cross-linking activated under deep-UV radiation. Resist ashing at elevated temperatures in oxygen plasma cannot be used to remove the resist mask at this stage, to prevent thermal damage to parylene. Therefore, the superficial cross-linked resist layer was first removed by applying a

short low-temperature oxygen plasma descum, and subsequently the remaining resist was acetone stripped.
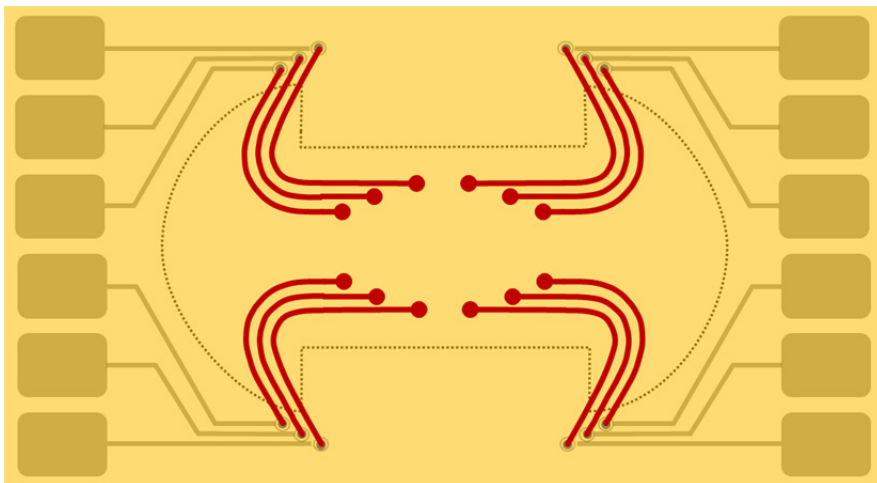
Figure 3.11 The schematic mask layout (shown in red) for patterning the TiN for electrodes and flexible interconnects.

3.3.3   Second layer parylene deposition and patterning (step 6)

In step 6 of the microfabrication, the second layer of parylene, 2 µm in thickness is deposited to fully insulate the interconnects. As mentioned previously, after parylene deposition the unwanted parylene deposited on the backside of the wafers is dry etched in an oxygen plasma. To improve the adhesion of the second layer parylene to the underlying TiN structures, an in situ vapor priming with a silane adhesion promoter, A174 (3-Methacryloxypropyltrimethoxysilane), is performed. Without the silane adhesion promoter, the adhesion of parylene to underlying TiN structures is poor, resulting in delamination of the electrodes after membrane release in step 13 of the microfabrication, as illustrated in figure 3.12. The delamination process is also mediated by the release of the residual stress in the TiN layer after removal of the underlying oxide, in case of insufficient parylene/TiN interlayer adhesion.

The first and second parylene layers are patterned together in step 6 of the microfabrication, to form the electrical insulation of the interconnects and electrodes, by using a resist mask and anisotropic dry etching in an oxygen plasma as described previously for the first parylene layer.
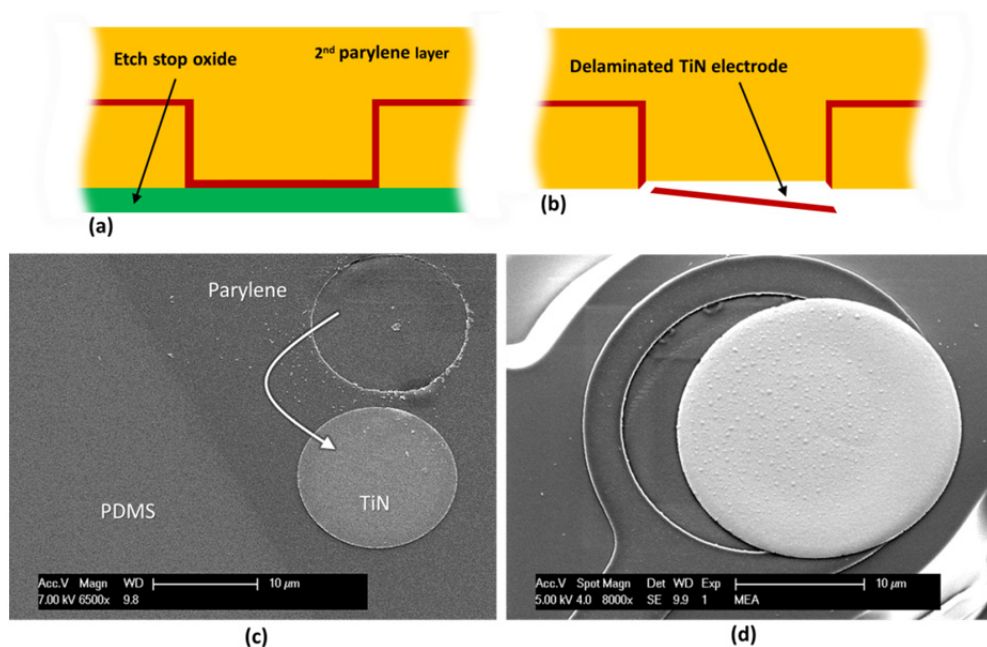
Figure 3.12 Lack of sufficient adhesion between the second layer parylene and the TiN layer results in delamination of the electrodes after membrane release. (a) Cross-sectional view of an electrode before removal of the oxide etch stop layer. (b) Delamination of the electrode after oxide removal, mediated by the residual stress in the TiN layer. (c, d) SEM micrographs of dogbone and circular chips showing delaminated TiN electrodes.
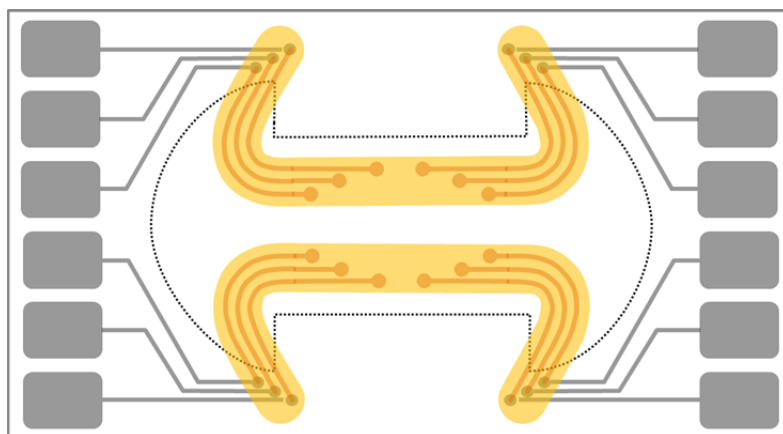
Figure 3.13 The schematic mask layout (shown in yellow) for the patterning of the first and second parylene layers.

3.4 Fabricating the photoresist sacrificial mold (step 7)

The surface micro-features in the membrane are fabricated by using sacrificial photo resist molds. The resist mold is eventually dissolved in acetone after release of the membrane in the last step of processing. In step 7 of the microfabrication, a layer of AZ9260 high resolution photo resist is spin coated to reach the desired height for the micro-features - in the case of the previously shown devices 12 μm thick - and patterned to define the inverse mold for the micro-features (figure 3.14).
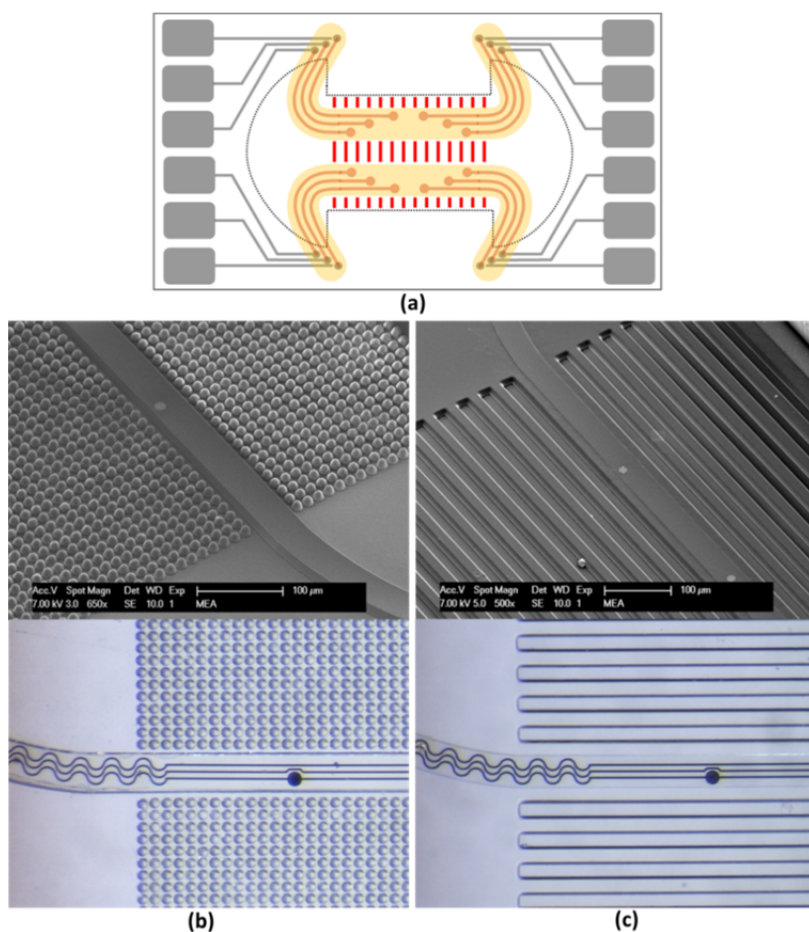
Figure 3.14 (a) The schematic mask layout (shown in red) for the fabrication of the resist mold for transversal micro-grooves. The photo-resist can generally be patterned to define diverse types of micro-features, for instance micro-pillar, micro-spheres, micro-grooves, etc. Two examples are shown in SEM and optical micrographs of SMEA membranes in images (b and c). The micro-spheres in the left image were obtained by an exposure-dose and focus that partially exposes holes in the sacrificial resist layer.

In case features with submicron heights are required on the SMEA membranes, using photo-resist molds is not a suitable approach. Since, already existing structures on the wafer having several microns of height would cause comets during spin coating of very thin layers of photo resist. An alternative approach for the fabrication of submicron features is to etch the required mold in the etch stop oxide layer, as demonstrated in figure 3.15. It is also possible to combine the two molding methods in a single device to realize more complex micro-features, as illustrated in figure 3.16.
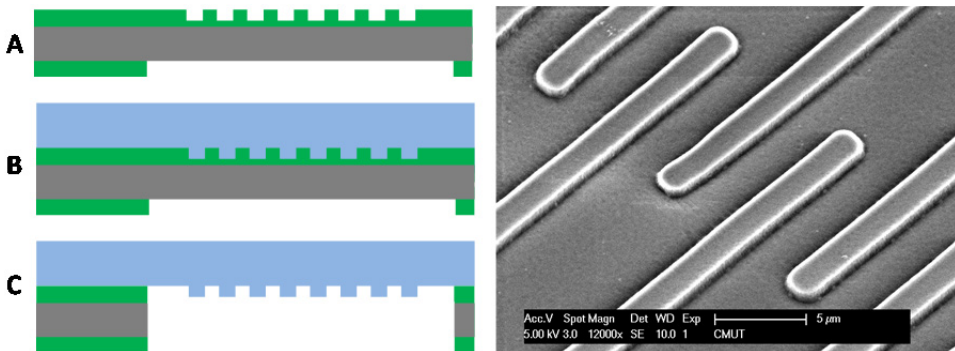
Figure 3.15 (left) Schematic diagram depicting the fabrication of submicron features in the PDMS membrane. The mold for the features is dry etched in the etch stop oxide before applying PDMS. The membrane is released by deep etching of silicon and subsequent wet etching of oxide. (right) SEM micrograph of a PDMS membrane with features 1 µm in height.
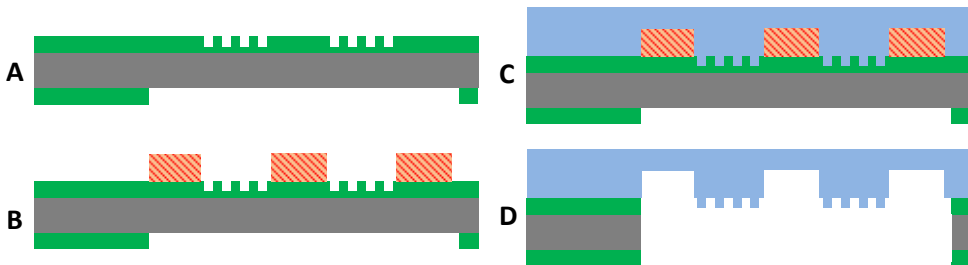
Figure 3.16 Schematic diagram depicting the process steps for the fabrication of complex features in the PDMS membrane by combining two molding methods. The submicron features are first etched in the oxide etch stop layer. Subsequently resist is spin coated and patterned to define the larger features. The oxide and sacrificial resist are removed after deep etching of underlying silicon.

3.5   PDMS processing (steps 8-10)

In step 8 of the microfabrication a 20 μm thick layer of PDMS (Dow Corning, Sylgard 186) with standard 10:1 base to curing agent mixing ratio is spin coated on the wafers and cured in a convection oven at 90 °C for 30 minutes. To improve the adhesion of PDMS to the parylene insulation of the interconnect stack AP3000 silane primer can be applied before spin coating the PDMS. However, at this stage to prevent damage to the already existing resist structures by the organic solvent of the primer, either the primer should be applied from vapor phase or a water based solution of the silane agent should be used.

Subsequently, a 150 nm thick layer of aluminum layer is sputter deposited on the PDMS at very low power to reduce the thermal budget. This aluminum layer serves two purposes. It acts as an anti-stiction layer between PDMS and the chuck of the DRIE etcher during deep etching of silicon from the backside in step 11 of the microfabrication. The aluminum layer also serves as the hard etch mask for dry etching of the PDMS to provide access to the underlying aluminum contact pads (figure 3.17 (b)). Although a thinner, e.g. 50 nm thick, layer of aluminum would be sufficient for the mentioned purposes, the thickness of the aluminum layer was increased to prevent resist cracking during subsequent lithography.

The aluminum layer deposited on PDMS forms ordered wrinkle patterns as shown in figure 3.17a. One possible reason for the emergence of the wrinkles is the release of the residual compressive stress developed in the deposited aluminum layer after cooling as a result of thermal mismatch between the aluminum and the PDMS [93], [94]. The other possible explanation for the observed wrinkles is the in situ formation of wrinkles on the PDMS surface due to heating in the deposition chamber, and concurrent deposition of Al on top of the emerged wrinkles [95], [96].

The presence of the wrinkles in the aluminum layer can cause complications for the subsequent lithography on the aluminum layer. Generally, the photoresist layer develops a tensile stress due to cooling after soft bake. In case the resist is spin coated on a compliant substrate, this stress might be released by the formation of cracks in the resist layer. Since, the wrinkles make the aluminum layer on the PDMS compliant to a certain degree, cracks can appear in the resist layer by deforming and straightening the wrinkles in the underlying aluminum layer at the bottom of the cracks' cleavage as observed microscopically. Therefore, to prevent

resist cracking, the thickness of the Al layer was increased to 150 nm to reduce its compliancy to an acceptable level, and additionally, a thinner resist layer was applied to reduce the cleaving force generated by the residual tensile stress in the resist layer.
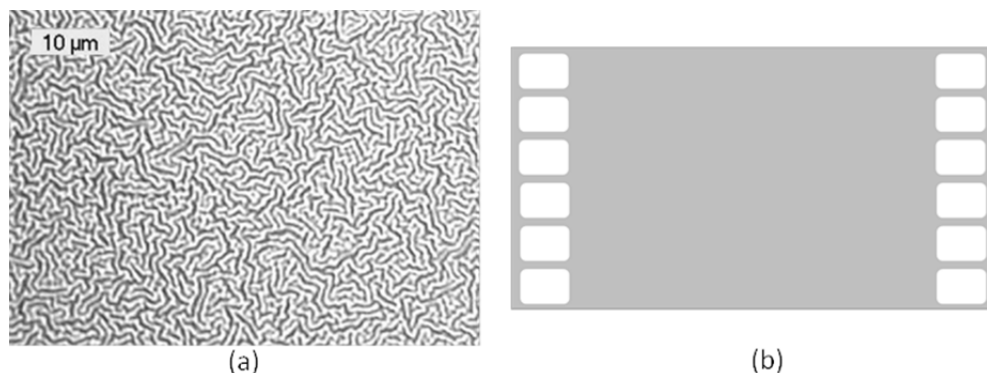
Figure 3.17 (a) An optical micrograph showing the ordered wrinkles observed after aluminum sputter deposition on PDMS. (b) Schematic mask layout for patterning the Al hard etch mask to open PDMS layer to access the contact pads.

After patterning the Al mask, the PDMS is dry etched in an SF_6/CF_4 plasma. The fluorine chemistry of the plasma does not etch aluminum, therefore the etching automatically stops on the underlying aluminum contact pads. Dry etching of PDMS with the mentioned chemistry produces fibrillar remnants - possibly with compounds similar to teflon - at the end of the etching process, which are chemically very stable and cannot be removed by chemical means [97], [98]. However, these remnants are loosely attached to the underlying aluminum surface and can be effectively removed by rinsing the wafers using a mild water jet to mechanically dislodge and wash them away. Figure 3.18 shows SEM micrographs depicting an Al bond pad with the remnants present and after their removal.

3.6 Silicon deep etch and release of the membrane (steps 11-14)

The silicon substrate underneath the membrane area is removed by DRIE etching of silicon from the backside in step 11 of the microfabrication. The etching stops on the etch stop oxide layer provided on the front side of the wafers. After deep etching the polymer layer deposited on the side walls of the cavities during the DRIE process is removed by using an in situ oxygen plasma, in order to improve

the hydrophilicity of the side walls for subsequent wet etching of the etch stop layer. Subsequently, the aluminum hard etch mask on the front side PDMS is wet etched in phosphoric/acetic acid aluminum enchant.
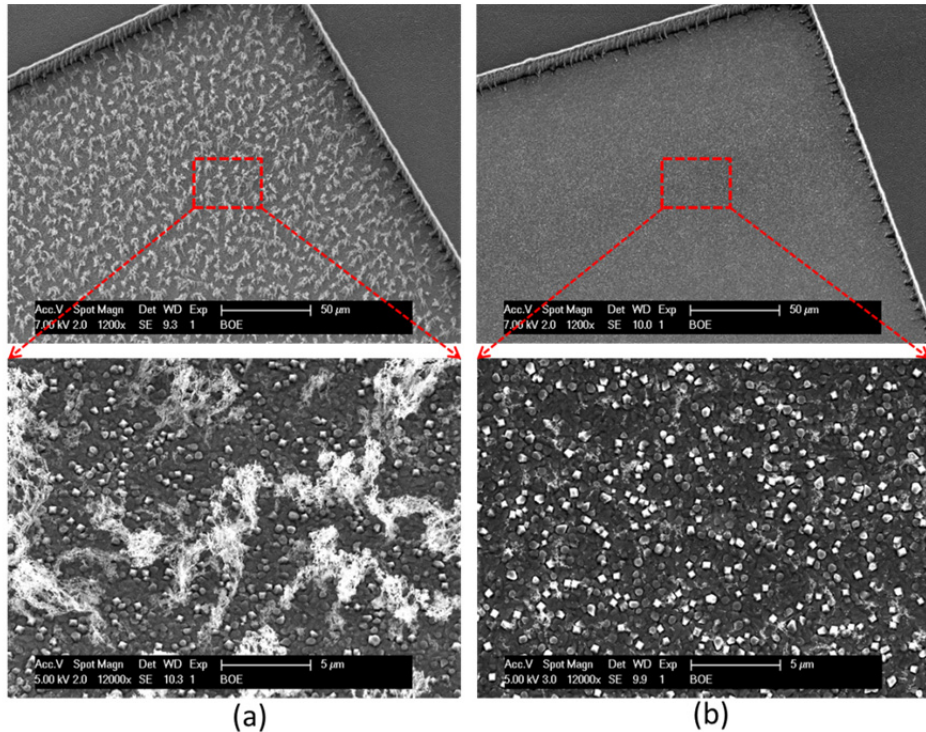
Figure 3.18 SEM micrographs of the aluminum bond pads exposed after dry etching the PDMS layer, showing (a) fibrillar remnants lying on the aluminum surface, and (b) a clean bond pad after rinsing the wafer with a mild water jet.

At this stage the membranes are completely flat as a result of using low stress PECVD oxide instead of thermal oxide for the etch stop oxide layer, as described previously. However, during the wet etching of the oxide layer, the thickness of the layer is gradually decreased to a critical point where the residual stress in the oxide is enough to buckle the layer. As a consequence of the buckling, cracks appear in oxide layer which damage the interconnect stack lying on top, as shown in figure 3.19.

To prevent the buckling of the oxide during wet etching, a thick photo resist layer is spray coated on top of the PDMS as a mechanical support layer before wet etching the oxide, as illustrated in step 12 process cross-section in table 3.1. Afterwards the oxide/Ti/oxide stack is wet etched in buffered hydrofluoric acid.
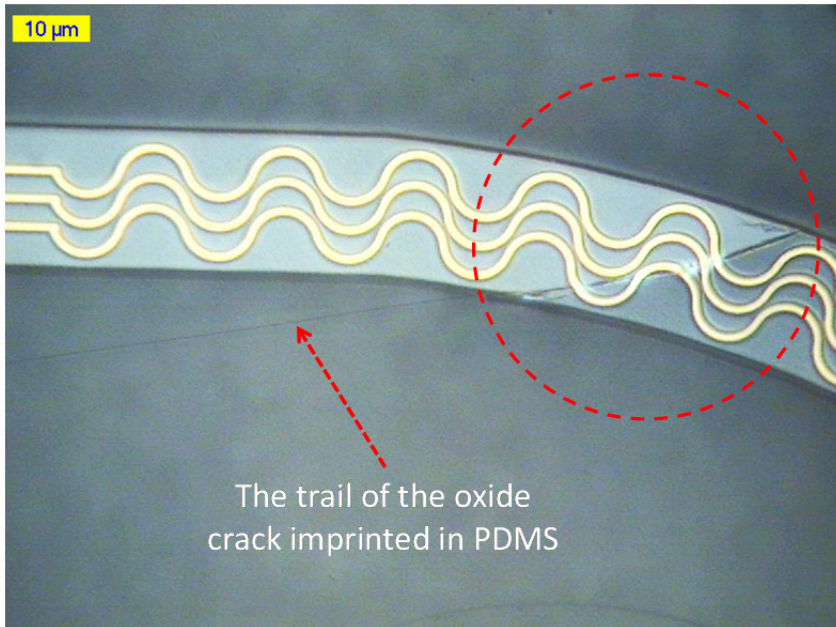
Figure 3.19 An optical micrograph of the membrane surface after removal of the etch stop oxide, illustrating the formation of cracks in the interconnect stack as a result of oxide layer cracking during wet etching in the absence of the mechanical support layer.

The final step to fully release the SMEA membranes is dissolving the resist mechanical support layer on the front side and the resist micro-molds in the membranes' surface in acetone. Figure 3.20 shows a SEM micrograph of a fully fabricated SMEA membrane stretched inside the SEM chamber by a small length of wire placed underneath the membrane for demonstration.

3.7   Mechanically isolated interconnects

Based on the same technology platform it is possible to fabricated interconnects which are mechanically isolated from the membrane, to isolate the forces exerted by the membrane and allow the interconnects to bend out of plane to improve their stretchability without delamination form the membrane. This can be accomplished by properly patterning the sacrificial resist around or on top of the interconnect tracks before application of the elastomer, as demonstrated schematically in Figure 3.21.
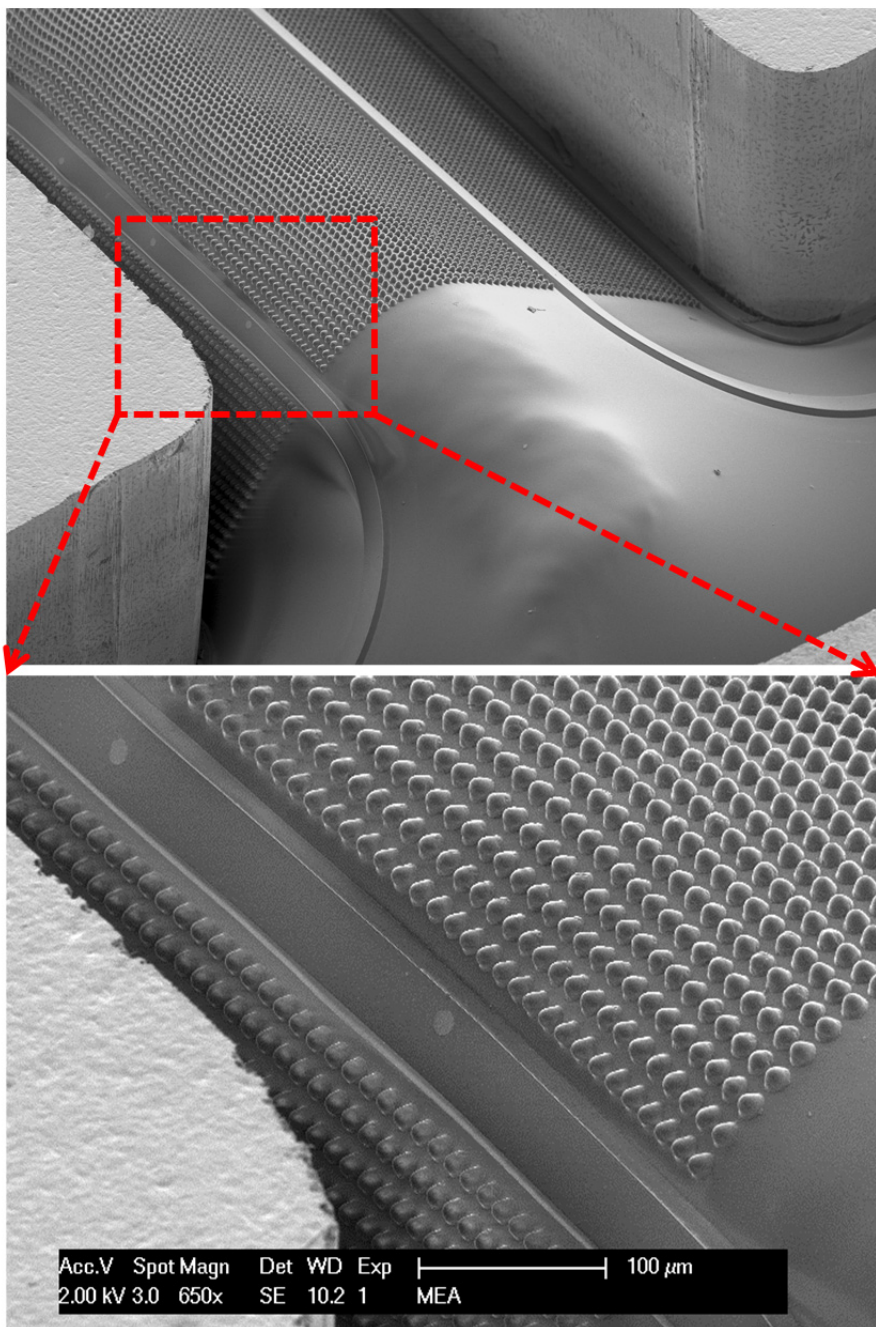
Figure 3.20 A SEM micrograph of a SMEA membrane stretched inside the SEM chamber by a small piece of wire placed underneath the membrane.
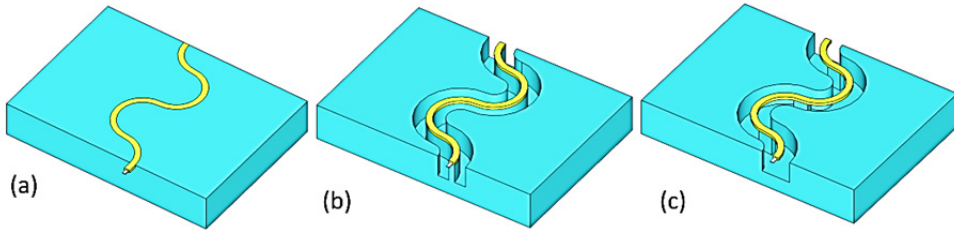
Figure 3.21 (a) An interconnect track normally embedded in the surface of a membrane. The track is prone to delamination from the membrane when the membrane is stretched. (b) A mechanically isolated interconnect track which is immune to delamination, as also shown in Figure 3.20. The sacrificial resist is patterned around the track. (c) An interconnect supported by only pillars, enabling improved bendability compared to image (b). Pillars are formed by properly patterning the sacrificial resist on top of the interconnect track.

3.8   Summary

The microfabrication of the SMEA chips using the elastomer last approach was discussed and demonstrated in this chapter. The microfabrication process avoids the problems associated with thin film processing on top of elastomers, by fabricating the micro-structures on a silicon wafer by using standard micro-fabrication techniques and subsequently transferring the structures to the applied elastomeric layer by removal of the underlying silicon substrate.

The presented microfabrication process can be used as a generic fabrication platform to embed electrodes and interconnects in a stretchable membrane along with diverse types of surface micro-features, in a manufacturable manner. Moreover, since the microfabrication is based on silicon processing and is CMOS compatible, it in principle enables the integration of silicon sensors and active electronics for on-chip sensing, amplification and digitization.

Chapter 4 - Electro-chemical and electro-mechanical characterization

This chapter presents the characterization tests performed on the SMEA devices and the obtained results. The chapter is divided into two main sections. The first section discusses the electrochemical characterization, with the focus on obtaining the electrochemical impedance characteristics of the electrodes. The second section presents the elecromechanical characterization of the devices with the purpose of determining the resistance change of the interconnects due to pneumatic actuation.

4.1   Electrochemical characterization

The charge transfer at the electrode-electrolyte interface occurs via either capacitive or faradaic mechanisms, depending on the type of material used for the electrode. In the capacitive mechanism the charging and discharging of the electrode-electrolyte double layer capacitance transfers the charge. In the faradaic mechanism to transfer charge a chemical reaction has to happen at the electrode-electrolyte interface, in which surface-confined species are oxidized or reduced [82].

The material selected for the electrodes in the SMEAs, titanium nitride (TiN), is a chemically stable conductor for which charge transfer happens mainly through the double layer capacitance [82]. Recording electrodes are typically characterized by their impedance at 1 kHz with values ranging from 50 kΩ to 1 MΩ depending on the size and material of the electrodes [82], [99]. A common method to determine the impedance of the electrodes is Electrochemical Impedance Spectroscopy (EIS) in which the magnitude and phase of the electrode impedance is determined over a broad frequency range, typically <1 Hz to >10^5 Hz, by exciting the electrodes with a precisely controlled sinusoidal small signal voltage and measuring the current, or vice versa.

In the following sections first the electrode-electrolyte double layer capacitance is briefly explained theoretically and the parameters affecting its value are identified. This is followed by experimental EIS measurements and a discussion of the

underlying measurement challenges, particularly for the SMEA device, and finally the obtained results are presented.

4.1.1   Double layer capacitance

When the surface of an object is exposed to an electrolyte, an electrical double layer of ions forms on the surface. The first layer, the surface charge, consists of adsorbed hydrated ions on the surface of the electrode (either positive or negative) and the second layer, the diffuse layer, is composed of hydrated ions attracted by the aforementioned surface charges, which electrically shields the first layer [100], [101]. This electrical double layer together with the electrode conductor form a capacitance which determines the electrochemical impedance of the electrode. Several models have been proposed to determine the value of this capacitor (Figure 4.1). The earliest model is the Helmholtz model in which all the counter ions are assumed to be adsorbed at the electrode surface (Figure 4.1 (a)). This structure is similar to a dielectric capacitor whose plates are separated by a distance H, approximately equal to the radius of the solvated counter ions. Therefore, the capacitance per unit surface area (the specific capacitance) of the Helmholtz double layer, C_s^H, is given by the equation below in F/m^2:

$$C_s^H = \frac{\epsilon_0 \epsilon_r}{H} \tag{4.1}$$

where ϵ_0 and ϵ_r are the free space and the relative permittivity of the electrolyte, respectively.

The second model is the Gouy-Chapman model which takes into account the fact that the ions in the electrolyte are mobile and driven by the coupled forces of diffusion and electric field [101], resulting in a diffusion layer as shown in Figure 4.1.b. The specific capacitance of the diffuse layer, C_s^D, for a simple electrolyte containing only two types of ions with the same opposite charge and the same concentration (i.e. a binary symmetric electrolyte) can be approximated by:

$$C_s^D = \frac{\epsilon_0 \epsilon_r}{\lambda_D} \tag{4.2}$$
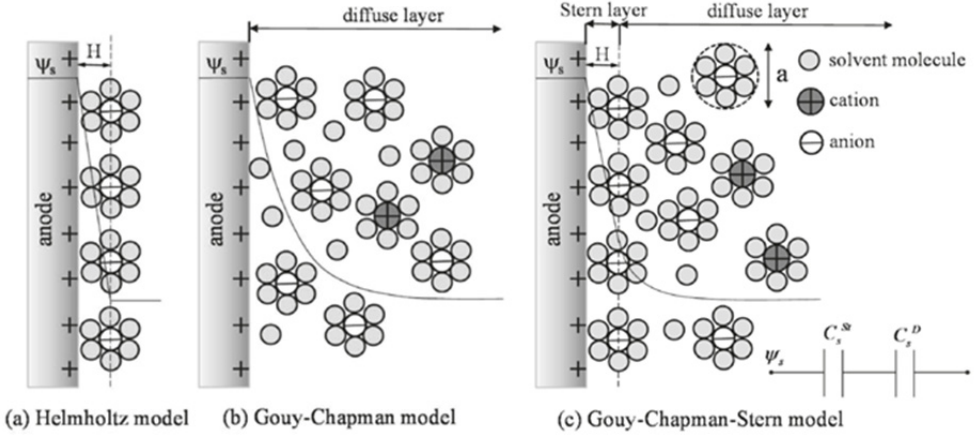
Figure 4.1 Schematic representation of (a) Helmholtz, (b) Gouy-Chapman (c) Gouy-Chapman-Stern models for the electric double layer capacitance. Adopted from [101].

where λ_D is the Debye length, which is a measure of how far from the electrode this double layer extends. The Debye length - and therefore the diffuse layer capacitance - is dependent on the electrolyte concentration c, the charge of the ions z, the temperature T, and the relative permittivity of the electrolyte, and is given by $\lambda_D = (\epsilon_0 \epsilon_r k_B / 2e^2 z^2 N_A c)^{1/2}$ where k_B, N_A and e are Boltzmann constant, Avogadro's number and the elementary charge respectively. It should be noted that the approximation in equation (4.2) is true for small electrode potentials (in the order of mV), otherwise the diffuse layer capacitance is dependent on and increases with the electrode potential [101].

To have a more accurate model, the Gouy-Chapman-Stern model was developed which takes into account both the adsorbed immobile charges on the electrode surface, and the diffuse layer charges, as shown in Figure 4.1.c. Therefore, according to this model the total double layer specific capacitance (F/m^2) is equivalent to the Helmholtz capacitance C_s^H in series with the diffuse layer capacitance C_s^D:

$$C_s^{Total} = \frac{C_s^H C_s^D}{C_s^H + C_s^D} \tag{4.3}$$

Assuming the electrolyte is a NaCl solution - similar to the Phosphate buffered Saline (PBS) which was used in the EIS experiments and constitutes the major component of cell culture solutions - with $\epsilon_r = 78$, $c = 137$ mmol/L and

$H = 0.33$ nm at room temperature, the values of the series capacitances can be calculated as: $C_s^H = 2.1$ F/m^2 and $C_s^D = 0.83$ F/m^2, resulting in $C_s^{Total} = 0.6$ F/m^2.

The value that was measured for the electrode capacitance with EIS - presented in the next section - is 35 pF for a circular electrode 12 µm in diameter, corresponding to specific capacitance of 0.31 F/m^2. The value predicted by the Gouy-Chapman-Stern model for the capacitance is therefore larger than the measured value. This difference can be attributed to several physical factors that are not included in the theoretical models. First of all the decrease of relative permittivity at increased ionic concentrations near the electrode surface, compared to that of the bulk electrolyte can reduce the theoretically predicted capacitances [101], [102]. Secondly, in reality the thickness of the Helmholtz (Stern) layer maybe larger than the solvated ions radius due to the adsorption of solvent molecules and ions near the electrode surface, which can further reduce the value for the calculated capacitance [101]. And finally, the difference might arise from the fact that the electrolyte used in the EIS experiments - PBS - is similar to, but not exactly the same as the one assumed for the model and contains other components besides NaCl.

4.1.2   Electrochemical Impedance Spectroscopy (EIS)

Electrochemical Impedance Spectroscopy (EIS) is a method to determine the impedance characteristics of an electrochemical cell or simply an electrode immersed in an electrolyte. In this method a controlled ac voltage (current) with a certain frequency and amplitude is applied across the electrochemical cell or the electrode/electrolyte interface, and the passing current (voltage) is measured and recorded. By having the magnitude and phase of the measured current, and the applied voltage, the magnitude and phase of the electrode's impedance can be determined for each frequency point according to Ohm's law. By repeating the measurement for different frequencies, the spectrum of the impedance magnitude and phase can be determined over a broad frequency range. Afterwards, if needed, a circuit model can be fitted to the measured impedance spectrum [103].

4.1.2.1   Three-electrode measurement

The EIS measurement to determine the electrochemical impedance of an electrode can be performed using a two or three-electrode configuration. In the two-electrode

method (Figure 4.2.a), a counter electrode, CE, is immersed in the electrolyte and the excitation voltage is applied between the counter electrode and the electrode whose impedance is to be measured (the working electrode WE). The problem with the two-electrode measurement is that there will be a voltage drop across the counter electrode double layer impedance, Z_{CE}. Consequently, the exact voltage across the working electrode double layer impedance, Z_{WE}, cannot be determined. As a result with this method the total impedance of the working and counter electrodes is measured. This method therefore only works if Z_{CE} is much smaller than Z_{WE} for all frequencies.
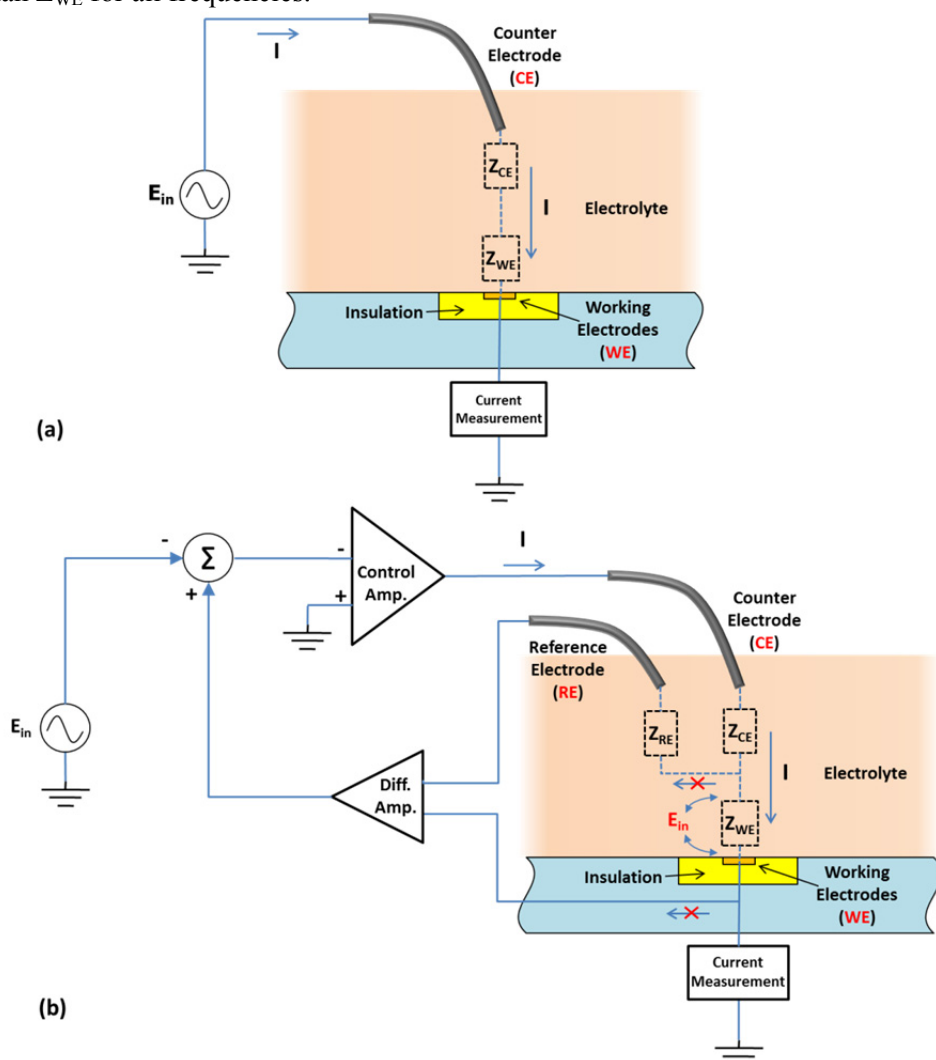
Figure 4.2 (a) Two-electrode and (b) Three electrode measurement set-up.

In order to circumvent the above mentioned limitation and to be able to apply an exact voltage across the WE impedance, Z_{WE}, a third electrode is required (Figure 4.2b). This electrode, which is called the reference electrode, RE, does not carry any current and therefore no ac voltage drop occurs across its double layer impedance. The reference electrode is therefore measuring the exact potential of the electrolyte in the vicinity of the working electrode. By measuring the voltage difference across Z_{WE} and comparing it with the desired excitation voltage E_{in} in a feedback loop, the current through the counter electrode can be adjusted such that the exact desired voltage E_{in} appears across the working electrode impedance. Since no current is drawn by the differential amplifier inputs as shown in Figure 4.2b, all the measured current, I, is passing through the WE. As a result, with this method the exact impedance of the WE can be determined.

4.1.3 Measurement results

The electrochemical impedance of the TiN micro-electrodes was determined with standard Electrochemical Impedance Spectroscopy (EIS) method in a 3-electrode arrangement by using a Metrohm Autolab instrument with a PGSTAT12 module by applying a sinusoidal excitation voltage with 20 mV amplitude in the frequency range 100 Hz to 600 kHz across the electrode-electrolyte double layer. For the electrolyte, Phosphate Buffered Saline (PBS), which is the major component of cell culture solutions, was used.

Each electrode is electrically contacted through aluminum contact pads fabricated at the periphery of the chips. The aluminum contact pads are fabricated on a 2µm thick silicon oxide layer, which due to their relatively large size ($1.5 \times 0.9 mm^2$) have a noticeable parasitic capacitance (~ 36 pF) between each contact pad and the silicon substrate. Since the silicon substrate is a semiconductor and not an insulator, this parasitic capacitance forms a parasitic path for the applied current when the electrolyte is in contact with the silicon substrate, as shown in Figure 4.3a. To eliminate the effect of this parasitic capacitance the EIS measurements were carried out in a droplet of electrolyte dispensed on the micro-electrodes, consequently avoiding any contact between electrolyte and the silicon substrate (Figure 4.3b). EIS measurements were performed by immersing two platinum wires (each 100 µm in diameter) as the reference and counter electrodes in the PBS droplet under a stereo microscope by using micromanipulators.
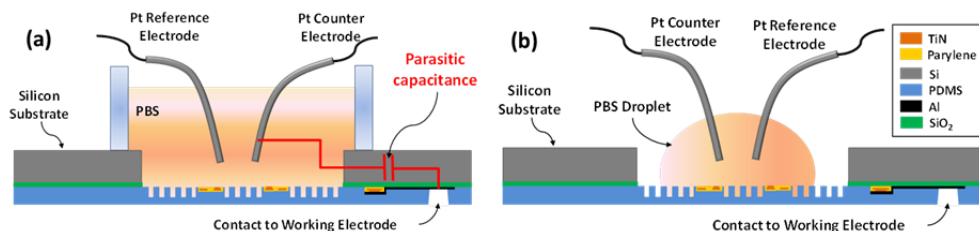
Figure 4.3 Schematic cross-section view of the chips and the measurement electrodes showing (a) the parasitic capacitance when the silicon substrate is in contact with the electrolyte, and (b) a measurement in an electrolyte droplet dispensed on the micro-electrodes to avoid contact between the silicon substrate and the electrolyte.

Due to the small size of the electrodes (each 12 μm in diameter), each micro-electrode exhibits a relatively high impedance in the low frequency range of the measurement, which results in currents lower than the measurement capability of the measurement instrument. Since the excitation voltage should remain small in order to perform measurements in the linear regime several electrodes were measured in parallel to increase the measured current. Figure 4.4 shows the impedance magnitude and phase of 5 electrodes measured in parallel averaged over 4 consecutive measurements. Recording electrodes are usually characterized by their impedance at 1 kHz; since the electrodes are identical, the characteristic impedance of one electrode is derived from the measurements to be ~4.5 MΩ at 1 kHz. At this frequency the resistance of the interconnects (< 47 kΩ) is negligible compared to the electrodes impedance.
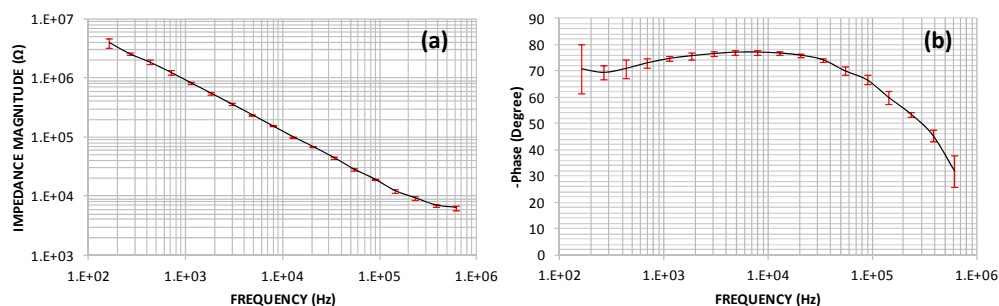
Figure 4.4 The magnitude (a) and phase (b) of the double layer impedance of 5 TiN micro-electrodes measured in parallel (#of measurements = 4). The magnitude of impedance at 1 kHz for the 5 electrodes is ~ 0.9 MΩ, corresponding to ~4.5 MΩ for each electrode [104].

The parasitic capacitance between each interconnect line and the electrolyte, through the 2 μm thick parylene insulation was also measured by dispensing a droplet of the electrolyte on the interconnect bundles and immersing a Pt electrodes

in the droplet and measuring the impedance between the Pt electrode and contact pads with an RLC meter (in this measurement the contact pads where short circuited to eliminate the effect of parasitic capacitances through the substrate). Since the double layer capacitance of the immersed Pt electrode is orders of magnitude larger than the parasitic capacitance of the interconnects, the measured value indicates the parasitic capacitance. The measured parasitic capacitance of each interconnect line was ~1.3 pF/mm.

4.2   Electromechanical characterization

For electromechanical characterization, the chips were mounted in the electro-pneumatic holder - as described before - and a controlled pneumatic pressure was applied to the backside of the membrane while continuously measuring and logging the electrical resistance change of the interconnect tracks in the membrane, and the applied pressure by using a National Instruments USB-6353 data acquisition system and a custom written Matlab program (Figure 4.5). In order to supress the mains 50 Hz interference and electromagnetic noise the resistance measurements were carried out differentially in a Wheatstone bridge configuration (Figure 4.5 (b)), and the differential voltage read out was subsequently converted to resistance change value by the Matlab script according to the resistance values of the bridge and the supply voltage:

$$\Delta R = \frac{V_{diff}\left(R_{ref} + R_{track}\right)}{\left(R_{ref}V_S - V_{diff}\left(R_{ref} + R_{track}\right)\right)} \qquad (4.4)$$

Normally, in order to increase the sensitivity of the bridge, the supply voltage of the bridge, V_S , can be increased. However, for voltages above approximately 5 V an positive drift in the resistance of the interconnects was observed over time - even without mechanical actuation - which can be attributed to current levels high enough to cause electromigration (2×10^7 A/cm^2) or thermally activated process in the TiN interconnects as describe in [105] as a result of the small cross sectional area of the interconnect tracks (2 μm×100 nm) and thermal isolation due to the parylene and the surrounding PDMS membrane. Therefore, for the experiments excitation voltages lower than 5V were mainly used. Another effect that was observed in the experiments was an increased level of noise in the presence of light, which can be caused by the photovoltaic effect in the silicon substrate. This

noise was effectively eliminated by covering the chips with an opaque plastic box during the measurements.
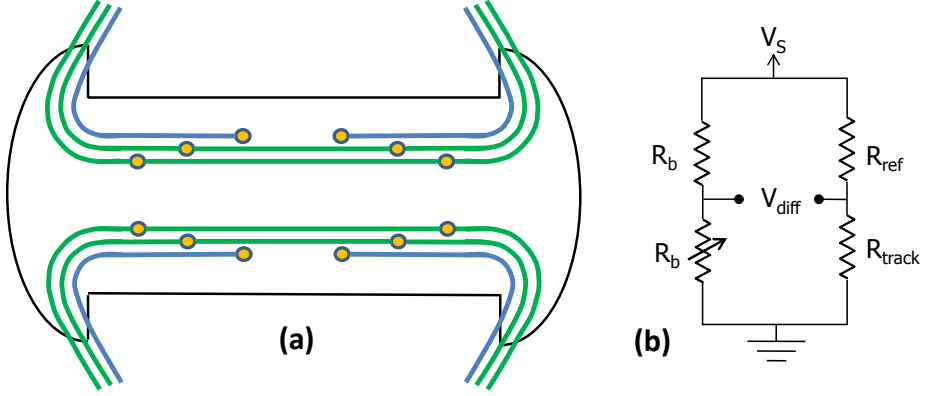
Figure 4.5 (a) Schematic layout of the interconnect tracks and the electrodes. The continuous tracks used in the measurements are denoted in green. (b) Wheatstone bridge configuration for measuring the change of the interconnects resistance, R_{track}, upon membrane inflation. The values of R_{ref} and R_b were selected to be close to the track resistance (~47 kΩ) to have maximum sensitivity for the bridge, and a trimmer resistor in the left leg of the bridge was used to balance the bridge to have zero V_{diff} in the beginning of measurements in the deflated state of the membrane.

Since the strains in the inflated membranes are large, the normal small strain bulge test equations cannot be used to relate the applied pressure and the strain in the membrane. Therefore the strain in the membrane was calculated geometrically from the measured vertical displacement of the center of the membrane as described in [61]. When the dogbone membrane is inflated the rectangular region in the middle of the membrane deforms to a semi-cylindrical shape. Figure 4.6 (a) shows the transversal cross-section of the membrane inflated to a semi-cylindrical shape with radius R. The radius R can be calculated from width of the membrane, $2w$, and the vertical deflection of its center:

$$R^2 = (R - z)^2 + w^2 \Rightarrow R = \frac{z^2 + w^2}{2z}$$
(4.5)

Subsequently, having R, the length of the membrane after inflation, l, is calculated:

$$l = 2R\theta = 2R \sin^{-1}\left(\frac{w}{R}\right) , \forall z \leq w$$
(4.6)

The strain, s, is then calculated as the change in the length of the membrane divided by its initial length, $2w$:

$$s = \frac{l - 2w}{2w} \qquad\qquad (4.7)$$

Figure 4.6 (b) shows the strain as calculated from Equations 4.5-4.7 with respect to the normalized vertical displacement of the center. This geometrical derivation of the strain is valid up to the point where the membrane's cross-section attains a semicircular shape ($\forall z \leq w$). The vertical displacement was measured optically by focusing on the center of the membrane by using an optical microscope table equipped with a vertical height measurement instrument. Figure 4.6 (c) shows the measured vertical displacement at the center of the membrane with respect to the applied pressure. The strain versus applied pressure can then be plotted by converting the measured vertical displacement to the corresponding strain using Equations 4.5-4.7 (figure 4.6 (d)).
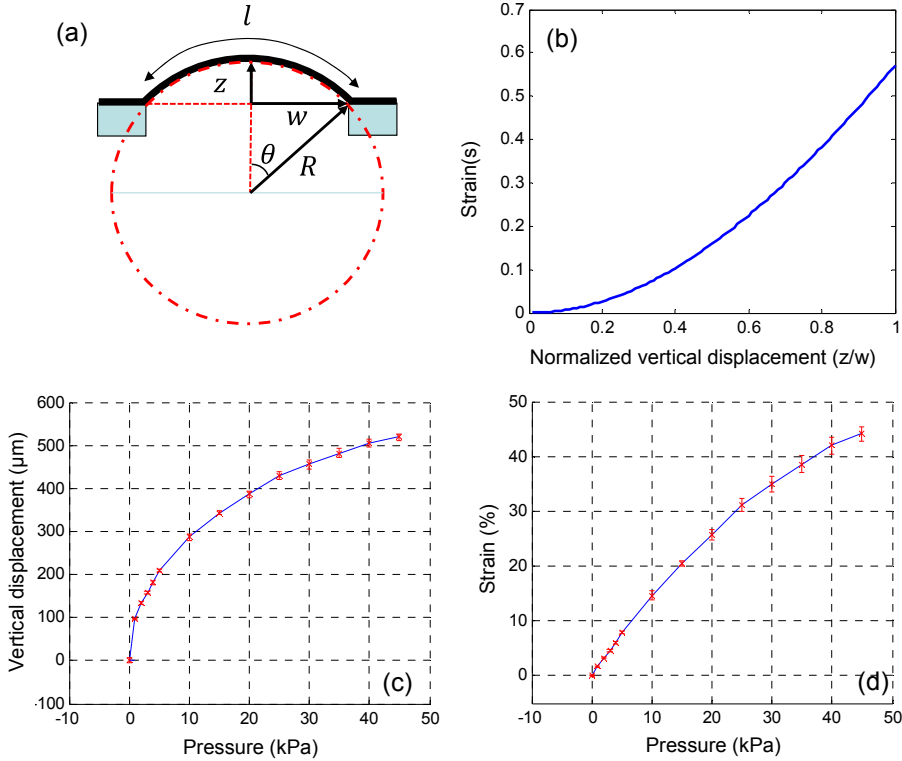
Figure 4.6 (a) Schematic transversal cross-section of the membrane inflated to a semi-cylindrical shape with radius R. (b) Calculated strain from the normalized vertical displacement. (d) Measured vertical displacement of the center of the membrane versus applied pressure (n=4). (c) Strain in the membrane versus applied pressure obtained by converting the vertical displacement measured in (c) to strain by using the geometrical relation shown in (b) with *2w* = 1.2 mm. Images b-d adapted from [104].

Inflating the membrane results in an increase in the original resistance of the interconnects due to exerted strain on the interconnects and bending. Figure 4.7 (b & c) show the measured relative resistance increase versus the applied pressure, and the equivalent transversal strain according to figure 4.6 (d). The resistance change is minimized by designing the trajectory of the electrical interconnects in such a way that the tracks experience minimal longitudinal strain during membrane actuation, and reduced interconnect bending as discussed in the mechanical design section of chapter 2. As demonstrated in figure 4.7 (c) the relative resistance change is less than 0.2 % for 20 % transversal strain in the membrane corresponding to 15 kPa of applied pressure.

For long term electromechanical characterization of the interconnects the membranes were cyclically stretched up to 20 % - which is the upper range of physiologically relevant strains - by cyclically applying a 15 kPa back pressure using a costume made pressure control system. As shown in figure 4.7a the original resistance of the tracks (46.75 kΩ) increases by less than 0.2 % in each pneumatic actuation cycle when the membrane is inflated to 20 % of strain, and returns to the original resistance by deflating the membrane. The histograms of logged resistance values in the first and last hour of the long term measurement session are shown in Figure 4.7 (d & e). The two peaks in each histogram correspond to the resistance values at the relaxed and inflated states of the membrane. The interconnects maintain their original resistance after more than 160 thousand deformation cycles as indicated by the similar resistance values corresponding to the histogram peaks in the beginning and in the end of the measurement session. The demonstrated stability of resistance values suggests that the interconnects conducting material, TiN, remains in its elastic deformation regime, as a result of increased bending radius at the elastomer to rigid substrate transition points, achieved by the gradual tapering of the corners of the dogbone, as well as the placement of the TiN tracks in the neutral bending plane of the parylene insulation.
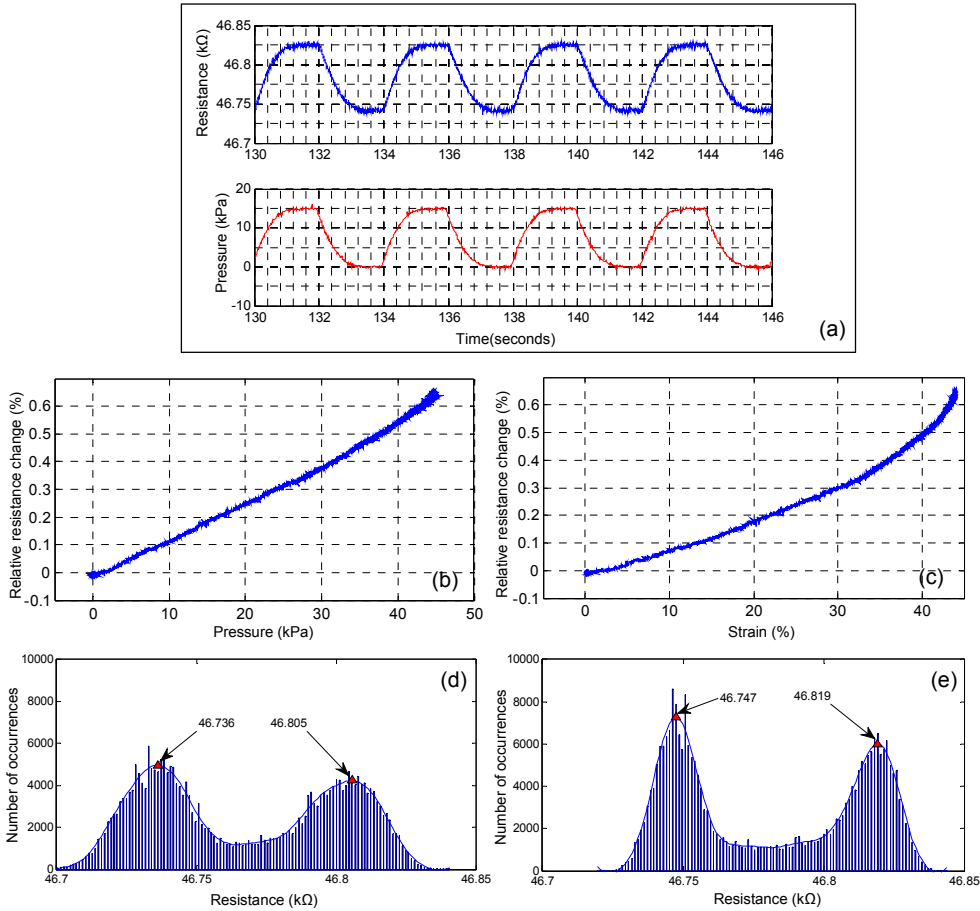
Figure 4.7 (b) A few periods of the logged resistance and pressure magnitude during electromechanical characterization. The interconnects show about 0.15 % (~70 Ω) reversible increase in resistance with respect to the original resistance value (46.74 kΩ) when the membrane is inflated with 15 kPa pressure resulting in 20 % of transversal strain in the membrane. For this curve a higher supply voltage was temporarily used to improve the signal to noise ratio for display purposes. (b) Resistance change relative to the original resistance versus applied pressure. The curve was obtained by logging the resistance while slowly ramping up the pressure (~0.75 kPa/second) in order to minimize the effect of time delay between pressure application and resistance change. (c) Relative resistance change versus the transversal strain equivalent of the applied pressure. (d, e) The histograms of logged resistance values in the first and last hour of the measurement session respectively, with sampling rate of 80 samples/second (number of bins=square root of number of samples). The two peaks in each histograms correspond to the resistance values of the interconnects at relaxed and inflated states of the membrane. As demonstrated in the two histograms the interconnects show similar resistance values in the beginning and at the end of the measurement session after more than 160 thousand deformation cycles. Images a,b,d and e adapted from [104].

4.3   Summary

In this chapter the electrochemical and electromechanical characterization of the SMEA chips was presented. The theory of the electrode-electrolyte double layer capacitance and the Electrochemical Impedance Spectroscopy (EIS) measurement methods were briefly discussed. The electrochemical characterization showed a characteristic impedance magnitude of 4.5 MΩ at 1kHz for each 12µm in diameter TiN electrode. A parasitic capacitance of 36 pF was measured between the electrolyte and each contact pad through the silicon substrate, as well as a parasitic capacitance of 1.3 pF/mm between the electrolyte and the parylene insulated interconnect tracks. The electrochemical properties of the SMEA devices proved to be sufficient for cellular measurements as demonstrated by field potential measurements from beating cardiomyocytes presented in the next chapter.

The resistance change of the interconnects with respect to the applied pressure and corresponding transversal strain in the membrane was characterized. The relative resistance change for 20 % transversal strain in the membrane was less than 0.2 %. The long term cyclic actuation of the chips demonstrated that the interconnects maintain their original resistance after more than 160 thousand cycles of 20 % stretching and relaxing, suggesting that the interconnects' conducting material, TiN, remains in its elastic deformation regime, as a result of mechanical design to reduce bending and exerted longitudinal strain on the interconnects.

Chapter 5 - Proof of concept cellular experiments

This chapter presents the cell culture experiments performed on the SMEA chips and the preliminary electrical measurements from cardiomyocytes on the platform. The first section presents the initial biocompatibility and imaging experiments. In the second section, after briefly explaining the origins of the field potential signal, the preliminary field potential measurements from spontaneously beating hESC cardiomyocytes under mechanical loading is presented.

5.1 Preliminary experiments with cells

The fabricated SMEAs were tested for compatibility with cell culture experiments and imaging techniques. To perform these tests, the chips were glued to the bottom of 12-well cell culture wellplates with an opening drilled in the center of the bottom of each well to have access to the membranes (Figure 5.1 (a)). In order to enable pneumatic actuation of the chips, the prepared wellplates were placed in a costume made holder that couples the pneumatic pressure supplied by a pressure control system to the backside of each chip (figure 5.1 (b)). During the culturing period the wellplate mounted in the holder was placed in an incubator while the actuation pressure was supplied to the holder through a tube inserted via an access opening in the rear of the incubator (figure 5.1 (c & d)).

For the initial biocompatibility tests, a Caco-2 colon cancer cell line which was readily available in the lab was used. The dividing cell lines can proliferate and therefore can be kept in culture for long periods and used for several experiments. In contrast, cardiomyocytes are unable to proliferate and therefore can be used only once in an experiment, and are consequently difficult and expensive to work with.

The membranes were firstly coated with fibronectin to promote cell adhesion. Subsequently, the cells were cultured and grown to confluency prior to subjecting them to 15 % cyclic stretching for in total of 16 hours spread over 3 days inside the incubator. The cells remained attached to the membrane, and no deterioration in the SMEA chips was observed under the microscope during this period, indicating

their robustness in a saline environment. To test the compatibility with imaging techniques the cells were fixed with paraformaldehyde and nuclear and actin cytoskeleton staining was performed. Since the PDMS membrane is only 20 µm thick, and transparent to UV excitation wavelengths used in confocal and fluorescent microscopy, the SMEAs allow for high magnification inverted microscopy. Figure 5.2 shows sample fluorescent and confocal microscopy images of the cells' nuclei and actin filaments for demonstration.
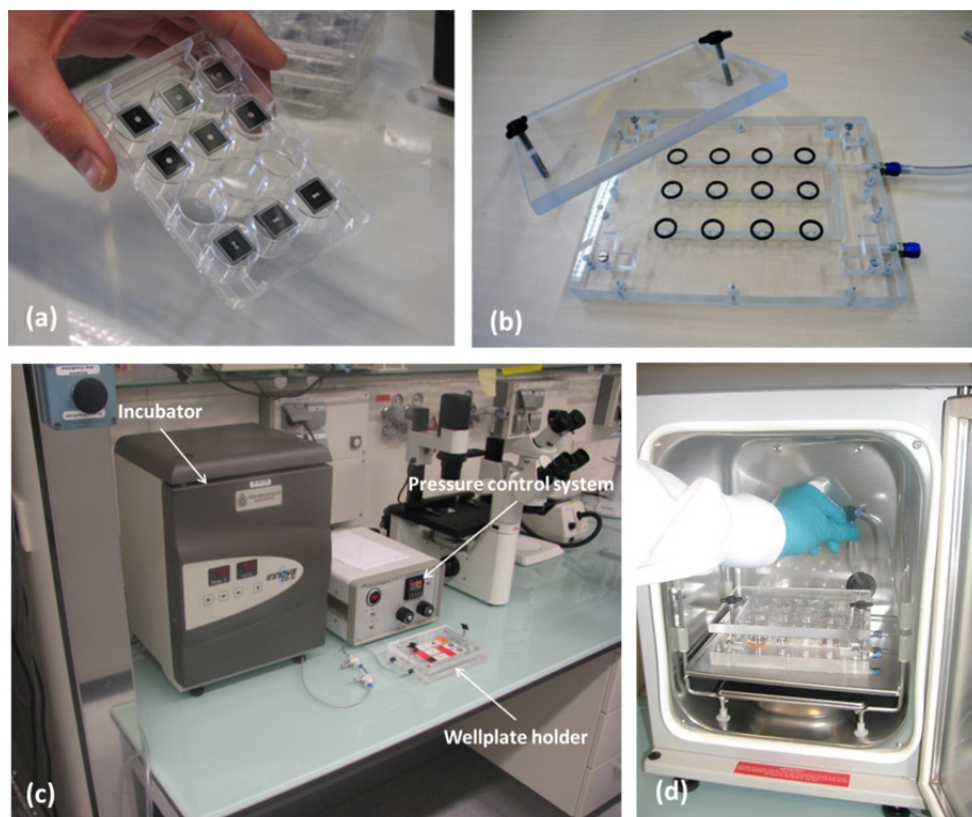
Figure 5.1 Photographs of (a) the chips glued to the bottom of a well-plate, (b) custom made well-plate holder enabling the application of controlled pressure to the back side of the chips, (c) the experimental set-up, including an incubator, the pressure control system and an inverted microscope, (d) the pneumatic connection from the pressure control system to the well-plate holder via an opening at the rear of the incubator.
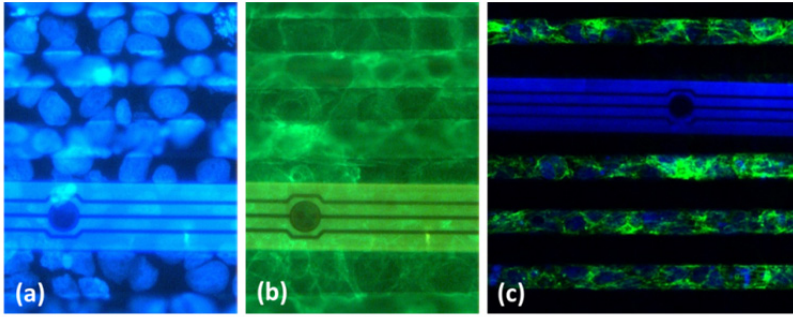
Figure 5.2 . (a, b) Fluorescent microscopy images of the cells' nuclei and actin filaments respectively, on a chip with longitudinal micro-grooves. (d) Combined confocal microscopy image. The focal plane in the image is a few microns below the surface, as a result only the cells inside the micro-grooves are visible. The parylene insulation of the interconnects exhibits some level of auto-fluorescence.

5.2   Field potential measurement from cardiomyocytes

In order to validate the main functionality of the platform to measure electrophysiological signals from cells under mechanical loading, hESC cardiomyocytes were cultured on the chips and their field potential signal was picked up by using Multichannel Systems MEA readout equipment, while subjecting the cells to mechanical loading by pneumatically actuating the chips in situ. In this section first the relationship between the field potential signal and the transmembrane action potential signal is briefly explained, followed by the obtained measurement result.

5.2.1   Field potential versus transmembrane action potential

As previously described in the introduction chapter, an action potential is generated as a result of membrane depolarization triggered by a chemical, mechanical or electrical stimulation [18]. The potential change across the membrane when membrane depolarization occurs is termed the transmembrane action potential (AP). The transmembrane potential can be measured with patch clamping techniques by electrically accessing the inside of the cell and directly measuring the potential difference between the inside of the cell and the outside electrolyte. The field potential (FP) signal however, is indirectly related to the action potential and is measured outside the cell membrane through electrodes.

When a cell generates an action potential, the potential changes in the close vicinity of the cell - in the order of the Debye length corresponding to the culture medium

electrolyte (~ 80 nm) - can be picked up by an external electrode. Further away from the cell, the potential change is shielded by the counter ions. Therefore, good adhesion of the cells to the electrode ensuring minimal distance is necessary to enable proper recording of the potential changes through the electrodes. Moreover, it should be taken into account that the cells adhere to surfaces through focal adhesion points, resulting in a gap of about several tens of nanometers between the cell membrane and the culturing surface filled with electrolyte as schematically illustrated in Figure 5.3a. If the distance between the cell membrane and the electrode is small enough, the generated action potential by the cell is coupled to the electrode through the cell membrane impedance, denoted by the cell membrane capacitance C_m and resistance R_m, and further to the amplifier through the electrode impedance [106]–[108]. In case the cell partially covers the electrode or the adhesion is poor, an unwanted "leakage" path to the electrolyte - denoted by C_{seal} - will reduce the signal magnitude picked up by the electrodes. This leakage impedance is especially problematic for single cell measurements on large electrodes, however, if the electrode is fully covered by a layer of cells that form cell to cell tight junctions as demonstrated in Figure 5.3 (c) - which is the case for cardiomyocytes forming a synchronously beating layer - the mentioned leakage path can be neglected.

Figure 5.3 (b) shows the circuit diagram of the field potential measurement according to the schematic illustration in Figure 5.3 (a). The combination of the cell membrane impedance and the electrode impedance forms a high-pass filter, which acts on the action potential before it reaches the amplifier. As a result, the signal picked up by the amplifier (the field potential signal V_{FP}) is a high-pass filtered version of the transmembrane action potential, V_{AP}. As an example, figure 5.4 shows the effect of removing the low frequency components from the action potential signal by applying a high-pass filter while progressively increasing the cut-off frequency. It can be observed that if the cut-off frequency of the highpass filter is low enough, the shape of the filtered signal better resembles the original action potential shape. By using a larger electrode for the measurement, both the electrode capacitance and the capacitance of the cell membrane portion on top of the electrode increase, resulting in a lower cut-off frequency for the high-pass filter and more low frequency components of the action potential reaching the amplifier. Consequently, the measured field potential more closely resembles the original action potential.
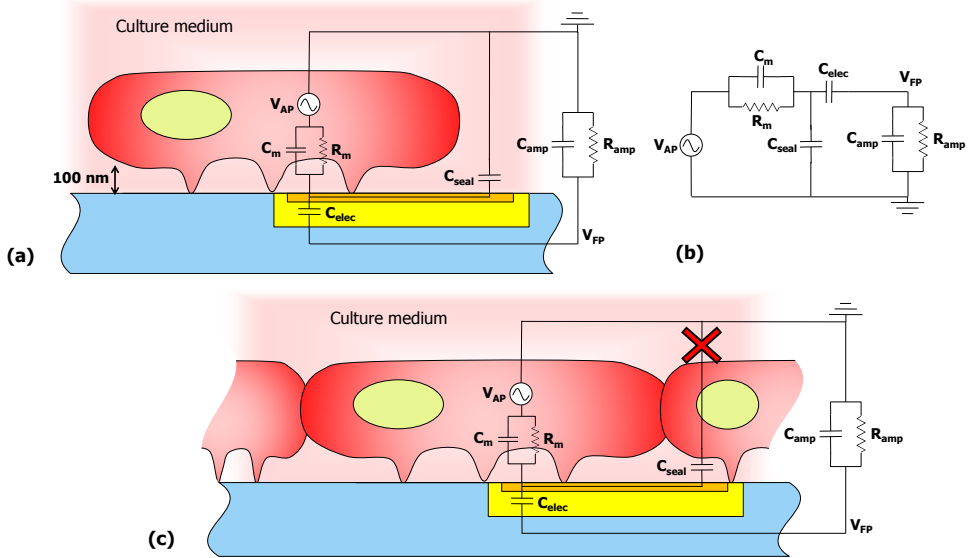
Figure 5.3 (a) Schematic depicting a cell body adhering through focal adhesion points to a substrate containing an electrode, overlaid with circuit elements involved in the field potential measurement. The culture medium is electrochemically connected to the amplifier's ground through either a Ag/AgCl electrode immersed in the culture medium, or a dedicated electrode in the culture substrate with large surface area - relative to the microelectrodes - that is not covered with cells, providing a negligible electrochemical impedance compared to the rest of the circuit elements (not illustrated in the picture). (b) Circuit diagram of field potential measurement. The action potential is highpass filtered through the cell membrane and electrode impedance before it is fed to the amplifier. The existence of the leakage impedance, C_{seal} decreases the signal magnitude due to impedance division before reaching the electrode. (c) When the electrode is fully covered by a layer of cells forming cell to cell tight junctions the leakage path can be avoided resulting in a stronger signal reaching the electrode.

It is worthwhile in this context to mention that, due to mechanical manipulation or electrical stimulation tears in the cell membrane might appear. Through this tear the intracellular environment connects to the extracellular electrolyte through a resistive path as denoted by R_{tear} in Figure 5.5. The value of R_{tear} depends on the size of the tear, and can be much smaller than the membrane impedance and therefore can bypass the membrane impedance resulting in less highpass filtering of the action potential according to the circuit model of Figure 5.3b. As a result, before the cell repairs the membrane, temporarily the recorded field potential signal is more similar to the transmembrane action potential as described in Figure 5.4. This phenomenon has been observed during electrical stimulation of the cells, and also in the stretching experiments presented in the following sections.
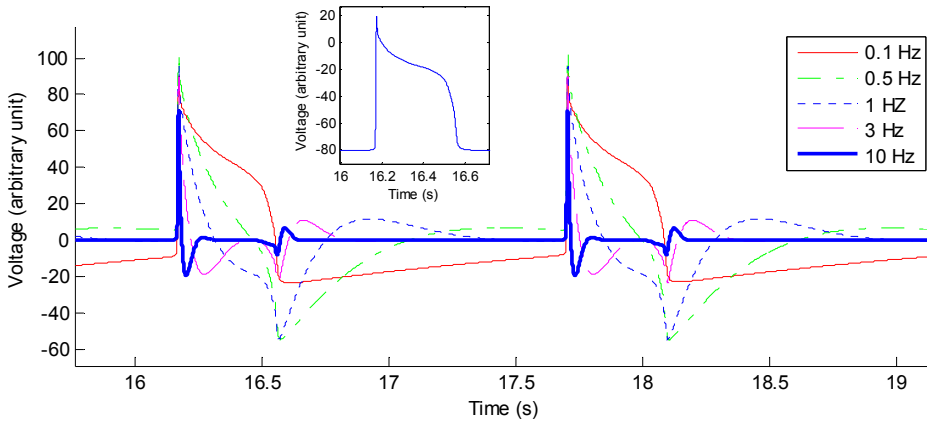
Figure 5.4 The effect of highpass filtering on the action potential shape. The inset shows the original shape of one period of the action potential signal. Increasing the cut-off frequency of the highpass filter from 0.1 to 10 Hz results in removal of more low frequency components from the original action potential signal and introduces extra ripples in the signal. To produce the illustration a second order Butterworth highpass filter was applied on a software generated periodic action potential signal using a MATLAB script.
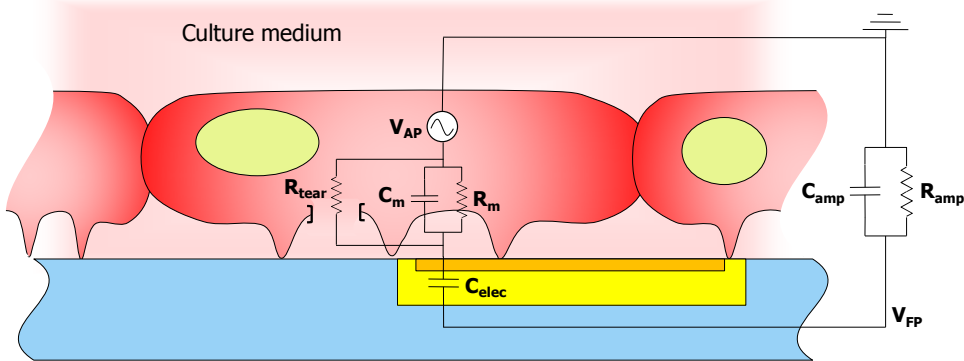
Figure 5.5 The picture depicts a tear in the cell membrane due to mechanical manipulation or electrical stimulation. The tear connects the intracellular environment to the extracellular culture medium through a resistive path denoted by R_{tear}.

5.2.2   Improving cardiomyocytes adhesion to PDMS

In order to perform stretching experiments on the cardiomyocytes their stable adhesion to the substrate is necessary, otherwise the cells would slide on the stretching substrate and would not be properly subjected to the applied mechanical loading. As mentioned before to promote the adhesion of cells to commonly used cell culture substrates like polystyrene or glass, an extracellular matrix (ECM) protein coating such as collagen, laminin and fibronectin is used. These ECM

proteins have binding sites that the cells can bind to through specific transmembrane proteins [69]. However, the used ECM protein should have proper conformation - i.e. the folding structure of the protein - after coating to expose those binding sites. The post coating conformation can depend on physical and chemical properties of the substrate, and even the surface concentration of the protein coating [69], [75], [109]. Moreover, for different types of cells different types of ECM protein coatings are used, and some cell types relatively quickly deposit their own matrix proteins after attachment while other cell types do not, leading to different attachment results for different types of cells on similarly coated substrates [69].

For cardiomyocytes, fibronectin has been previously reported to promote adhesion to a variety of substrate materials [9], [54], [77]. However, on plane PDMS the physically adsorbed fibronectin tends to desorb over time [75], [110], and the contractile nature of cardiomyocytes might exacerbate this process, resulting in poor adhesion and spreading of the cells after seeding, and their detachment from the substrate after a few days as observed in our experiments. To realize a stable chemical bond, rather than merely physical adsorption between ECM proteins and substrates like glass or PDMS, organosilanes have been employed as an intermediate molecular layer [110], [111].

As described previously in the microfabrication chapter, the organosilanes have the form: $R\text{-}Si\text{-}(X)_3$ in which silicon is the center of the organosilane molecule, the X is a hydrolyzable group, typically alkoxy (methoxy or ethoxy), and R is a nonhydrolyzable organofunctional group like amino, vinyl, epoxy, etc. The X groups react with water to form silanol groups (Si-OH) which then react with the activated surface of the substrate that contains hydroxyl groups (-OH) to form a covalent bond. The organofunctional group of the organosilane is then available to chemically bond to the subsequently added biopolymers, e.g. fibronectin.

In our experiments the organosilane aminopropyltrimethoxysilane (APTMS) was used, with a similar protocol as described in [110]. Prior to silane coating the PDMS surface of the chips was activated by shortly exposing it to an oxygen plasma to form the hydroxyl groups. The chips were subsequently coated with fibronectin before seeding the cardiomyocytes. The detailed coating protocol is presented in appendix 2. As shown in figure 5.6 the cardiomyocytes show poor attachment and tend to clump together after seeding on chips coated only with fibronectin. The adhesion and spreading of cardiomyocytes is notably improved by

treating the substrate with the silane prior to fibronectin coating. The cells maintain their adhesion to the substrate during stretching experiments, as optically observed under the microscope, and demonstrated by the consistent quality of the field potential recordings presented in the next section
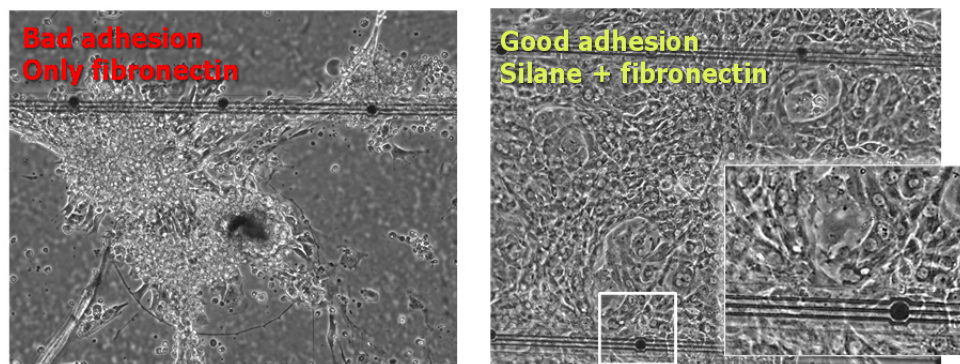
Figure 5.6 Optical microscopy images of hESC cardiomyocytes cultured on the chips. (left) Poor adhesion and spreading of cardiomyocytes on chips coated with only fibronectin (either with or without plasma treatment of PDMS before fibronectin coating). The cells have clumped together one day after seeding. (right) By treating the substrate with APTMS prior to fibronectin coating, the adhesion and spreading of cardiomyocytes is notably improved.

5.2.3   Field potential measurement under mechanical loading

The hESC cardiomyocytes used in the experiments were obtained from Pluriomics in frozen vials. After thawing and adjusting the cell concentration, for each chip 10 µl of the cell solution containing 15 k cells was dispensed on the pre-coated membranes under a stereo microscope and subsequently incubated. The cells form a beating syncytium already on day 2 of culturing.

The field potential measurements under mechanical loading were performed on day 7 of culturing. For the measurements, the chips containing the cultured cardiomyocytes are first mounted in the electro-pneumatic adapter (figure 5.7 (b)). The adaptor is subsequently placed in the Multichannel Systems MEA readout head stage and a controlled pressure is supplied to the adaptor through the pneumatic connector on the PCB, for the application of in situ mechanical loading during electrical read-out (figure 5.7 (c)). During the measurements an Ag/AgCl electrode immersed in the culture solution and connected to the ground of the amplifier was used as the ground/reference electrode. Additionally, the chips under measurement were covered with an opaque box, in order to eliminate the photovoltaic noise generated in the silicon substrate in the presence of light, as

mentioned in the previous chapter. The electrical layout of the chips and a screenshot of the field potential recording from the spontaneously beating cardiomyocytes on all 12 electrodes are shown in figure 5.8.
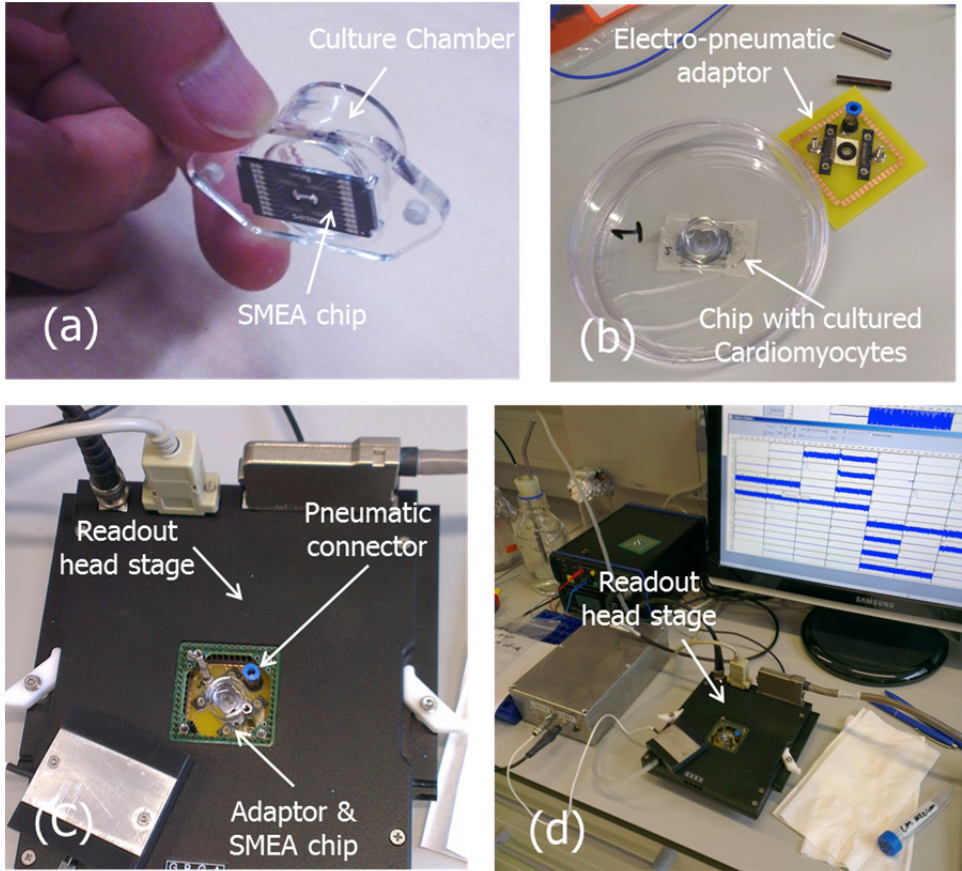
Figure 5.7 (a-d) Elements of the measurement set up. The chips containing the beating cardiomyocytes are first mounted in the electro-pneumatic adaptor. The adaptor which has the same foot print as the commercial MEAs is then placed in the read-out head stage. Subsequently a tube connects the pneumatic connector on the adaptor to the pressure control system (not shown in the pictures) for in situ pneumatic actuation of the SMEA.

Two types of mechanical loading, that is static and cyclic, were applied to the cells during the field potential recordings. For the static stretch case, a step pressure of 15 kPa, corresponding to 20 % of stretch, was applied to the back side of the membrane. The recorded electrophysiological response of the cardiomyocytes to this static stretch is shown in figure 5.9. Immediately after the application of the static stretch, a sudden decrease in the beat rate of cardiomyocytes was observed as

shown in figure 5.9 (a, b). The beat rate gradually recovers over a period of about one minute. The transient effects of stretch on ventricular cardiomyocytes have been previously reported [112], [113]. The observed change in the duration of the field potential immediately after stretch is shown in figure 5.9 (d), as previously reported [42], [43]. The presented recordings demonstrate the capability of the platform to capture the dynamic changes in the field potential signal in response to the applied static stretch.
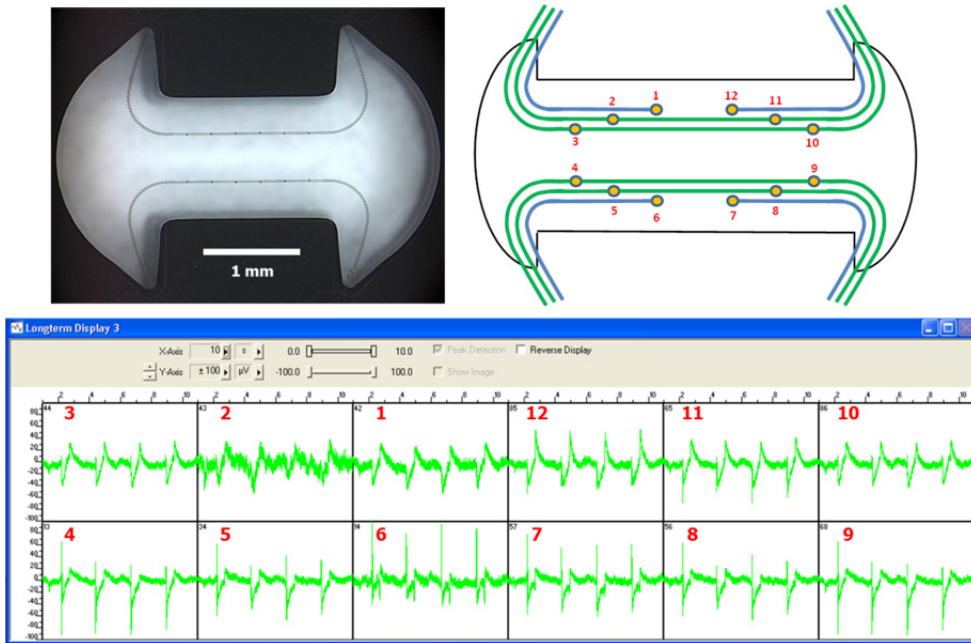
Figure 5.8 (top) The actual layout of the SMEA membrane and the schematic electrical layout of the electrodes and interconnects on the membrane. (bottom) A screen shot of field potential recording from all electrodes.

As shown in figure 5.9 (b, c), a transient fluctuation is observed in the recorded signal when the membrane is pneumatically inflated. This fluctuation in the recorded signal from the electrodes is also observed in the absence of cells when the membrane is actuated. Therefore, the observed fluctuation could be attributed to the movement of the electrolyte with respect to the electrodes as a result of the vertical movement of the membrane during actuation. The resistance change of the interconnects due to actuation is less probable as the cause for the observed signal fluctuation, since the amount of this resistance change (as measured in the previous chapter) is extremely small compared to the input impedance of the amplifier.
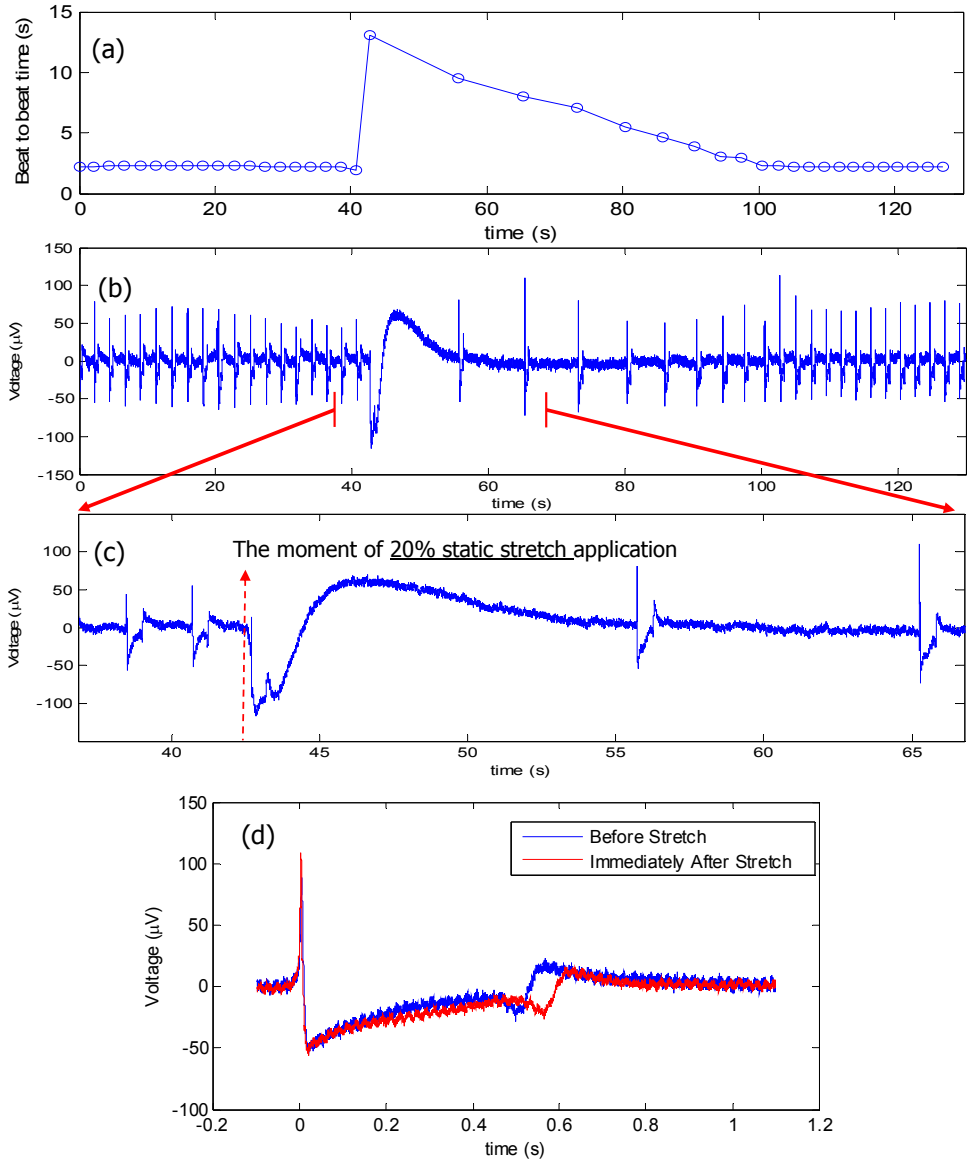
Figure 5.9 (a) The beat to beat time increases immediately after the application of 20 % static stretch and recovers over time. (b & c) The field potential recording from electrode #7 and the zoomed in view of the recording, showing the dynamics of the measured signal after the application of the stretch. (d) The observed duration of the field potential before and immediately after the application of the static stretch. To reduce the mains 50 Hz noise, each field potential signal is averaged for 3 consecutive periods before and after stretch application.

For cyclic mechanical loading, a periodic 10 kPa pressure pulse with 0.5 Hz frequency an 50 % duty cycle was applied to the SMEAs. In this way the membranes were stretch up to 15 % and subsequently relaxed cyclically. Figure 5.10 (a) shows the recorded signal from one of the electrodes. It can be observed that the field potential of the beating cells is superimposed on a cyclic fluctuation - as described before - which has the same frequency as the actuation pressure pulse. Since, this fluctuation has lower frequency components compared to the field potential signal, it can be effectively removed by applying a digital highpass filter to the recorded signal as demonstrated in figure 5.10 (b).
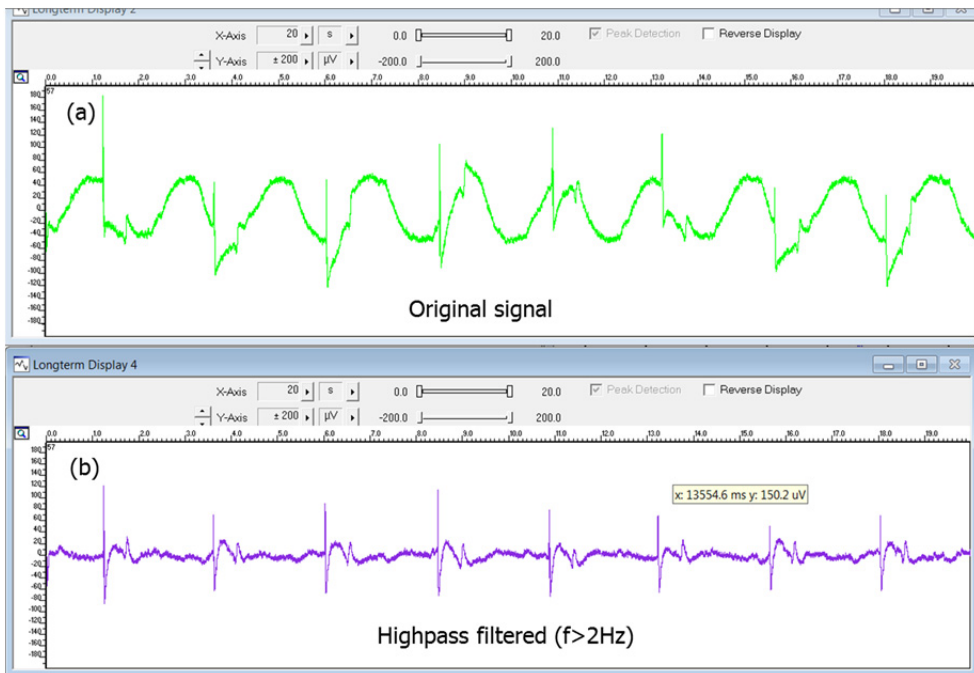
Figure 5.10 (a) Cyclic fluctuation observed in the measured signal during cyclic actuation of the membrane (actuation frequency: 0.5 Hz). (b) The fluctuation can be effectively removed by applying a digital high pass filter to the measured signal. Here a highpass filter with the cut off frequency of 2 Hz has been applied.

In the presented field potential recording for cyclic mechanical loading, the beating of cardiomyocytes is not synchronized with the applied stretching rhythm. In order, to reproduce the in vivo physiological conditions in the in vitro cellular experiments, in each beating period, the SMEA membrane should be inflated to stretch the cardiomyocytes (diastole) and subsequently at the start of the next

action potential - which triggers the contraction of cells - the membrane should be deflated to let the cells contract (systole). Therefore, the pneumatic actuation of the SMEA membranes should be synchronized with the action potential timing of the cardiomyocytes. This can be achieved by pacing the cells with in situ electrical stimulation and feeding the corresponding trigger-out signal from the stimulation system to the pneumatic pressure control system for synchronization. Alternatively, the field potential read out system can generate triggers from the intrinsic beating rhythm of the cells which can be fed to the pressure control system for synchronized actuation. By varying the actuation pressure and frequency, different preload conditions can be simulated. By introducing predefined time delays between the onset of the action potential and the membrane deflation, controlled arrhythmic conditions can be reproduced as well.

The presented cell culture experiments and field potential measurements demonstrated the proof of concept usage and capabilities of the platform. Based on the demonstrated capabilities, the platform can be utilized in a proper experimental setting to study the dose-response curves for cardiotoxic effects of drug compounds under variable simulated cardiac preload conditions.

5.3   Summary

In this chapter the functionality of the chips for cell culture and field potential measurement was investigated. The initial cellular experiments with a Caco-2 colon cancer cell line demonstrated the compatibility of the chips with cell culture and imaging techniques. For field potential measurements hESC Cardiomyocytes were used. The cardiomyocyte showed poor adhesion to the membrane with normal fibronectin coating. The adhesion was improved by modifying the culture surface with an organosilane prior to fibronectin coating.

The relation between the transmembrane action potential and filed potential was discussed, followed by presenting the field potential measurement results from spontaneously beating cardiomyocytes subjected to in situ static and cyclic mechanical loading. The presented measurement results serve as proof of concept, demonstrating the capabilities of the platform to be employed as a useful tool in electrophysiological studies with mechanical loading. For the cyclic loading case, the synchronization of the pneumatic actuation system with the electrical pacing of

the cardiomyocytes should be incorporated in the platform in order to enable in vitro physiological simulation of variable preload conditions.

Chapter 6 - General conclusions and recommendations

6.1 Conclusions

In this thesis the design, fabrication and characterization of a novel platform for in vitro electrophysiological measurements is presented. The platform allows for in situ mechanical loading of cells, and is specifically aimed for cardiotoxicity drug screening applications. The platform is based on pneumatically actuated Stretchable Micro-Electrode Array (SMEA) chips which are fabricated using state of the art silicon micro-fabrication technology. The main technological challenges addressed in this thesis were, firstly, the mechanical design of the electrical interconnects for the stretchable devices, and secondly, a manufacturable micro-fabrication technology to enable high volume production of the SMEA chips. The electro-chemical and electro-mechanical characterization of the chips are presented, together with proof of concept field potential measurements from human stem cell derived cardiomyocytes under cyclic mechanical loading.

The novel mechanical design for the electrical interconnects presented in chapter 2, shows that the interconnects for the SMEA can be realized without the need for space-demanding meandering designs, or the use of unconventional stretchable conductive materials which are not suitable for micro-fabrication. In this approach the optimal routes for the interconnects which result in minimal stress in the tracks were determined based on the magnitude and direction of the 1st and 2nd principal strains in inflated membranes obtained from mechanical FEM simulations. The interconnect routes were designed to be perpendicular to the 1st principal strain direction and if possible pass through regions with minimal 2nd principal strain magnitude.

Based on these design rules two different designs for the SMEAs are proposed, namely the circular and dogbone designs. In the circular design the interconnects have a spiral shape perpendicular to the direction of the 1st principal (radial) strain and dimensioned mechanically to withstand the 2nd principal (tangential) strain. In the dogbone design, the concave corners in the geometry of the membrane result in

regions with virtually zero 2nd principal strain magnitude providing optimal locations for the interconnect tracks. While for the circular design the tangential strain in the membrane always results in stress in the interconnect tracks, in the dogbone design, due to the routing of the interconnects through the 2nd principal strain zero-crossing, higher levels of strain in the membrane are achievable with less stress development in the interconnect tracks compared to the circular design. The dogbone design also provides unidirectional strain in the functional area of the membrane containing the electrodes, which enables directional stretching of the cells. Therefore, for the electrophysiological measurements under stretch and the electromechanical characterization the dogbone design was preferred.

In chapter 3 the micro-fabrication technology for embedding the electrodes and electrical interconnects in free standing PDMS membranes is presented. In order to enable large scale production of the SMEAs a manufacturable fabrication method was developed based on state of the art silicon micro-fabrication technology and materials. In the proposed microfabrication process in order to avoid the problems normally associated with thin film processing on top of elastomers, a "elastomer last" approach was employed.

In this approach all of the micro-structures including the electrodes (TiN), electrical interconnects (TiN isolated with parylene) and sacrificial photo resist micro-molds for the surface micro-features are initially fabricated on a silicon wafer. A thin layer of elastomer is then applied on top of the fabricated structures, and subsequently the structures are transferred to the elastomeric membrane by removal of the underlying silicon substrate using Deep Reactive Ion Etching (DRIE) from the backside, and dissolving the sacrificial photo resist molds. The micro-fabrication challenges mainly arising from the residual stresses in the deposited layers, and insufficient interlayer adhesions, as well as unconventional challenges with sacrificial photoresist processing, PDMS patterning and crack-free release of the SMEA membranes, were discussed in detail and addressed practically.

The characterization of the fabricated chips is presented in chapter 4. The electrochemical characterization of the electrodes using Electrochemical Impedance Spectroscopy (EIS) showed a characteristic impedance magnitude of 4.5 MΩ at 1 kHz for a 12 μm diameter TiN electrode. The measured characteristic impedance is higher than that of commercially available MEAs which is normally bellow 1 MΩ. This is attributed to the small size and flat surface of the electrodes.

However, the electrochemical properties of the SMEAs proved to be sufficient for field potential measurements from synchronously beating layers of cardiomyocytes.

The resistance change of the interconnects as a result of the transversal strain in the membrane and out of plane bending was characterized for the dogbone chips. The relative resistance change for 20% transversal strain in the membrane was less than 0.2 %. The long term cyclic actuation of the chips demonstrated that the interconnects maintain their original resistance after more than 160 thousand cycles of 20 % stretching and relaxing. This suggests that the interconnects' conducting material, TiN, remains in its elastic deformation regime, as a result of the mechanical design to reduce bending and exerted longitudinal strain. As a result, the chips can be used for long term field potential measurements under cyclic loading, as well as for in situ stretch induced maturation of the cardiomyocytes prior to drug screening tests.

Finally, the proof of concept cell culture and field potential measurements from human stem cell derived cardiomyocytes under cyclic mechanical loading is presented in chapter 5. The experiments show that in order to achieve sufficient adhesion of cardiomyocytes to the SMEA membrane, a combination of organosilane and ECM protein coating is required. The organosilane aminopropyltrimethoxysilane helps stabilizing the ECM protein fibronectin which normally tends to desorb from PDMS surface over time. Microscopy observations and the stable quality of the measured field potential signal during cyclic stretching confirm the proper adhesion of the cells to the SMEA membranes. However, further experiments are required to ensure long term stability of cell adhesion over a few days of continuous actuation. The cyclic movement of the membrane during actuation introduces a cyclic fluctuating artifact in the measured signal which can be attributed to the movement of the electrolyte with respect to the electrodes. This cyclic fluctuation is a low frequency signal, in phase with the cyclic actuation frequency, and can therefore be effectively removed by applying a highpass digital filter to the measured signal while preserving the original field potential signal content.

The presented results in this thesis demonstrate a robust design and manufacturable technology for SMEAs, as well as the proof of principle functionality of the platform to simulate in situ cyclic loading of cardiomyocytes while performing electrophysiological measurements. Based on the obtained results, it is now

possible to devise different types of experiments to verify the potential improvements of cardiotoxicity detection by including the mechano-electric coupling effects in the model. In addition to screening applications, the platform can be utilized to develop disease models where cell stretch and electrical activity play a role.

6.2   Recommendations

Based on the results and insights of this thesis work, the following general recommendations are formulated for future work to improve the performance of the SMEA platform in terms of design and functionality:

- The signal to noise ratio of field potential measurements can be improved by increasing the effective electrochemical contact surface area of the electrodes, resulting in lower electrode impedance. By simply increasing the geometrical size of the electrodes a lower impedance can be obtained. However, in order to preserve the spatial resolution, the surface area can be increases by introducing roughness on the same geometrical surface area of the electrodes. Electro-deposition of porous conductive polymers such as PEDOT and incorporating carbon nano-tubes on the surface of electrodes have been reported to achieve lower electrode impedances. In the proposed micro-fabrication process for the SMEAs in this thesis, increased surface area can also be achieved by etching micro-cavities in the DRIE etch stop oxide layer on top of which the electrode metallization is deposited. In this way increasing the electrode surface area can be seamlessly integrated in the microfabrication process without the need for additional post fabrication processes.

- The SMEA membranes are located at the bottom of a through wafer etched cavities in the silicon substrate. As a result, after cell culture the silicon substrate comes in contact with the culture medium electrolyte. Normally, for field potential measurements the culture medium is connected to the amplifier's ground through an Ag/AgCl electrode. Consequently, the parasitic capacitance between each contact pad and the silicon substrate provides a parasitic path to the grounded electrolyte, resulting in attenuation of the field potential signal through impedance division before the amplifier input. This parasitic capacitance can be reduced by reducing

the size of the contact pads, as well as increasing the thickness of the oxide isolation layer between the contact pad metallization and the silicon substrate. This parasitic path can also be removed by preventing contact between the silicon substrate and the electrolyte by incorporating an insulating layer on the silicon surface where contact with the electrolyte is possible. Another solution is to use an insulating material for the substrate instead of silicon, however that entails significant modifications to the microfabrication process.

- The photovoltaic noise that is generated in the silicon substrate when exposed to light, appears in the electrical measurements through the parasitic capacitance between the contact pads and the silicon substrate. This noise was eliminated during characterization and field potential measurements by covering the chips with an opaque plastic box. However, this noise can be problematic in case the field potential measurements have to be performed in the presence of light, such as illumination for optical or fluorescence microscopy. Apart from reducing the parasitic capacitance of the contact pads, a possible way to reduce this noise is to use highly doped silicon as the substrate. In that case the silicon substrate can as well be used as the ground electrode. Another solution, as mentioned in the previous item, is to use an alternative material instead of silicon for the substrate.

- In order to enable direct electro-pneumatic interfacing with the SMEA chips for prototype characterization and preliminary cellular measurements, the existing layout of the SMEA chips incorporates relatively large electrical contact pads, alignment notches at the corner of the chips, and sufficient space around the membrane area for pneumatic sealing with an elastic O-ring. The mentioned provisions result in a relatively large chip area. To increase the number of chips per wafer for actual production, the layout of the chips should be modified to decrease the size of the chips and the contact pads, combined with a proper MEMS packaging scheme which enables inverted microscopy of the SMEA membranes. Moreover, to improve manufacturability, alternative isolating material instead of parylene can be used such as spin on photo-patternable polyimides.

▪ Since the mechanical properties of the membranes might drift during long term cellular experiments under cyclic actuation, a means to measure the actual membrane stretch in situ might be required to enable closed loop control of the pneumatic pressure to achieve a certain level of stretch. This can be achieved by in situ non-contact measurement of the membrane inflation height or profile to estimate the strain in the membrane.

▪ Decreasing the thickness of the SMEA membranes might enable detection of contraction force of cardiomyocytes, as has been already demonstrate by the cellDrum technology [11]. In that case a lower pressure would be required to inflate the membrane and as a result the contraction force of the attached cardiomyocytes might be able to induce a measureable deflection in the inflated membrane proportional to the contraction force.

▪ Finally, since diverse types of micro-features can be integrated on the surface of the SMEA membranes, an array of cellular experiments can be used to find the features which induce optimal alignment for the cardiomyocytes. In such experiments care should be taken, since cyclic stretch also induces cell alignment. It has been reported that in case cyclic stretch is applied to cardiomyocytes cultured on silicone dishes shortly after seeding (3 h), it can induce alignment in parallel to the stretch direction. However, if the cyclic stretch is applied long enough after seeding (24 h) such that the cell to cell adhesions are already formed, no alignment is induced by the cyclic stretching [114], [115]. Therefore, further cellular experiments are required to study the combined effects of micro-features and cyclic stretching on the alignment of cardiomyocytes [57], as well as the effect of time scale, frequency and magnitude of the applied cyclic stretch [116].

Appendix 1- Fabrication process

#	Equipment	Process	Parameter/Details	Comments
1- Stepper alignment marks				
1	Cintillo	wafer cleaning	hzplus 15min + fzplusHcl	
2	laktrack	Resist spin coat	150mm_TMSDEA_HPR504_4000_rpm_EBR	
3	Stepper	expose alignment marks	dose 150 focus 0 (mj/cm^2, μm)	
4	laktrack	develop	150mm_HPR504_develop	
5	Verteq rinser/dryer	rinse dry		
6	STS CPX clustertool	etch silicon	140 nm	
7	Barrel	Strip resist	O2 plasma, 1000W, 30min	
8	Cintillo	wafer cleaning	hzplus 15min + fzplusHcl	
2- Oxide for back side hard etch mask and front side deep etch stop				
9	Novellus PECVD	PECVD oxide on backside	4μm "zero-stress PECVD oxide"	backside hard etch mask
10	Cintillo	wafer cleaning	hzplus 15min + fzplusHcl	
11	Novellus PECVD	PECVD oxide on frontside	1μm "zero-stress PECVD oxide"	frontside deep etch stop
12	Cintillo	wafer cleaning	hzplus 15min + fzplusHcl	
13	laktrack	Resist spin coat on backside	150mm_TMSDEA_HPR504_2000_rpm_EBR	
14	Stepper	expose BACK	2x dose 150 focus 0 (mj/cm2, μm)	2 times exposure due to roughness of the backside
15	laktrack	develop	150mm_HPR504_develop	
16	Verteq rinser/dryer	rinse dry		
17	STS CPX clustertool	etch oxide on the backside	4μm thick oxide etch	
18	Barrel	Strip resist	O2 plasma, 1000W, 30min	
19	Cintillo	wafer cleaning	hzplus 15min + fzplusHcl	
3- Ti UV block layer				
20	CVC Connexion 800 / Veeco 2 Nexus	Sputter deposition	20nm sputter etch + 100 nm Ti on front side	UV block layer
21	laktrack	Resist spin coat	hpr504 1500 rpm	
22	Stepper	expose UVB	dose 170 focus 0 (mj/cm2, μm)	pattern the UV block layer
23	laktrack	develop	150mm_HPR504_develop	

25	Verteq rinser/dryer	rinse dry		
25	STS CPX clustertool	etch 100nm Ti	100 nm with ICP Ti01	
26	Barrel	O2 plasma descum	600w 90°C 3min	
27	laktrack	acetone strip		
28	Fuming Nitric Acid HNO3 100%	Fuming nitric acid cleaning +rinsing	10min	
29	Novellus PECVD	PECVD oxide deposition on frontside	1µm "zero-stress PECVD oxide"	
4- TiN/Al interconnects and contact pads				
30	CVC Connexion 800 / Veeco 2 Nexus	Sputter deposition	10nm sputter etch + 100 nm TiN/300nm Al on front side	
31	laktrack	Resist spin coat	150mm_TMSDEA_HPR504_2000_rpm_EBR	
32	Stepper	expose AL	dose 170 focus 0 (mj/cm2, µm)	
33	laktrack	develop	150mm_HPR504_develop	
34	Verteq rinser/dryer	rinse dry		
35	STS CPX clustertool	oxide dry etch	100nm oxide etch	
36	STS CPX clustertool	etch 300nm Al/100 nm TiN stop on oxide	ICP Al01	
37	Barrel	O2 plasma descum	2x 600w 90°C 2min	Remove cross-linked resist
38	laktrack	acetone strip		
5- First layer parylene				
39	Fuming Nitric Acid HNO3 100%	Fuming nitric acid cleaning +rinsing	10min	
40	Verteq rinser/dryer	rinse dry		
41	KS spinner RC8	manual AP3000 primer spin coat	5ml, 100rpm 10s OL + 2000rpm 60s CL	
42	SCS Labcoter	Parylene deposition	2µm	
43	STS CPX clustertool	strip parylene on the backside	ICP-PAR01, for 9min	strip parylene from the backside
44	KS spinner RC8	manual AZ9260 spin coat and soft bake	500rpm 10s CL + 3000rpm 60s CL, hotplate 90°C 10min	4.2µm resist thickness
45	Stepper	expose ELEC	dose 360 focus 0 (mj/cm2, µm)	
46	laktrack	develop	150mm_az4533_develop_thick	

47	Verteq rinser/dryer	rinse dry		
48	STS CPX clustertool	etch parylene	ICP-PAR03, for 75s+10S	
49	Barrel	O2 plasma descum	2x 600w 90°C 2min	
50	laktrack	acetone strip		
6- TiN electrodes and interconects				
51	CVC Connexion 800 / Veeco 2 Nexus	Sputter deposition	20nm sputter etch + 100 nm TiN	
52	EV coating system	Resist spin coating	SPR660 4000rpm	
53	Stepper	expose INT	dose 170 focus 0 (mj/cm2, µm)	
54	EV coating system	developposte exposure bake and develop	SPR660-develop	
55	STS CPX clustertool	etch 100nm TiN	100nm with ICP TiN01	
56	Barrel	O2 plasma descum	2x 600w 90°C 2min	
57	laktrack	acetone strip		
7- Second layer paylene				
58	Barrel	O2 plasma descum	600w 90°C 2min	surface activation
59	SCS Labcoter	Parylene deposition +in situ priming	A174 in situ vapor priming, 2µm parylene	
60	STS CPX clustertool	strip parylene on the backside	ICP-PAR01, for 9min	strip parylene from the backside
61	KS spinner RC8	manual AZ9260 spin coat and soft bake	500rpm 10s CL + 2000rpm 60s CL, hotplate 90°C 10min	6µm resist thickness
62	Stepper	expose PAR	dose 300 focus -3 (mj/cm2, µm)	
63	laktrack	develop	150mm_az4533_develop_thick	
64	Verteq rinser/dryer	rinse dry		
65	STS CPX clustertool	etch parylene	ICP-PAR03, for 2m:10s+20S	4µm parylene etch
66	Barrel	O2 plasma descum	2x 600w 90°C 2min	
67	laktrack	acetone strip		
8- Resist mold				
68	Barrel	O2 plasma descum	600w 90°C 2min	surface activation
69	Verteq rinser/dryer	rinse dry		
70	Primeroven YES	HMDS prim	at room temperature	

71	KS spinner RC8	manual AZ9260 spin coat and soft bake	500rpm 10s CL + 1000rpm 60s CL, hotplate 90°C 15min	~12μm resist thickness
72	Stepper	expose RES	dose 800 focus -6 (mj/cm2, μm)	.
73	laktrack	develop	150mm_az4533_develop_thick	
73	Verteq rinser/dryer	rinse dry		
9-PDMS				
74	Barrel	O2 plasma descum	600w 25°C 5min	to remove HMDS primer
75	Verteq rinser/dryer	rinse dry		to from OH groups on the surface
76	SCS Labcoter	AP3000 vapor prime	Water based solution of the primer is preferred	to improve adhesion of PDMS to parylene
77	LFB PDMS Spincoating	spin coat PDMS	500rpm 20s CL + 3000rpm 60s CL, oven 90°C 30min	standard 10:1 base:curing agent mixture
78	CVC Connexion 800 / Veeco 2 Nexus	Sputter deposition	150nm Al, low power (120w), low temperature	Al as anti-stiction layer and hard etch mask for PDms dry etching
79	KS spinner RC8	manual HPR504 spin coat and soft bake	500rpm 10s CL + 4000rpm 40s CL, oven 90°C 30min	
80	MA-8 Karl Suss	expose Bond Pads	hard contact 10s	1000W high - pressure mercury arc lamp
81	PLSI developer	develop in PLSI + rins dry	2min	
82	PES heated etchant	wet etch Al	2min	
83	STS CPX clustertool	dry etch PDMS	ICP-PDMS01a, for 100min	PDMS etch stopping on Al
84	Verteq rinser/dryer	rinse dry		Rinse with water jet first to remove PDMS dry etch remnants.
10- Final steps to release the membrane				
85	STS CPX clustertool	deep etch silicon from the backside stoping on oxide + cleaning	PEG C01b 180min + PEG Tdesk clean 6min	deep etch silicon + oxygen plasma cleaning to remove deposited polymers to make the side walls hydrophilic for subsequent wet processing.
86	PES heated etchant	etch Al +rinse without water jet	2min	etch the anti-stiction Al

87		Hot air dry		
88	Suss Microtec Delta Altraspray	Spraycoat resist+oven cure 90°C 30min	Diluted az9260, 60 um	Mechanical support layer
89	BOE etchant	wet etch etch stop oxide and Ti UV block layer + rinse	20min	
90		Acetone strip spraycoated resist+rinse		
100		Hot air dry		
END				

Appendix 2- Membrane coating protocol

1. Clean the chips with 1% (w/v) tergazyme in water solution overnight, wash thoroughly with water and let them dry.
2. Expose the chips to oxygen plasma to activate the surface and sterilize.
3. Immediately after oxygen plasma, put 1% (v/v) solution of Silane primer (APTMS) in absolute ethanol (ethanol without any water) on the chips (~200 uL per chip), then add 5% (v/v) sterile water and wait for 10 minutes for the reaction to occur. (Note: the silane primer is sensitive to moisture, so take a sample form the stock bottle for your experiments, to prevent frequent exposure of stock bottle to room humidity.)
4. Aspirate the priming solution, wash with 70% ethanol + 3 times with sterile water, let the chips completely dry.
5. Add 66 ug/mL fibronectin in PBS solution to each chip (~ 10-15 uL per chip), and incubate for at least 1 hour. (Note: to prevent evaporation of the droplet put some water in the Petri dish containing each chip.)
6. Aspirate the fibronectin solution and carefully not to touch the membrane or the electrodes, add ~10 uL droplet of cell solution containing about 15-30k cells on each membrane under the stereo microscope.
7. Incubate for at least 1 hour, to let the cells attach to the membrane. (Note: to prevent evaporation of the droplet put some water in the Petri dish containing each chip.)
8. Add the rest of the medium gently not to sweep away the cells, and further incubate.

References

[1] "Drug Discovery and Development." Pharmaceutical Research and Manufacturers of America, Feb-2007.

[2] "Pharmaceutical Research and Manufacturers of America, 2013 Biopharmaceutical Research Industry Profile." Pharmaceutical Research and Manufacturers of America, Washington, DC: PhRMA, Jul-2013.

[3] A. M. Issa, K. A. Phillips, S. Van Bebber, H. G. Nidamarthy, K. E. Lasser, J. S. Haas, B. K. Alldredge, R. M. Wachter, and D. W. Bates, "Drug withdrawals in the United States: a systematic review of the evidence and analysis of trends," *Curr. Drug Saf.*, vol. 2, no. 3, pp. 177–185, 2007.

[4] K. Takahashi and S. Yamanaka, "Induction of Pluripotent Stem Cells from Mouse Embryonic and Adult Fibroblast Cultures by Defined Factors," *Cell*, vol. 126, no. 4, pp. 663–676, Aug. 2006.

[5] C. Y. Chan, P.-H. Huang, F. Guo, X. Ding, V. Kapur, J. D. Mai, P. K. Yuen, and T. J. Huang, "Accelerating drug discovery via organs-on-chips," *Lab. Chip*, vol. 13, no. 24, p. 4697, 2013.

[6] D. Huh, Y. Torisawa, G. A. Hamilton, H. J. Kim, and D. E. Ingber, "Microengineered physiological biomimicry: Organs-on-Chips," *Lab. Chip*, vol. 12, no. 12, p. 2156, 2012.

[7] A. D. van der Meer and A. van den Berg, "Organs-on-chips: breaking the in vitro impasse," *Integr. Biol.*, vol. 4, no. 5, p. 461, 2012.

[8] K. R. Chi, "Revolution dawning in cardiotoxicity testing," *Nat. Rev. Drug Discov.*, vol. 12, no. 8, pp. 565–567, 2013.

[9] A. Agarwal, J. A. Goss, A. Cho, M. L. McCain, and K. K. Parker, "Microfluidic heart on a chip for higher throughput pharmacological studies," *Lab. Chip*, vol. 13, no. 18, pp. 3599–3608, Aug. 2013.

[10] D. Huh, H. J. Kim, J. P. Fraser, D. E. Shea, M. Khan, A. Bahinski, G. A. Hamilton, and D. E. Ingber, "Microfabrication of human organs-on-chips," *Nat. Protoc.*, vol. 8, no. 11, pp. 2135–2157, Nov. 2013.

[11] P. Linder, J. Trzewik, M. Rüffer, G. M. Artmann, I. Digel, R. Kurz, A. Rothermel, A. Robitzki, and A. Temiz Artmann, "Contractile tension and beating rates of self-exciting monolayers and 3D-tissue constructs of neonatal rat cardiomyocytes," *Med. Biol. Eng. Comput.*, vol. 48, no. 1, pp. 59–65, Jan. 2010.

[12] R. Frotscher, J.-P. Koch, and M. Staat, "Computational investigation of drug action on human-induced stem cell-derived cardiomyocytes," *J. Biomech. Eng.*, Mar. 2015.

[13] R. Frotscher, M. Goßmann, H.-J. Raatschen, A. Temiz-Artmann, and M. Staat, "Simulation of Cardiac Cell-Seeded Membranes Using the Edge-

Based Smoothed FEM," in *Shell and Membrane Theories in Mechanics and Biology*, H. Altenbach and G. I. Mikhasev, Eds. Springer International Publishing, 2015, pp. 187–212.

[14] C. L. Lawrence, C. E. Pollard, T. G. Hammond, and J.-P. Valentin, "In vitro models of proarrhythmia," *Br. J. Pharmacol.*, vol. 154, no. 7, pp. 1516–1522, Aug. 2008.

[15] S. R. Braam, "Human embryonic stem cells : advancing biology and cardiogenesis towards functional applications l," Doctoral thesis, 2010.

[16] K. Finlayson, H. J. Witchel, J. McCulloch, and J. Sharkey, "Acquired QT interval prolongation and HERG: implications for drug discovery and development," *Eur. J. Pharmacol.*, vol. 500, no. 1–3, pp. 129–142, Oct. 2004.

[17] B. Fermini and A. A. Fossa, "The impact of drug-induced QT interval prolongation on drug discovery and development," *Nat. Rev. Drug Discov.*, vol. 2, no. 6, pp. 439–447, Jun. 2003.

[18] J. M. Nerbonne and R. S. Kass, "Molecular physiology of cardiac repolarization," *Physiol. Rev.*, vol. 85, no. 4, pp. 1205–1253, Oct. 2005.

[19] C. Denning and D. Anderson, "Cardiomyocytes from human embryonic stem cells as predictors of cardiotoxicity," *Drug Discov. Today Ther. Strateg.*, vol. 5, no. 4, pp. 223–232, Dec. 2008.

[20] L. Sintra Grilo, P.-A. Carrupt, and H. Abriel, "Stereoselective inhibition of the hERG1 potassium channel," *Pharmacol. Ion Channels Channelopathies*, vol. 1, p. 137, 2010.

[21] A. E. Enayetallah, D. Puppala, D. Ziemek, J. E. Fischer, S. Kantesaria, and M. T. Pletcher, "Assessing the translatability of In vivo cardiotoxicity mechanisms to In vitro models using causal reasoning," *BMC Pharmacol. Toxicol.*, vol. 14, no. 1, p. 46, 2013.

[22] O. Caspi, I. Itzhaki, I. Kehat, A. Gepstein, G. Arbel, I. Huber, J. Satin, and L. Gepstein, "In vitro electrophysiological drug testing using human embryonic stem cell derived cardiomyocytes," *Stem Cells Dev.*, vol. 18, no. 1, pp. 161–172, 2009.

[23] C. Py, M. Martina, G. A. Diaz-Quijada, C. C. Luk, D. Martinez, M. W. Denhoff, A. Charrier, T. Comas, R. Monette, A. Krantis, N. I. Syed, and G. A. R. Mealing, "From understanding cellular function to novel drug discovery: the role of planar patch-clamp array chip technology," *Pharmacol. Ion Channels Channelopathies*, vol. 2, p. 51, 2011.

[24] U. Egert and T. Meyer, "Heart on a Chip — Extracellular Multielectrode Recordings from Cardiac Myocytes in Vitro," in *Practical Methods in Cardiovascular Research*, P. D. S. Dhein, P. D. F. W. Mohr, and M. D. MD, Eds. Springer Berlin Heidelberg, 2005, pp. 432–453.

[25]   T. Meyer, K.-H. Boven, E. Günther, and M. Fejtl, "Micro-electrode arrays in cardiac safety pharmacology: a novel tool to study QT interval prolongation," *Drug Saf.*, vol. 27, no. 11, pp. 763–772, 2004.

[26]   M. Halbach, U. Egert, J. Hescheler, and K. Banach, "Estimation of action potential changes from field potential recordings in multicellular mouse cardiac myocyte cultures," *Cell. Physiol. Biochem. Int. J. Exp. Cell. Physiol. Biochem. Pharmacol.*, vol. 13, no. 5, pp. 271–284, 2003.

[27]   H. M. Himmel, A. Bussek, M. Hoffmann, R. Beckmann, H. Lohmann, M. Schmidt, and E. Wettwer, "Field and action potential recordings in heart slices: correlation with established in vitro and in vivo models," *Br. J. Pharmacol.*, vol. 166, no. 1, pp. 276–296, May 2012.

[28]   T. A. Quinn, P. Kohl, and U. Ravens, "Cardiac mechano-electric coupling research: fifty years of progress and scientific innovation," *Prog. Biophys. Mol. Biol.*, vol. 115, no. 2–3, pp. 71–75, Aug. 2014.

[29]   O. P. Hamill and B. Martinac, "Molecular basis of mechanotransduction in living cells," *Physiol. Rev.*, vol. 81, no. 2, pp. 685–740, Apr. 2001.

[30]   P. Kohl, C. Bollensdorff, and A. Garny, "Effects of mechanosensitive ion channels on ventricular electrophysiology: experimental and theoretical models," *Exp. Physiol.*, vol. 91, no. 2, pp. 307–321, Mar. 2006.

[31]   F. Ravelli, "Mechano-Electric Feedback and Atrial Arrhythmias," in *Mechanosensitivity in Cells and Tissues*, A. Kamkin and I. Kiseleva, Eds. Moscow: Academia, 2005.

[32]   M. B. Cannell, "Pulling on the Heart Strings A New Mechanism Within Starling's Law of the Heart?," *Circ. Res.*, vol. 104, no. 6, pp. 715–716, Mar. 2009.

[33]   B. D. Hoffman, C. Grashoff, and M. A. Schwartz, "Dynamic molecular processes mediate cellular mechanotransduction," *Nature*, vol. 475, no. 7356, pp. 316–323, Jul. 2011.

[34]   D. E. Ingber, "Cellular mechanotransduction: putting all the pieces together again," *FASEB J. Off. Publ. Fed. Am. Soc. Exp. Biol.*, vol. 20, no. 7, pp. 811–827, May 2006.

[35]   C. G. Galbraith and M. P. Sheetz, "Forces on adhesive contacts affect cell function," *Curr. Opin. Cell Biol.*, vol. 10, no. 5, pp. 566–571, Oct. 1998.

[36]   P. A. Gottlieb and F. Sachs, "Cell biology: The sensation of stretch," *Nature*, vol. 483, no. 7388, pp. 163–164, Mar. 2012.

[37]   B. L. Prosser and C. W. Ward, "Mechano-Chemo Transduction Tunes the Heartstrings," *Sci. Signal.*, vol. 7, no. 317, pp. pe7–pe7, Mar. 2014.

[38]   N. Wang, J. P. Butler, and D. E. Ingber, "Mechanotransduction across the cell surface and through the cytoskeleton," *Science*, vol. 260, no. 5111, pp. 1124–1127, May 1993.

[39]   J. Iqbal and M. Zaidi, "Molecular regulation of mechanotransduction," *Biochem. Biophys. Res. Commun.*, vol. 328, no. 3, pp. 751–755, Mar. 2005.

[40]   S. A. Thompson, C. R. Copeland, D. H. Reich, and L. Tung, "Mechanical Coupling Between Myofibroblasts and Cardiomyocytes Slows Electric Conduction in Fibrotic Cell Monolayers," *Circulation*, vol. 123, no. 19, pp. 2083–2093, May 2011.

[41]   A. Salameh and S. Dhein, "Effects of mechanical forces and stretch on intercellular gap junction coupling," *Biochim. Biophys. Acta BBA - Biomembr.*, vol. 1828, no. 1, pp. 147–156, Jan. 2013.

[42]   A. Kamkin, I. Kiseleva, and G. Isenberg, "Stretch-activated currents in ventricular myocytes: amplitude and arrhythmogenic effects increase with hypertrophy," *Cardiovasc. Res.*, vol. 48, no. 3, pp. 409–420, 2000.

[43]   A. Kamkin, I. Kiseleva, K.-D. Wagner, and H. Scholz, "Mechano-Electric Feedback in the Heart: Evidence from Intracellular Microelectrode Recordings on Multicellular Preparations and Single Cells from Healthy and Diseased Tissue," in *Mechanosensitivity in Cells and Tissues*, A. Kamkin and I. Kiseleva, Eds. Moscow: Academia, 2005.

[44]   K. A. Addae-Mensah and J. P. Wikswo, "Measurement techniques for cellular biomechanics in vitro," *Exp. Biol. Med. Maywood NJ*, vol. 233, no. 7, pp. 792–809, Jul. 2008.

[45]   M. Brandenburger, J. Wenzel, R. Bogdan, D. Richardt, F. Nguemo, M. Reppel, J. Hescheler, H. Terlau, and A. Dendorfer, "Organotypic slice culture from human adult ventricular myocardium," *Cardiovasc. Res.*, vol. 93, no. 1, pp. 50–59, Jan. 2012.

[46]   F. J. Chorro, I. Trapero, L. Such-Miquel, F. Pelechano, L. Mainar, J. Canoves, A. Tormos, A. Alberola, L. Hove-Madsen, J. Cinca, and L. Such, "Pharmacological modifications of the stretch-induced effects on ventricular fibrillation in perfused rabbit hearts," *AJP Heart Circ. Physiol.*, vol. 297, no. 5, pp. H1860–H1869, Nov. 2009.

[47]   S. S. Nunes, J. W. Miklas, J. Liu, R. Aschar-Sobbi, Y. Xiao, B. Zhang, J. Jiang, S. Masse, M. Gagliardi, A. Hsieh, N. Thavandiran, M. A. Laflamme, K. Nanthakumar, G. Gross, P. H. Backx, G. Keller, and M. Radisic, "Biowire: a new platform for maturation of human pluripotent stem cell derived cardiomyocytes," *Nat. Methods*, vol. 10, no. 8, pp. 781–787, Aug. 2013.

[48]   N. L. Tulloch, V. Muskheli, M. V. Razumova, F. S. Korte, M. Regnier, K. D. Hauch, L. Pabon, H. Reinecke, and C. E. Murry, "Growth of engineered human myocardium with mechanical loading and vascular coculture," *Circ. Res.*, vol. 109, no. 1, pp. 47–59, Jun. 2011.

[49]   D. Dado, M. Sagi, S. Levenberg, and A. Zemel, "Mechanical control of stem cell differentiation," *Regen. Med.*, vol. 7, no. 1, pp. 101–116, Jan. 2012.

[50]   M. Flaibani, L. Boldrin, E. Cimetta, M. Piccoli, P. D. Coppi, and N. Elvassore, "Muscle differentiation and myotubes alignment is influenced by

micropatterned surfaces and exogenous electrical stimulation," *Tissue Eng. Part A*, vol. 15, no. 9, pp. 2447–2457, 2009.

[51] W. L. Murphy, T. C. McDevitt, and A. J. Engler, "Materials as stem cell regulators," *Nat. Mater.*, vol. 13, no. 6, pp. 547–557, Jun. 2014.

[52] D. A. Pijnappels, M. J. Schalij, A. A. Ramkisoensing, J. van Tuyn, A. A. F. de Vries, A. van der Laarse, D. L. Ypey, and D. E. Atsma, "Forced alignment of mesenchymal stem cells undergoing cardiomyogenic differentiation affects functional integration with cardiomyocyte cultures," *Circ. Res.*, vol. 103, no. 2, pp. 167–176, Jul. 2008.

[53] B.-Y. Yu, P.-H. Chou, Y.-M. Sun, Y.-T. Lee, and T.-H. Young, "Topological micropatterned membranes and its effect on the morphology and growth of human mesenchymal stem cells (hMSCs)," *J. Membr. Sci.*, vol. 273, no. 1–2, pp. 31–37, Mar. 2006.

[54] A. Grosberg, P. W. Alford, M. L. McCain, and K. K. Parker, "Ensembles of engineered cardiac tissues for physiological and pharmacological study: heart on a chip," *Lab. Chip*, vol. 11, no. 24, pp. 4165–4173, Dec. 2011.

[55] D. G. Simpson, M. Majeski, T. K. Borg, and L. Terracio, "Regulation of cardiac myocyte protein turnover and myofibrillar structure in vitro by specific directions of stretch," *Circ. Res.*, vol. 85, no. 10, pp. e59–69, Nov. 1999.

[56] J. H.-C. Wang, G. Yang, Z. Li, and W. Shen, "Fibroblast responses to cyclic mechanical stretching depend on cell orientation to the stretching direction," *J. Biomech.*, vol. 37, no. 4, pp. 573–576, Apr. 2004.

[57] S. M. Gopalan, C. Flaim, S. N. Bhatia, M. Hoshijima, R. Knoell, K. R. Chien, J. H. Omens, and A. D. McCulloch, "Anisotropic stretch-induced hypertrophy in neonatal ventricular myocytes micropatterned on deformable elastomers," *Biotechnol. Bioeng.*, vol. 81, no. 5, pp. 578–587, Mar. 2003.

[58] D.-H. Kim, R. Ghaffari, N. Lu, and J. A. Rogers, "Flexible and Stretchable Electronics for Biointegrated Devices," *Annu. Rev. Biomed. Eng.*, vol. 14, no. 1, pp. 113–128, Aug. 2012.

[59] J.-H. Ahn and J. H. Je, "Stretchable electronics: materials, architectures and integrations," *J. Phys. Appl. Phys.*, vol. 45, no. 10, p. 103001, Mar. 2012.

[60] P. Wei, R. Taylor, Z. Ding, C. Chung, O. J. Abilez, G. Higgs, B. L. Pruitt, and B. Ziaie, "Stretchable microelectrode array using room-temperature liquid alloy interconnects," *J. Micromechanics Microengineering*, vol. 21, no. 5, p. 054015, May 2011.

[61] S. Rosset, M. Niklaus, P. Dubois, and H. R. Shea, "Metal ion implantation for the fabrication of stretchable electrodes on elastomers," *Adv. Funct. Mater.*, vol. 19, no. 3, pp. 470–478, 2009.

[62] M. K. Shin, J. Oh, M. Lima, M. E. Kozlov, S. J. Kim, and R. H. Baughman, "Elastomeric Conductive Composites Based on Carbon Nanotube Forests," *Adv. Mater.*, vol. 22, no. 24, pp. 2663–2667, Jun. 2010.

[63]   K.-Y. Chun, Y. Oh, J. Rho, J.-H. Ahn, Y.-J. Kim, H. R. Choi, and S. Baik, "Highly conductive, printable and stretchable composite films of carbon nanotubes and silver," *Nat. Nanotechnol.*, vol. 5, no. 12, pp. 853–857, Dec. 2010.

[64]   T. Adrega and S. P. Lacour, "Stretchable gold conductors embedded in PDMS and patterned by photolithography: fabrication and electromechanical characterization," *J. Micromechanics Microengineering*, vol. 20, no. 5, p. 055025, May 2010.

[65]   D.-H. Kim, J. Song, W. M. Choi, H.-S. Kim, R.-H. Kim, Z. Liu, Y. Y. Huang, K.-C. Hwang, Y. Zhang, and J. A. Rogers, "Materials and noncoplanar mesh designs for integrated circuits with linear elastic responses to extreme mechanical deformations," *Proc. Natl. Acad. Sci.*, vol. 105, no. 48, pp. 18675–18680, Dec. 2008.

[66]   D.-H. Kim, N. Lu, R. Ghaffari, Y.-S. Kim, S. P. Lee, L. Xu, J. Wu, R.-H. Kim, J. Song, Z. Liu, J. Viventi, B. de Graff, B. Elolampi, M. Mansour, M. J. Slepian, S. Hwang, J. D. Moss, S.-M. Won, Y. Huang, B. Litt, and J. A. Rogers, "Materials for multifunctional balloon catheters with capabilities in cardiac electrophysiological mapping and ablation therapy," *Nat. Mater.*, vol. 10, no. 4, pp. 316–323, Apr. 2011.

[67]   D.-H. Kim, N. Lu, Y. Huang, and J. A. Rogers, "Materials for stretchable electronics in bioinspired and biointegrated devices," *MRS Bull.*, vol. 37, no. 03, pp. 226–235, Mar. 2012.

[68]   R. Verplancke, F. Bossuyt, D. Cuypers, and J. Vanfleteren, "Thin-film stretchable electronics technology based on meandering interconnections: fabrication and mechanical performance," *J. Micromechanics Microengineering*, vol. 22, no. 1, p. 015002, Jan. 2012.

[69]   C. Frantz, K. M. Stewart, and V. M. Weaver, "The extracellular matrix at a glance," *J. Cell Sci.*, vol. 123, no. Pt 24, pp. 4195–4200, Dec. 2010.

[70]   H. Baharvand, M. Azarnia, K. Parivar, and S. K. Ashtiani, "The effect of extracellular matrix on embryonic stem cell-derived cardiomyocytes," *J. Mol. Cell. Cardiol.*, vol. 38, no. 3, pp. 495–503, Mar. 2005.

[71]   T. A. Desai, "Micro- and nanoscale structures for tissue engineering constructs," *Med. Eng. Phys.*, vol. 22, no. 9, pp. 595–606, Nov. 2000.

[72]   M. Théry, "Micropatterning as a tool to decipher cell morphogenesis and functions," *J. Cell Sci.*, vol. 123, no. Pt 24, pp. 4201–4213, Dec. 2010.

[73]   G. M. Whitesides, E. Ostuni, S. Takayama, X. Jiang, and D. E. Ingber, "Soft lithography in biology and biochemistry," *Annu. Rev. Biomed. Eng.*, vol. 3, pp. 335–373, 2001.

[74]   R. S. Kane, S. Takayama, E. Ostuni, D. E. Ingber, and G. M. Whitesides, "Patterning proteins and cells using soft lithography," *Biomaterials*, vol. 20, no. 23–24, pp. 2363–2376, Dec. 1999.

[75]   F. Grinnell and M. K. Feld, "Fibronectin adsorption on hydrophilic and hydrophobic surfaces detected by antibody binding and analyzed during cell adhesion in serum-containing medium.," *J. Biol. Chem.*, vol. 257, no. 9, pp. 4888–4893, 1982.

[76]   G. K. Toworfe, R. J. Composto, C. S. Adams, I. M. Shapiro, and P. Ducheyne, "Fibronectin adsorption on surface-activated poly(dimethylsiloxane) and its effect on cellular function," *J. Biomed. Mater. Res. A*, vol. 71, no. 3, pp. 449–461, Dec. 2004.

[77]   A. W. Feinberg, A. Feigel, S. S. Shevkoplyas, S. Sheehy, G. M. Whitesides, and K. K. Parker, "Muscular Thin Films for Building Actuators and Powering Devices," *Science*, vol. 317, no. 5843, pp. 1366–1370, Sep. 2007.

[78]   T. Dvir, B. P. Timko, D. S. Kohane, and R. Langer, "Nanotechnological strategies for engineering complex tissues," *Nat. Nanotechnol.*, vol. 6, no. 1, pp. 13–22, Jan. 2011.

[79]   T. Shimizu, M. Yamato, A. Kikuchi, and T. Okano, "Cell sheet engineering for myocardial tissue reconstruction," *Biomaterials*, vol. 24, no. 13, pp. 2309–2316, Jun. 2003.

[80]   J. Deutsch, D. Motlagh, B. Russell, and T. A. Desai, "Fabrication of microtextured membranes for cardiac myocyte attachment and orientation," *J. Biomed. Mater. Res.*, vol. 53, no. 3, pp. 267–275, 2000.

[81]   J. H. C. Wang, G. Yang, and Z. Li, "Controlling cell responses to cyclic mechanical stretching," *Ann. Biomed. Eng.*, vol. 33, no. 3, pp. 337–342, Mar. 2005.

[82]   S. F. Cogan, "Neural Stimulation and Recording Electrodes," *Annu. Rev. Biomed. Eng.*, vol. 10, no. 1, pp. 275–309, Aug. 2008.

[83]   G. Dieter, *Mechanical Metallurgy*, 3 edition. New York: McGraw-Hill Science/Engineering/Math, 1986.

[84]   J. Shigley, C. Mischke, and T. Brown, *Standard Handbook of Machine Design*, 3 edition. New York: McGraw-Hill Professional, 2004.

[85]   J. K. N. R. G. Budynas, *Shigley's Mechanical Engineering Design*. McGraw-Hill, 2008.

[86]   C. Y. Shih, T. A. Harder, and Y.-C. Tai, "Yield strength of thin-film parylene-C," *Microsyst. Technol.*, vol. 10, no. 5, pp. 407–411, 2004.

[87]   W. K. Schomburg, *Introduction to Microsystem Design*, vol. 1. Berlin, Heidelberg: Springer Berlin Heidelberg, 2011.

[88]   J. Neggers, J. Hoefnagels, F. Hild, S. Roux, and M. Geers, "Full-Field Bulge Testing Using Global Digital Image Correlation," in *MEMS and Nanotechnology, Volume 4*, T. Proulx, Ed. Springer New York, 2011, pp. 99–103.

[89]   A. Szekeres and P. Danesh, "Mechanical stress in structures formed by thermal oxidation of amorphous and crystalline silicon," *Semicond. Sci. Technol.*, vol. 11, no. 8, p. 1225, Aug. 1996.

[90]   E. Iwase, P.-C. Hui, D. Woolf, A. W. Rodriguez, S. G. Johnson, F. Capasso, and M. Lončar, "Control of buckling in large micromembranes using engineered support structures," *J. Micromechanics Microengineering*, vol. 22, no. 6, p. 065028, Jun. 2012.

[91]   "Application note: Dry Etching with Photoresist Masks." MicroChemicals GmbH, 2013.

[92]   H. Mei, R. Huang, J. Y. Chung, C. M. Stafford, and H.-H. Yu, "Buckling modes of elastic thin films on elastic substrates," *Appl. Phys. Lett.*, vol. 90, no. 15, p. 151902, 2007.

[93]   N. Bowden, S. Brittain, A. G. Evans, J. W. Hutchinson, and G. M. Whitesides, "Spontaneous formation of ordered structures in thin films of metals supported on an elastomeric polymer," *Nature*, vol. 393, no. 6681, pp. 146–149, May 1998.

[94]   W. T. S. Huck, N. Bowden, P. Onck, T. Pardoen, J. W. Hutchinson, and G. M. Whitesides, "Ordering of Spontaneously Formed Buckles on Planar Surfaces," *Langmuir*, vol. 16, no. 7, pp. 3497–3501, Apr. 2000.

[95]   E. Sultan and A. Boudaoud, "The Buckling of a Swollen Thin Gel Layer Bound to a Compliant Substrate," *J. Appl. Mech.*, vol. 75, no. 5, p. 051002, 2008.

[96]   H. Vandeparre, S. Gabriele, F. Brau, C. Gay, K. K. Parker, and P. Damman, "Hierarchical wrinkling patterns," *Soft Matter*, vol. 6, no. 22, p. 5751, 2010.

[97]   B. Balakrisnan, S. Patil, and E. Smela, "Patterning PDMS using a combination of wet and dry etching," *J. Micromechanics Microengineering*, vol. 19, no. 4, p. 047002, Apr. 2009.

[98]   W. Chen, R. H. W. Lam, and J. Fu, "Photolithographic surface micromachining of polydimethylsiloxane (PDMS)," *Lab. Chip*, vol. 12, no. 2, p. 391, 2012.

[99]   I. R. Minev and S. P. Lacour, "Impedance spectroscopy on stretchable microelectrode arrays," *Appl. Phys. Lett.*, vol. 97, no. 4, p. 043707, 2010.

[100]   K. B. Oldham, J. C. Myland, A. M. Bond, and Wiley InterScience (Online service), *Electrochemical science and technology fundamentals and applications*. Chichester, West Sussex, U.K.; Hoboken: John Wiley & Sons, 2011.

[101]   H. Wang and L. Pilon, "Accurate Simulations of Electric Double Layer Capacitance of Ultramicroelectrodes," *J. Phys. Chem. C*, vol. 115, no. 33, pp. 16711–16719, Aug. 2011.

[102]   N. Gavish and K. Promislow, "Dependence of the dielectric constant of electrolyte solutions on ionic concentration," *ArXiv Prepr. ArXiv12085169*, 2012.

[103]   E. Barsoukov and J. R. Macdonald, *Impedance Spectroscopy: Theory, Experiment, and Applications*, 2 edition. Hoboken, N.J: Wiley-Interscience, 2005.

[104] S. K. Pakazad, A. Savov, A. van de Stolpe, and R. Dekker, "A novel stretchable micro-electrode array (SMEA) design for directional stretching of cells," *J. Micromechanics Microengineering*, vol. 24, no. 3, p. 034003, Mar. 2014.

[105] J. Tao, N. W. Cheung, and C. Hu, "Electromigration characteristics of TiN barrier layer material," *IEEE Electron Device Lett.*, vol. 16, no. 6, pp. 230–232, Jun. 1995.

[106] D. A. Borkholder, *Cell Based Biosensors Using Microelectrodes*. Stanford University, 1998.

[107] Q. Liu, *Cell-Based Biosensors: Principles and Applications*. Artech House, 2014.

[108] J. Wang, C. Wu, N. Hu, J. Zhou, L. Du, and P. Wang, "Microfabricated Electrochemical Cell-Based Biosensors for Analysis of Living Cells In Vitro," *Biosensors*, vol. 2, no. 2, pp. 127–170, Apr. 2012.

[109] G. Altankov and T. Groth, "Reorganization of substratum-bound fibronectin on hydrophilic and hydrophobic materials is related to biocompatibility," *J. Mater. Sci. Mater. Med.*, vol. 5, no. 9–10, pp. 732–737, Sep. 1994.

[110] L. M. Pakstis, J. P. Dunkers, A. Zheng, T. V. Vorburger, T. P. Quinn, and M. T. Cicerone, "Evaluation of polydimethylsiloxane modification methods for cell response," *J. Biomed. Mater. Res. A*, vol. 9999A, p. NA–NA, 2009.

[111] S. S. Lateef, S. Boateng, T. J. Hartman, C. A. Crot, B. Russell, and L. Hanley, "GRGDSP peptide-bound silicone membranes withstand mechanical flexing in vitro and display enhanced fibroblast adhesion," *Biomaterials*, vol. 23, no. 15, pp. 3159–3168, Aug. 2002.

[112] N. Sasaki, T. Mitsuiye, and A. Noma, "Effects of mechanical stretch on membrane currents of single ventricular myocytes of guinea-pig heart," *Jpn. J. Physiol.*, vol. 42, no. 6, pp. 957–970, 1992.

[113] G. Iribe, C. W. Ward, P. Camelliti, C. Bollensdorff, F. Mason, R. A. B. Burton, A. Garny, M. K. Morphew, A. Hoenger, W. J. Lederer, and P. Kohl, "Axial stretch of rat single ventricular cardiomyocytes causes an acute and transient increase in Ca2+ spark rate," *Circ. Res.*, vol. 104, no. 6, pp. 787–795, Mar. 2009.

[114] T. Matsuda, K. Takahashi, T. Nariai, T. Ito, T. Takatani, Y. Fujio, and J. Azuma, "N-cadherin-mediated cell adhesion determines the plasticity for cell alignment in response to mechanical stretch in cultured cardiomyocytes," *Biochem. Biophys. Res. Commun.*, vol. 326, no. 1, pp. 228–232, Jan. 2005.

[115] K. Kada, K. Yasui, K. Naruse, K. Kamiya, I. Kodama, and J. Toyama, "Orientation change of cardiocytes induced by cyclic stretch stimulation: time dependency and involvement of protein kinases," *J. Mol. Cell. Cardiol.*, vol. 31, no. 1, pp. 247–259, Jan. 1999.

[116] J. L. Samuel and H. H. Vandenburgh, "Mechanically induced orientation of adult rat cardiac myocytes in vitro," *Vitro Cell. Dev. Biol. J. Tissue Cult. Assoc.*, vol. 26, no. 9, pp. 905–914, Sep. 1990.

Summary

A potential serious side effect of drugs is cardiotoxicity which can result in lethal heart arrhythmias. Cardiotoxicity has been the leading cause of drug withdrawals from the market in the past decades, and has been responsible for costly failures in late stage clinical trials. This highlights the unmet need in the pharmaceutical industry for more accurate and predicative cardiotoxicity screening assays. An important indication for drug-induced proarrhythmic cardiotoxicity is the prolongation of the action potential duration of the cardiomyocytes. The prolongation of the action potential duration can be detected in vitro through field potential measurements from cardiomyocytes cultured on Micro-Electrode Arrays (MEAs) when they are subjected to drug compounds.

MEAs are normally fabricated on rigid substrates which precludes mechanical stretching and contraction of the cultured cardiomyocytes as it happens in vivo during diastole and systole of the heart. It has been demonstrated in the literature that cardiomyocytes can sense mechanical stretching and adapt their electrical and mechanical responses to it, through mechano-electric coupling phenomena, causing alterations of the action potential shape, duration, and rhythm. Including physiologically relevant mechanical loading of cardiomyocytes in the in vitro model, can lead to potentially more predictive screening results.

In this thesis the design, fabrication and characterization of a novel platform for in vitro electrophysiological measurements is presented which allows for in situ mechanical loading of cardiomyocytes. The platform is based on pneumatically actuated Stretchable Micro-Electrode Array (SMEA) chips which are fabricated using state of the art silicon micro-fabrication technology. The main technological challenges addressed in this thesis were the mechanical design of the electrical interconnects for the stretchable devices, and the development of a manufacturable micro-fabrication technology to enable high volume production of the SMEA chips. The electrochemical and electromechanical characterization of the chips is presented, together with proof of concept field potential measurements from human stem cell derived cardiomyocytes under cyclic mechanical loading.

Samenvatting

Cardiotoxiteit is een ernstige bijwerking van medicijnen die dodelijke hartritme-stoornissen tot gevolg kan hebben. Het is een van de belangrijkste redenen waarom medicijnen tijdens klinische testen worden afgekeurd, of zelfs uit de markt moeten worden genomen. De farmaceutische industrie heeft dus een dringende behoefte aan goede en voorspellende tests waarmee cardiotoxiteit in een vroeg stadium kan worden vastgesteld. Een belangrijke indicatie voor medicijn-geïnduceerde cardiotoxiteit is een verlenging van de actiepotentiaal van hartspiercellen. Een verlenging van die actiepotentiaal kan in vitro worden vastgesteld, door middel van veldpotentiaal-metingen aan hartspiercellen. Deze zijn aangebracht op een multi-electrode array (MEA), waarop ze worden blootgesteld aan het te testen medicijn.

MEA's worden standaard gemaakt op rigide substraten,waardoor de hartspiercellen niet kunnen rekken en samentrekken zoals dat in een normaal hart gebeurt. In de literatuur is echter aangetoond dat hartspiercellen, door mechanisch-electrische koppelingen, mechanische rek kunnen detecteren en er hun gedrag met betrekking tot actiepotentiaal niveau, tijdsduur en frequentie op aanpassen. Het integreren van mechanische stress in een MEA, zal daardoor een cardiotoxiteits-test met een betere voorspellende waarde opleveren.

In dit proefschrift wordt het ontwerp, de fabricage en de karakterisatie van een nieuw platform voor in vitro electrophysiology- metingen gepresenteerd, waarin de hartspiercellen in-situ aan mechansche stress kunnen worden onderworpen. Het platform is gebaseerd op een pneumatisch geactueerde MEA, die wordt gefabriceerd met behulp van moderne micro-fabricage technologie. De belangrijkste uitdagingen hierbij waren de fabricage van rekbare electrische verbindingen voor de electrodes en het komen tot een maakbare technologie, geschikt voor massafabricage. De electrochemische en electromechanische eigenschappen van de ontwikkelde MEA worden besproken. "Proof-of-concept" veldpotentiaal- metingen aan hartspiercellen onder rek worden getoond.

List of Publications

1. S. K. Pakazad, A. Savov, A. van de Stolpe, and R. Dekker, "A novel stretchable micro-electrode array (SMEA) design for directional stretching of cells," *J. Micromechanics Microengineering*, vol. 24, no. 3, p. 034003, Mar. 2014.
2. S. K. Pakazad, A. Savov, S. R. Braam, and R. Dekker, "A Platform for Manufacturable Stretchable Micro-electrode Arrays," *Procedia Eng.*, vol. 47, pp. 817–820, 2012.
3. S. Khoshfetrat Pakazad, A. M. Savov, A. van de Stolpe, S. Braam, B. van Meer, and R. Dekker, "A stretchable Micro-Electrode Array for in vitro electrophysiology," in *2011 IEEE 24th International Conference on Micro Electro Mechanical Systems (MEMS)*, 2011, pp. 829–832.
4. S. K. Pakazad, A. Savov, A. van de Stolpe, and R. Dekker , "A Novel SMEA Design For Directional Stretching Of Cells", *in Proceedings of 2013 International Conference on Microtechnologies in Medicine and Biology*, Marina del Rey, California, USA, April 10 - 12, 2013, pp. 6-7.
5. S. K. Pakazad, A. Savov, and R. Dekker, "A Manufacturable Platform For In Vitro Electrophysiological Studies Under Mechanical Stimulation", *in Proceedings of 17th International Conference on Miniaturized Systems for Chemistry and Life Sciences*, 27-31 October 2013, Freiburg, Germany, pp. 1412-1414.
6. A. Savov, S. K. Pakazad, S. Joshi, V. Henneken, and R. Dekker, "A post processing approach for manufacturing high-density stretchable sensor arrays," in *2014 IEEE SENSORS*, 2014, pp. 1703–1705.
7. R. Dekker, S. Braam, V. Henneken, A. van der Horst, S. K. Pakazad, M. Louwerse, B. van Meer, B. Mimoun, A. Savov, and A. van de Stolpe, "Living Chips and Chips for the living," in *2012 IEEE Bipolar/BiCMOS Circuits and Technology Meeting (BCTM)*, 2012, pp. 1–9.

Poster presentations:

1. S. K. Pakazad, A. Savov, A. van de Stolpe , S. R. Braam, and R. Dekker, "A Stretchable Micro-Electrode Array for in vitro Electrophysiology", Lorentz Organs on Chips: Human Disease Models Workshop, 24-28 Sep, 2012, Leiden, The Netherlands.

2. S. K. Pakazad, A. Savov, A. van de Stolpe, and R. Dekker, "Stretchable Micro-Electrode Array", 3rd Flexible & Stretchable Electronics Workshop, November 15 – 17, 2011, Berlin, Germany.
3. S. K. Pakazad, A. van de Stolpe, and R. Dekker , "A platform for cardiotoxicity screening based on manufacturable Stretchable Micro-Electrodes Arrays (SMEAs)", The Safety Pharmacology Society 13th Annual Meeting, September 16-19, 2013, Rotterdam, The Netherlands.
4. S. K. Pakazad, A. Savov, A. van de Stolpe, and R. Dekker, "A platform based on Stretchable Micro-Electrode Arrays for more predictive cardiotoxicity screening", NanoCity 2014, 27-28 October, 2014, Utrecht, The Netherlands.

Patents:

1. R. Dekker, A. Van De Stolpe, B. jan Van Meer, S. Khoshfetrat Pakazad, and A. Savov, "Cardiomyocyte Containing Device, Manufacturing Method and Measuring Method," WO/2012/017343, 10-Feb-2012.
2. R. Dekker, V. Henneken, S. Khoshfetrat Pakazad, "A method for fabricating a Stretchable CMUT Array", Philips Intellectual Property & Standards ID, 2012ID00959.

Acknowledgments

This research could not have been successfully accomplished without the help, advice, encouragement and support from many people. Here, I would like to express my gratitude to them. Firstly, I would like to thank my supervisor Ronald Dekker for providing the opportunity and the means to carry out this research. His vision and experience at the intersection between academy and industry were key to the success of this project. I have learned a lot from him at both scientific and personal levels.

During the time carrying out this research I was hosted by the micro systems and devices department of Philips Research in Eindhoven. I would like to greatly thank Derk Reefman and Hans Huiberts the former and current heads of the department for kindly hosting me. In Philips Research Eindhoven I have had the privilege of receiving help and advice from many great scientists. I would like to specially thank Eugene Timmering, without his help and advice on many microfabrication challenges that I faced, it was impossible to successfully fabricate my devices. I would like to thank Alwin Verschueren, for giving me advice and allowing me to work in his lab for electrochemical characterization of the chips. I greatly thank Vincent Henneken for his advice, encouragement and many valuable discussions we had, and enabling the clean room work under his project, and for being a patient mediator in many cases. The successful clean room microfabrication results presented in this thesis were impossible without the help, advice and experience of the many great colleagues in the Philips Innovation and Services (PInS) clean room. Also, for the design and development of the electro-pneumatic platform I received a lot of help and support from the colleagues in the mechanical, pneumatic and electrical workshops of PInS. I would like to acknowledge their skills, expertise and friendly way of working and thank them all.

Coming from an engineering background, I had little understanding of working with living cells. I am extremely thankful to Anja van de Stolpe for encouraging me and giving me the opportunity to learn more about cells and biosafety and providing the means and supervision to do experiments in Philips Life Science Facilities. I would like to thank Christa Dam de Veen, for teaching me the ways of working with cells for the first time and helping me with my experiments. For cellular experiments we were also collaborating with LUMC. I would like to

express my gratitude and appreciation to Christine Mummery and Robert Passier for enabling this collaboration. Also, I would like to thank Leon Tertoolen for sharing his expertise in electrophysiology to enable the measurements, and Marcelo C. Ribeiro for dedicating time to perform the initial culturing experiments. I would like to specially thank Stefan Braam for his indispensable collaboration and hosting me in Pluriomics culture facilities for proof of concept stem cell derived cardiomyocyte culturing and helping me with the very first successful field potential measurements on my devices. I would also like to thank Karin Langenberg for her great help with culturing and maintaining the cells.

I would like to thank Lina Sarro the head of ECTM department for her support, and encouragement during my Ph.D. period and for being an inspiring mentor to every student in our department including me. I would like also to thank the secretary of our department Marian Roozenburg, she has always kindly helped me with my many requests.

During my time in the student office and then the Ph.D. office in Philips Research Eindhoven and through the PPC and PIC events, I had the pleasure to meet many great students with many of whom I am still in contact and we became friends and have a lot of unforgettable memories together. Specially, I would like to thank Angel Savov for his friendship and numerous scientific and personal discussions we had. I learned a lot about microfabrication and clean room work from him, and the initial work we did together formed the basis of this thesis work. Also, I would like to thank him and Shivani Joshi for kindly accepting to be my paranymphs for my Ph.D. defense. I would also like to thank Ronald Stoute for kindly making the fantastic illustrations of the mechanical design of the electro-pneumatic adaptor which I presented in chapter one.

The last but not the least I would like to thank my family and friends for their indispensable emotional support, love and kindness. Specially, my girlfriend Sepide for being the closest to me in all the hard times during preparation of this thesis; her presence, brilliance and positive energy always have lifted me up.

To all of you who were with me through the ups and downs of this journey, and contributed to its success…thank you.

Saeed
May 2015, Eindhoven

About The Author

Saeed Khoshfetrat Pakazad was born in Tehran, Iran, in 1980. He received his B.Sc. degree in Electronics Engineering from K.N.Toosi University of Technology, Tehran, Iran, in 2003. He holds two M.Sc. degrees. The first one in Electrical Engineering from Tehran Polytechnic University in 2006, and the second M.Sc. degree with distinction in Biomedical Engineering from Delft University of Technology, the Netherlands, in 2010. He carried out his master thesis research in Philips Research Eindhoven, on the topic of design and micro-fabrication of stretchable devices. His M.Sc. degree research resulted in a European and US patent for Philips. He started his Ph.D. in September 2010 with Delft University of Technology in the laboratory of Electronic Components, Technology and Materials (ECTM) in the Department of Microelectronics on the topic of developing a miniaturized heart-on-a-chip platform for pharmaceutical drug screening applications. The research was carried out in collaboration with Philips Research Eindhoven and Leiden University Medical Center (LUMC), and was partially funded by the NanoNextNL consortium under program 06C Nano-bio interfaces & devices. The research was highlighted in the Delta magazine of TU Delft in the article "Kloppende hartcellen op een chip" published on April 13th, 2015. One of his papers, "A novel stretchable micro-electrode array (SMEA) design for directional stretching of cells" was selected to form part of the feature collection MEMS and Microengineering for Life Science Applications in the Journal of Micromechanics and Microengineering. He was invited to present his research results in the Safety Pharmacology Society (SPS) 13th annual meeting, in Rotterdam, in September 2013. Based on the successful results, the project he was working on was granted a full valorization fund from NanoNextNL consortium in April 2015.

Having a multidisciplinary engineering background, his main research interests are addressing life science applications with the help of microfabrication technologies through understanding the physics governing the mechanical and electrochemical interactions of cells and their in vitro environments at micro-scale.